



Vol (1), No(2) September 2017

LIBYAN JOURNAL FOR ENGINEERING RESEARCH

*A Refereed Scientific Journal Issued Semi-annually by Faculty of Engineering -
Benghazi University*

ISSN 2522-6967

General Director

Dr. Tawfiq Hussein Elmenfy

Editor-in-Chief

Dr. Amer A. M. Boushaala

Editor-in-director

Dr. Salah A. Masheiti

Editorial Committee

Dr. Abdelhamid Houssein Alhassi

Mr. Nassr A. AlFadil

Mr. Elsanousi Ahmed Gaderbough

Mr. Isam Abdelkarim Belkasem

Mr. Hamzah A. I. Mohamed

Mr. Mohamed Milad Hawiwo

Technical Advisor

Dr. Hussam El-Din F. El-Sheikh

Technical Support

Mr. Salah Abdullah Algallai

All copyrights reserved to Libyan Journal for Engineering Research. No part of this publication may be reproduced, stored in a retrieval form, or transmitted in any other form without prior permission of the copyright owner.

All correspondences should be addressed to:

Editor in Chief of Libyan Journal for Engineering Research.

Faculty of Engineering, Benghazi University, Libya.

Email: LyJER@uob.edu.ly

ULR: www.lyjer.uob.edu.ly

*Faculty of Engineering, Benghazi University, Benghazi – Libya
www.lyjer.uob.edu.ly*

Aims of the Journal

This journal aims to provide a reliable source of information on current research and development in the fields of basic and applied sciences, on the national and international levels, as well as exchange of ideas and information for experts in these fields. Moreover, it will provide an opportunity for researchers to publish their works.

Editorial Board Looks forewords to develop the journal and to promote it to be at the level of international scientific journals, and expand their reach circle to allow the largest possible number of interested to follow it by publishing all its issues through the internet web site.

Call for Papers

The Editorial Committee invites teaching staff members, postgraduate students, engineers, researchers and all those concerned with basic and applied sciences, and technology fields to submit their research work to be published in the journal. The journal publishes scientific papers (basic and applied research, review papers) technical reports, technical notes and book reviews in the mentioned fields.

Terms of Publication in the Journal

1. The papers and reports should be an original work and not considered for publication elsewhere. Papers published in conferences may be considered for publication in the journal after they go through the evaluation process and if they do not conflict with the copyright of the conference proceedings.
2. All papers and reports are subject to evaluation and may not be published unless all the required corrections are met and the author's guide for publication is followed.
3. The accepted papers could be written in Arabic (with English abstract), or in English (with Arabic abstract).
4. After acceptance of the paper or report for publication in the journal, it should not be considered for publication in another journal and the author should sign a copyright agreement with the editorial board of the journal.
5. Authors should include the full title of the paper, the author's full name, Author's affiliation and address, e-mail address.
6. Papers not written according to the stated instructions will not be considered for refereeing.

Typing Instruction

In spite that an electronic paper template is available, Authors are kindly requested to abide by the following instructions:

1. Manuscripts should not exceed 10 (A4) pages including figures and tables, produced using Microsoft word, with Times New Roman font 9.5pt single space typewritten. The page setup left and right margins of 13.5 mm and top margin of 25.4 mm and bottom margin of 21.8 mm.
2. The original and two copies should be submitted, and on a CD disc. The file on the disc should exactly correspond to the hard copies.
3. Authors have to the following format:
 - a. **Title page**, headed by a concise but informative full title font size 15pt**bold**, name(s) font size 12pt, and address of the place where the work was carried out font size of 8pt.
 - b. **Abstract**, containing brief but informative details of the contents and conclusions of the paper and should not exceed 200words, size 8.5.
 - c. **Introduction**, stating the reasons for carrying out the work, size of 9.5pt.
 - d. **Materials and Methods**, containing sufficient experimental details so that methods can be reproduced by researchers (in experimental papers), size 9.5pt.
 - e. **Results** should be described as concise as possible, size of 9.5pt.
 - f. **Discussion** should not recapitulate results in detail or contain new information but should emphasize the relevance and significance of the findings reported, size of 9.5pt.
 - g. **Conclusion**, size of 9.5pt.
 - h. **Acknowledgement**, size of 9.5pt.
 - i. **References** should be cited in the text a number in square brackets []. All references should be included at the end of the manuscript successively with size of 8pt. Correct references are the responsibility of the author.

Notes

1. the Journal has the right to publish these researches and makes use of them in scientific fields without referring to their owners, provided always referring to the owners of these studies/research according to generally accepted rules.
2. Manuscripts submitted for publication does not respond to their owners, whether published or not, the applicant is not entitled to claim them.
3. Editors of the journal reserve the right to make editorial changes in any manuscript accepted for publication for the sake of style or clarity. Authors will be consulted only if the changes are substantial.
4. Author/s must pay all the expenses incurred in the review process if s/he decides to withdraw his/her research paper whilst it is undergoing review.

Contents

English Part

Research Papers	Page
Effect of Roughness, Compliance and Adhesion on Perception of Softness Salima Abreiak , Raymond Holt, and Brian Henson	1
Experimental Assessment of The 100 mV Polarization Shift Criterion for Cathodic Protection Systems of the Prestressed Concrete Cylinder pipes Belied S. Kuwairi, and Hisham A. Elfergani	11
Thermal Efficiency Evaluation of Souk Elkhamis Cement Rotary Kiln Hussam El-Din F. El-Sheikh and Suliman A. Shaibi	18
Using Hazard-Based Duration Models to Investigate the Impacts of RUC on Libyan Drivers Travel Patterns Aziza.Safour	24
An Implementation of Fuzzy Logic Technique to Predict the Material Removal Rate in Abrasive Water Jet Machining Process Omar M Elmabrok, and Abdel Aziz M Badi	30
Dynamic Performance of a Sensorless Speed Control for Induction Motor Drives Based on Model Reference Adaptive System Haytham Mustafa, Saad. M. Saad, N. El-Naily, Salwa Almoshity, and Mohamed A. Almaktar	34
Modelling and Simulation of Multistage Flash Desalination Plants Wael Abu jazyah	43
Economic Evaluation of Mixed C4's Upgrading Processes. (Raslanuf Ethylene Plant as a Case Study) Isam A.B. Salem	48
A Comparative Study for the Effects of Synthetic Diesel Fuels on the Performance and Emissions of A Single Cylinder DI Diesel Engine Mansour N. Elhemri, Iman K. Reksowardojo, Kanit Wattanavichien, and Wiranto Arismunandar	52
Totally Volume Integral of Fluxes for Discontinuous Galerkin Method (TVI-DG) II-One Dimensional System of Equations E. I. Elhadi and I. M. Rustum	60

Effect of Roughness, Compliance and Adhesion on Perception of Softness

Salima Abreiaik ^{a*}, Raymond Holt ^b, and Brian Henson ^c

^a School of Industrial and Manufacturing systems Engineering, University of Benghazi, Benghazi, Libya

^{b & c} School of Mechanical Engineering, University of Leeds, Leeds, United Kingdom

* Corresponding author e-mail: sama_mima_2006@yahoo.com

ABSTRACT

This paper concerns the perceived softness of objects, which is an important aspect of haptic perception. To design tactile displays, there are many unanswered questions about human touch perception and its relationship with material properties. This paper explores how the interaction of material properties affects perception of softness through the use of two psychophysical experiments. The first experiment used a set of nine stimuli representing three materials of different compliance, embossed with three different patterns to vary their surface roughness. The second used three materials of different compliance with three different coatings to vary their stickiness. Magnitude estimation was used to assess the perceived softness for the stimuli in both experiments under two conditions: pressing into the stimulus with the finger, and sliding the finger across the stimulus. The results indicated that compliance affected perception of softness when pressing the finger, but not when sliding; and that compliance, friction and thermal conductivity all influenced the perception of softness. This work is an essential step to understand interactions between compliance and other material properties. The new knowledge can be applied to the design of tactile displays for laparoscopic surgery.

Keywords: human perception, softness, compliance, roughness, stickiness, tactile displays.

1. Introduction

There are many situations in which being able to judge the softness or hardness of a surface is important. Surgery is one example, where tumours are detected by palpitation, looking for harder patches amongst softer, healthy tissue. Yet we know that mechanisms by which the body detects material properties can be influenced by other factors (Ottermo, 2006, Gersem, 2005). This can be important both in terms of determining how human judgements of material properties, such as softness, can be affected by other factors, and also in accurately reproducing sensations through tactile displays, which are proposed for use in situations such as laparoscopic surgery, where direct tactile feedback is not available (Ottermo, 2008). This paper investigates how subjective human perception of material softness, is affected by the compliance, roughness and adhesion of a given material.

A range of studies has explored the relationship between surface properties and human perception of them. (Hollins et al., 1993) identified hardness-softness as one of the main subjective responses used by humans to discriminate surfaces, the other being roughness-smoothness. However, subjective perception of roughness and softness can be affected by more than one physical parameter ((Bergmann Tiest and Kappers, 2006), Shao et al. (2009)). For example, Chen et al. (2009a) found that judgements of hardness-softness depended on both compliance and cooling rate. Perceptions of softness or hardness can also be affected by factors such visual feedback and the mode of interaction (static or dynamic touch, for example) (Koçak et al., 2011, Harper and Stevens, 1964, Srinivasan and LaMotte, 1995). Harper and Stevens (1964) were able to relate the objective measure (compliance) and the subjective sensation (perceived softness) by building a quantifiable model of compliance discrimination using numerical ranking of perceived softness. This study has one shortcoming, that compliance was quantified without control of surface texture. This means that the influence of texture for the

different materials and surface properties on the subjective ranking of compliance is uncertain. The softness and hardness depended on the degree to which the object conforms to the body and to which the body conforms to the object respectively. This means that different kinds of sensory information are used to assess the soft versus hard objects (Friedman et al., 2008). The aim of this paper is to determine whether some of the interactions exist between the physical properties which effect the subjective perception. The same investigation was performed earlier (Shao et al., 2010), however, the experiments in this study were conducted with better experimental designed, and under more restricted control. This paper presents two experiments intended to further this exploration of the interaction between perceived softness and physical properties, by exploring the effect of roughness and stickiness on perceived softness.

2. Methodology

The goal of the first experiment (effect of surface roughness on perceived softness) was to determine whether surface roughness affected the perceived softness of a material. To do this, a set of experimental stimuli were created that represented different textures indented into different materials using magnitude estimation, and participants were asked to rate the softness of each texture by running their finger across it and by pressing their finger into it (as shown in Figure 1).

The second experiment (effect of adhesion and compliance on perception of softness) aimed at characterizing how surface adhesion and compliance affect the perception of softness. To accomplish this aim, there are several methods that could be used, but the method applied is magnitude estimation, which is fully explained later, by varying the level of stickiness of each sample.

2.1. Participants

Twenty four participants took part in each experiment (7 females and 17 males for first experiment and 11 females

and 13 males for second experiment), their age ranged between 20 and 49. Through a handedness inventory questionnaire was adapted from the handedness questionnaire by Briggs and Nebes (1975). They completed at the laboratory, all of the participants were found to be right handed for each experiment but one the left handed participant was a male in his twenties in first experiment. None of the subjects reported any neurological or physical injury that affected sensitivity of the index figures of both hands. The experiments were approved by the Faculty Research Ethics Committee at University of Leeds.

2.2. Stimuli

For first experiment, nine stimuli were made for first experiment, representing all combinations of three different levels of compliance and three different levels of roughness. Stimuli were produced in square 100mm × 100mm plaques, 10mm thick. These were made using a hot pressing process from thermoplastic polyurethane material of varying hardnesses (IROGRAN A 60 E 4902, PS455-203, PS440-200). Samples of stimuli are shown in Figure 2. Three textured aluminium sheets with different surface roughness were used to impress the plaques with different textures as shown in Figure 3.

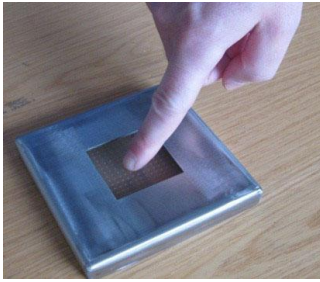


Fig. 1: Stimulus during touching.



Fig. 2: Sample of stimuli made of thermoplastic polyurethane.



Fig. 3: Textured aluminium sheets (a) vertex: mill finish textured sheet, (b) flat plain aluminium sheet: anodised finish sheet and (c) sheet was made using the shot blast method

For the second experiment, a nine stimuli set representing all combinations of three levels of compliance and three levels of adhesion were created for each stimulus. Stimuli were varied by mixing platsil gel 10 parts A and B

with different amounts of plasticizer. Moreover, platsil, plasticizer and toluene were mixed and applied in a thin layer of stickiness on the surface of softer blocks. A sample of stimuli is shown in Figure 4.

2.3. Method

In both experiments, the magnitude estimation procedure was used to quantitatively scale participants' perceptions of the softness of the different stimuli.

In the first experiment, the experimental approach used was to develop 3*3 general full factorial designs with the counterbalanced design for four conditions (Pressing and Sliding). These conditions requires 24 orders (4*3*2*1) in which they can occur (Field, 2010). So, Participants were divided into 2 groups to have an equal number of participants in each group; it means that 12 participants were in each group. Within each block, the order of presentation of stimuli was randomised. The two-way repeated measures analysis of variance was carried out with the magnitude estimates of perceived softness as dependent variables and compliance levels and roughness levels, as independent variable, to explore relations between the perception of softness and roughness.

In the second experiment, the experimental approach used was to develop 3*3 randomized complete block factorial designs with the counterbalanced design for four conditions (rating softness through pressing, rating stickiness through pressing, rating softness through sliding, rating stickiness through sliding). These conditions requires 24 orders (4*3*2*1), that can occur (Field, 2010). So, participants were divided into 24 groups to have an equal number of participants in each group; it means one participant was in each group. Within each block, the order of presentation of stimuli was randomised. The two-way repeated measures analysis of variance was carried out with the magnitude estimates of perceived softness as dependent variables and softness levels and stickiness levels to explore relations between the perception of compliance and stickiness.



Fig. 4: Sample of stimuli made of silicone and deadener.

2.4. Procedure

Participants took part in this study individually, so that they did not influence each other in their responses. Participants were asked to rate eight of the stimuli against a reference stimulus (Stimulus E) under two different conditions: by pressing into the stimulus with their finger, and by sliding their finger across it. Textures were placed behind a curtain, so that participants could not see the stimuli, to prevent visual feedback interfering with the tactile perception. Two textures were presented at a time: the reference stimulus, and the test stimulus. These were always located in the same position, so that participants knew which was the reference and which was the test stimulus. The two touching conditions (pressing and

sliding) were blocked and counterbalanced. Within each block, the order of presentation of stimuli was randomised.

The same reference stimulus was used in every case, and participants were asked to give a rating for the softness of the test stimulus using a magnitude estimation process (Lodge, 1981). The participant was told that the reference stimulus had a softness of 20, and asked to assign a rating to the test stimulus such that 40 would indicate twice as soft and 10 half as soft as the reference. Participants could go back and forth between the test and reference stimulus as often as desired before assigning a rating. Stimulus was presented three times for each participant, and the geometric mean was calculated for pressing and sliding condition.

Before starting, each participant wiped his/her fingertip with hand hygiene wipes to clean up sebum and dusts and help them revive their fingers. The stimuli set were also cleaned with a mild surface cleaner (non bleach, no taint and no odour) to ensure constant stimuli intensity. Participants were allowed to rest at any point during the experiment, if necessary. After each condition, the participant was allowed to rest for as long as they needed: the rest times ranged from 0-5 min. The experiment lasted for approximately 40- 45 minutes (mean=42 min and standard deviation = 1.85) and the full study was performed within 6 weeks.

The second experiment was carried out using a similar procedure to the previous experiment. During the experiment, participants touched the stimulus under four touch conditions: rating softness through pressing, rating stickiness through pressing, rating softness through sliding and rating stickiness through sliding. After each condition, the participants were allowed to rest for a period of time depending on the participant. The time ranged between (0-6) min. Participants could not see the stimuli during both experiments and rest period. The total experimental time per participant was between 18 minutes and 58 minutes (mean = 35.08 minutes and standard deviation = 9.71) and full study was performed within 8 days.

2.5. Material properties measurement

For each stimulus (for first and second experiments), material properties were measured: compliance was measured using Tribometer (measured using the tribometer presented in (Shao et al., 2010)). The artificial fingertip was replaced by a steel ball of 10 mm diameter. The ball was pressed into the surface of each compliant stimulus and the load was recorded against time, the load should reach around 3N.

The roughness of the stimuli (for first experiment) was measured by contact surface profilometry, using a Talysurf machine with a standard 0.8mm cut-off. Arithmetical roughness R_a (μm), is most popular measure of roughness of the surfaces.

The friction coefficient of each stimulus (for first and second experiments) was measured using a tribometer. For friction measurement, each sample was pressed and slid by forces F_y , F_x respectively were recorded against time. The force applied on each sample was 0.5N.

The thermal conductivity measurement (for first and second experiments) was also measured using the tribometer. The room temperature was recorded by running the program in LabVIEW system during one minute. The

fingertip temperature was set up to be +10oC. After setting up the temperature, a force of 1N was applied to make fingertip contact with the stimulus.

In case of measuring stickiness (for second experiment), the artificial fingertip was attached. The contact force was 1N for stickiness.

All measurements were repeated three times at different points across the stimulus and the average obtained.

3. Results

3.1. Results of first experiment

A two-way repeated measure ANOVA was conducted using SPSS to explore relations between the human tactile perception and roughness and to find whether there is interaction between two factors within each condition; this section reviews the results for each condition in turn.

• Pressing condition

Mauchly's test [14] indicated that the assumption of sphericity is violated for the main effects of softness, $\chi^2(2) = 41.62$, $p < 0.05$, roughness, $\chi^2(2) = 43.20$, $p < 0.05$ and interactions between softness and roughness, $\chi^2(9) = 20.67$, $p < 0.05$ and so correction of the F-ratio was required for the main effect of softness, roughness and the interactions. Therefore, degrees of freedom were corrected using Greenhouse-Geisser estimates of sphericity ($\epsilon = 0.69$ for the main effect of softness, 0.69 for the main effect of roughness and 0.88 for main effect of interaction between softness and roughness) [14].

All effects are reported as significant at $p < 0.05$. The two-way repeated measures ANOVA indicated that there was a significant main effect of compliance on the perception of softness, $F(1.38, 98.05) = 39.39$. This indicated that when the roughness level was ignored, the perception of softness were significantly differentiated according on the softness levels. There was a significant main effect of level of roughness on the perception of softness, $F(1.37, 97.23) = 26.11$. There was no significant interaction effect between the level of softness and the level of roughness used, $F(3.53, 250.50) = 2.45$, $p > 0.05$.

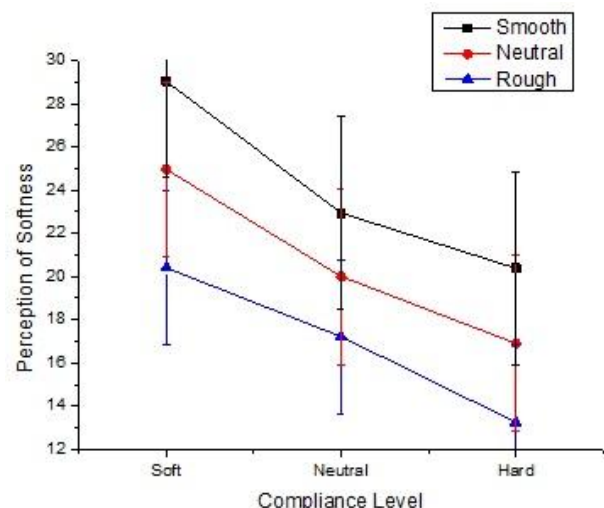


Fig.5: Perceived softness vs compliance at different levels of roughness during pressing condition.

Fig. 5 shows the geometric means for reported softness as a function of compliance in the pressing condition,

standard deviation error bar and how this varied with the different roughness conditions.

• *Sliding condition*

Mauchly's test indicated that the assumption of sphericity had been violated for the main effects of softness, $\chi^2(2) = 9.37, p < 0.05$. Moreover, it had been violated for the main effects of roughness, $\chi^2(2) = 12.40, p < 0.05$; also for the main effects of interactions between softness and roughness, $\chi^2(9) = 43.89, p < 0.05$. So correction of the F-ratio was required for the all effects of softness, roughness and their interaction. Therefore, the degrees of freedom were corrected using Greenhouse-Geisser estimates of sphericity ($\epsilon = 0.89$ for the main effect of softness, 0.86 for the main effect of roughness and 0.76 for the main effect of interaction between softness and roughness).

From the tests of within subjects effects, there was a significant main effect of compliance on the perception of softness, $F(1.78, 126.19) = 11.57$. There was also significant main effect of level of roughness on the perception of softness, $F(1.72, 122.17) = 22.15$, to conclude that there was significant effect of roughness on perception of softness.

There was no significant interaction between the level of softness and the level of roughness used, $F(3.05, 216.33) = 1.84$ on perceived softness. This indicates that roughness had not different effects on perception of softness on different level of softness used for sliding condition.

Figure 6 shows the geometric means for reported softness as a function of compliance in the sliding condition, standard deviation error bar and how this varied with the different roughness conditions. Perceived softness against compliance for both conditions is shown in Figure 7.

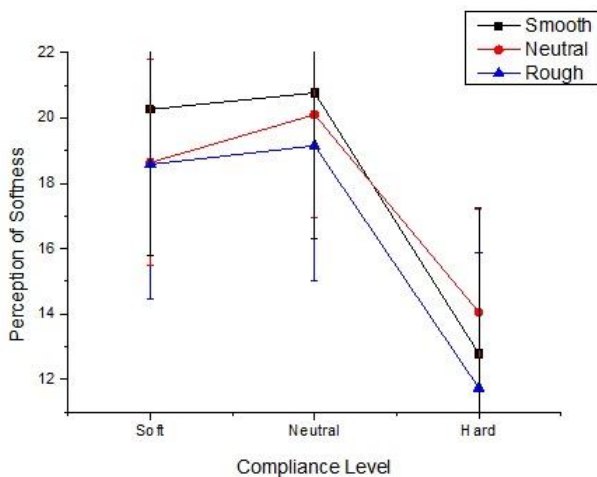


Fig.6: Perceived softness vs compliance at different levels of roughness during sliding condition.

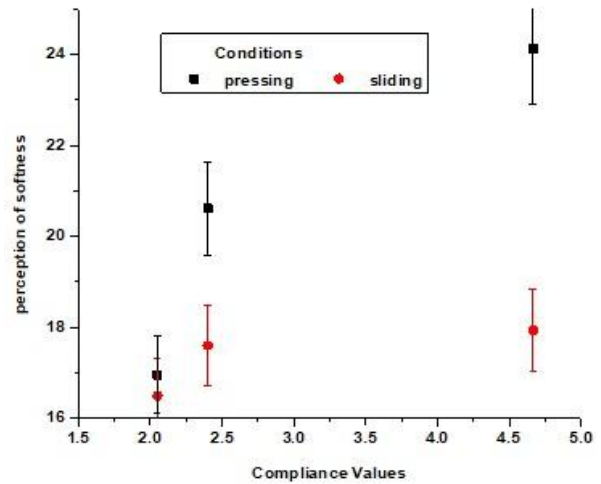


Fig.7: Perceived softness vs compliance.

To examine whether people could discriminate between different softness; the pairwise method was used to collect the data which compares between differences samples at same surface roughness. The results were analysed by Chi-square test to find out if there is any differences among samples. Since the significant value is 0 (which is less than 0.05), there is a significant difference between the levels of softness. It means that participants can distinguish between different compliance for all surface roughness. Table 1 shows the results of Chi-square test.

In order to examine the relationship between physical measurements and softness perception, a Pearson correlation coefficient was computed to assess the relationship between physical properties with perceived softness for both conditions, as shown in Table 2. Also, a regression analysis was used to draw this relationship between perceived softness and physical properties. The results showed that the perception of softness for pressing condition was contributed by compliance as found in previous studies (Shirado and Maeno, 2005, Bergmann Tiest and Kappers, 2006). This means that the perceived softness can be predicted by compliance and as being shown in Table 3.

A Pearson correlation coefficient was computed to assess the relationship between the physical properties with each other. There were not correlations between each physical property with other physical properties. Table 4 summarizes the results.

Table 1: Chi-square analysis for distinguish between softness of stimuli during pressing.

	Pearson Chi-Square value	P Value
Compare between feeling softness at smooth surface	263.83	0.00001
Compare between feeling softness at natural surface	156.1	0.00001
Compare between feeling softness at rough surface	212.35	0.00001

Table 2: Correlations between physical properties and perceived softness during pressing and sliding

	Compliance (mm/3N)	Averaged of measured Roughness (Ra) μm	Friction coefficient (μ)	Heat transfer (°C/sec)
Perceived softness (pressing condition)	0.750*	-0.083	-0.458	0.07
Perceived softness (sliding condition)	0.300	0.618	-0.74*	0.181

* Correlation is significant at the 0.05 level

Table 3. Beta coefficients of regression of perceived softness during pressing and sliding

Model	Perceived softness (pressing)	Model	Perceived softness (sliding)
	Coefficient		Coefficient
Measured compliance	0.750	Friction coefficient	-0.736

Table 4: Correlations between physical properties

	Compliance (mm/3N)	Averaged of measured Roughness (Ra) μm	Friction coefficient (μ)	Heat transfer (°C/sec.)
Compliance (mm/3N)	1	-0.01	-0.17	-0.29
Averaged of measured Roughness (Ra) μm	-0.01	1	-0.45	.22
Friction coefficient (μ)	-0.17	-0.45	1	-0.32
Heat transfer (°C/sec.)	-0.29	.22	-0.32	1

Correlation is significant at the 0.05 level

3.2. Results of second experiment

A two-way repeated measure ANOVA was conducted using SPSS to explore relations between the human tactile perception and stickiness and to find whether there is interaction between two factors within each condition; this section reviews the results for each condition in turn.

- *Perception of softness (through pressing condition)*
Mauchly's test indicated that the assumption of sphericity had been violated for the main effects of softness, $\chi^2(2) = 69.41, p < 0.05$, stickiness $\chi^2(2) = 7.08, p < 0.05$; and

interactions between softness and stickiness, $\chi^2(9) = 47.91, p < 0.05$. so correction of the F-ratio was required for the main effect of softness, stickiness and the interactions stickiness. Therefore, degree of freedom were corrected using Greenhouse-Geisser estimates of sphericity ($\epsilon = 0.56$ for the main effect of softness, 0.88 for the main effect of stickiness and 0.66 for the main effect of interaction between softness and stickiness).

All effects are reported as significant at $p < 0.05$. There was a significant main effect of compliance on perceived softness, $F(1.12, 25.86) = 107.32$. There was no significant main effect of level of stickiness on the perception of softness, $F(1.75, 40.29) = 0.56$. There was no significant interaction effect between the level of softness and the level of stickiness used, $F(2.65, 60.88) = 2.57, p > 0.05$. Figure 8 shows the geometric means for reported softness as a function of compliance in the pressing condition, standard deviation error bar and how this varied with the different stickiness conditions.

In short, the analysis demonstrates that compliance and stickiness do not significantly affect perceived softness for this condition.

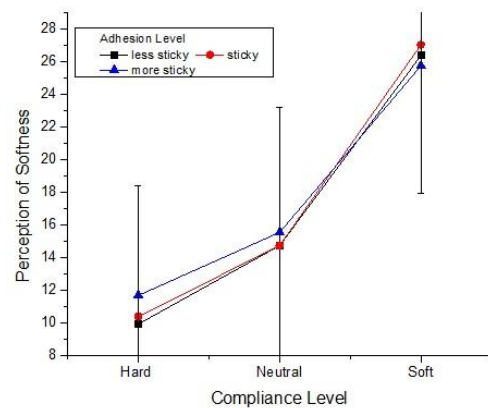


Fig8: Perceived softness vs compliance at different levels of adhesion during pressing conditions.

- *Perception of stickiness (through pressing condition)*
Mauchly's test indicated that the assumption of sphericity is met for the main effects of softness, $\chi^2(9) = 2.02, p > 0.05$, but the assumption had been violated for the stickiness, $\chi^2(9) = 10.13, p < 0.05$ and interactions between softness and stickiness, $\chi^2(9) = 14.33, p > 0.05$ and so there is a need to correct F-ratio for these effect, degrees of freedom were corrected using Greenhouse-Geisser estimates of sphericity ($\epsilon = 0.0.84$ for the main effect of stickiness and 0.86 for the main effect of interaction between softness and stickiness).

From the tests of within subjects effects, there was no significant main effect of softness on the perception of stickiness, $F(1.92, 90.13) = 2.82$. There was also non-significant main effect of level of stickiness on the perception of stickiness, $F(1.67, 78.49) = 2.38$, to conclude that there was non-significant effect of stickiness on perception of softness.

There was no significant interaction between the level of softness and the level of stickiness used, $F(3.46, 162.37) = 1.58$. The geometric means for reported softness as a function of compliance in the pressing condition are shown in Figure 9.

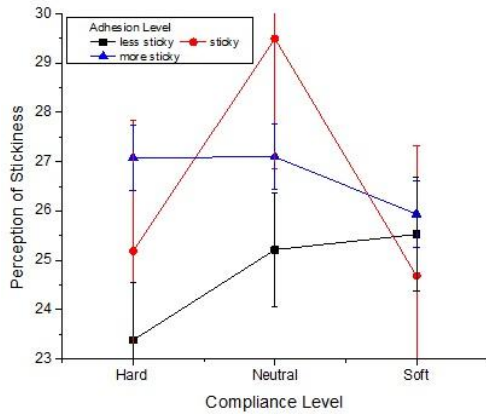


Fig. 9: Perceived stickiness vs compliance at different levels of adhesion during pressing conditions.

• Perception of softness (through sliding condition)

In this condition, Mauchly’s test indicates that the assumption of sphericity had been violated for the main effects of softness, $\chi^2(9) = 59.73, p < 0.05$ and the interaction between compliance and stickiness, $\chi^2(9) = 62.14, p < 0.05$. Therefore, degrees of freedom were corrected using Greenhouse-Geisser estimates of sphericity ($\epsilon = 0.58$ for the main effect of softness and 0.61 for the main effect of interaction between softness and stickiness).

The results show that there was non-significant interaction effect between the level of softness and the level of stickiness used, $F(2.42, 113.65) = 0.64$, indicating that both softness and roughness had the same effects on participants’ ratings. To sum up, there was no significant interaction between the levels of stickiness and level of softness for perceiving softness.

Simple main effects analysis showed that there was a significant main effect of softness on the perception of softness, $F(1.16, 54.43) = 65.58$. This effect revealed if the different levels of stickiness were ignored, perception of softness of different levels of softness were different.

There was significant main effect of level of stickiness on the perception of Softness, $F(1.84, 86.59) = 3.62$ with stickiness level, to conclude that the main effects of stickiness do not perceive softness significantly (Figure 10).

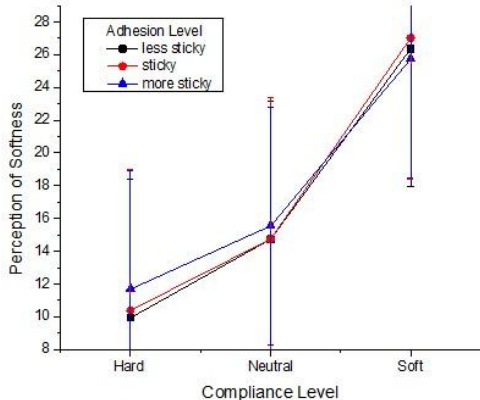


Fig. 10: Perceived softness vs compliance at different levels of adhesion during sliding conditions.

• Perception of stickiness (through sliding condition)

In the fourth condition, Mauchly’s test indicates that the assumption of sphericity had been violated for the main effects of softness, $\chi^2(9) = 25.48, p < 0.05$, the main effects of stickiness, $\chi^2(9) = 54.20, p < 0.05$ and interactions between softness and stickiness, $\chi^2(9) = 45.51, p < 0.05$. Therefore, degrees of freedom were corrected using Greenhouse-Geisser estimates of sphericity ($\epsilon = 0.70$ for the main effect of softness, 0.54 for the main effect of stickiness and 0.74 for the main effect of interaction between softness and stickiness).

The results show that there was no significant interaction effect between the level of softness and the level of stickiness used, $F(2.96, 139.18) = 1.60$, indicating that a given level of softness, the perception of stickiness does not change significantly for all levels of stickiness. These interactions are shown in Figure 11 due to the interaction of the three lines. To sum up, there was non-significant interaction between the levels of stickiness and level of softness for perceiving softness. The perception of softness due to levels of softness compared to levels of stickiness is not affected by whether stimuli are soft or hard.

Simple main effects analysis showed that there was a significant main effect of softness on the perception of softness, $F(1.40, 65.95) = 36.39$. This effect indicates that the different levels of softness used had a different effect on the perception of stickiness when the levels of stickiness were ignored.

There was also a significant main effect of level of stickiness on the perception of stickiness, $F(1.18, 55.55) = 27.99$. To conclude that this effect revealed that if the different levels of softness were ignored, perception of stickiness of different levels of softness was different according to different levels of stickiness (Figure 11). Figure 12 shows Perceived softness against compliance for both conditions.

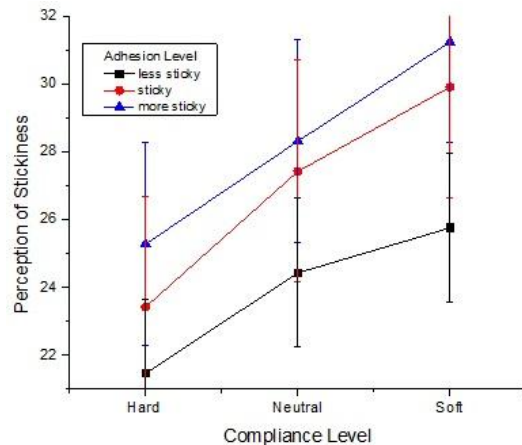


Fig. 11: Perceived stickiness vs compliance at different levels of adhesion during sliding conditions.

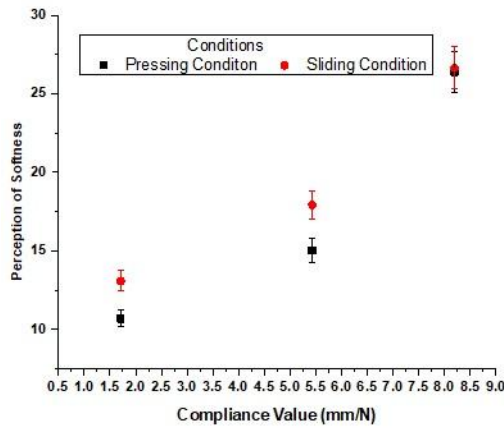


Fig. 12: Perceived softness vs compliance.

Further analysis is to determine whether, for each stickiness level, participants appeared to distinguish between the softness of the stimuli through both conditions, using One-way ANOVA analysis. The results show that the perception of softness was significantly affected by softness for all levels of stickiness. The values of F test and p values are shown in Table 5 for pressing and sliding conditions.

The results of correlation between physical properties and perception of softness and stickiness during two conditions (pressing and sliding) are shown in Table 6. This means that the perceived softness or stickiness can be predicted by these physical properties and it can be expressed as given in Table 7.

A Pearson correlation coefficient was computed to assess the relationship between the physical properties with each other. There were strong, negative correlations between compliance and friction coefficient and between compliance and heat transfer and no correlations between other physical properties with each other. Table 8 summarizes the results.

Table 5: One- Way ANOVA analysis for distinguishing between softness of stimuli during pressing and sliding condition.

Level of softness	Pressing condition		sliding condition	
	F(2,71)	P value	F(2,71)	P value
Stickiness level 1 compare different level of softness	38.43	0.00	26.31	0.00
Stickiness level 2 compare different level of softness	59.83	0.00	35.55	0.00
Stickiness level 3 compare different level of softness	55.58	0.00	37.93	0.00

Table 6: Correlations between physical properties and perceive softness and stickiness for pressing and sliding.

	Compliance	Stickiness	Friction coefficient (μ)	Heat transfer
Perceived softness (pressing condition)	0.932*	-0.14	-0.51	-0.89*
Perceived stickiness (pressing)	-0.01	-0.52	-0.44	0.28

condition)				
Perceived softness (sliding condition)	0.94*	-0.09	-0.56	-0.87*
Perceived stickiness (sliding condition)	0.77*	-0.69*	-0.75*	-0.65

Table 7: Coefficients of regression of perceived softness and stickiness during pressing and sliding.

Model	Preceived softness (pressing)	Preceived softness (sliding)	Preceived stickiness (sliding)
	Coefficient	Coefficient	Coefficient
Measured compliance	0.656	0.801	0.575
Measured stickiness	0	0	-0.556
Friction coefficient	0	0	-0.172
Heat transfer	-0.312	-0.159	0

Table 8: Correlations between physical properties

	Compliance	Measured stickiness	Friction coefficient	Heat transfer
Compliance	1	-.14	-.69*	-.89**
Measured stickiness	-.14	1	.31	.06
Friction coefficient	-.69*	.31	1	.38
Heat transfer	-.89**	.06	.38	1

4. Discussion and conclusions

The aim of this experiment was to establish whether the interaction between surface roughness and compliance could influence the perception of softness. Across the two conditions tested (pressing and sliding), there was a strong outcome that interaction between roughness and compliance does not affect the perception of softness. In this section the main findings are summarized and their implications discussed.

The main result of first experiment was that the compliance × roughness interaction had no significant effect on perceived softness; this was true for both pressing and sliding conditions. There was no evidence that interaction between compliance and roughness affected perceived softness. This may be because of frictional forces between the finger tips and the stimulus or because of small differences between compliance levels of samples. The amount of deformation that fingers undergo during pressing may be one reason, because it depends on the contact force and how stiff the material compared is to a finger.

The main result of second experiment was that interaction between compliance and adhesion do not significantly affect perceived softness and perceived stickiness during pressing or sliding touch. It means that both compliance and adhesion had the same effects on participant responses depending on which condition was being employed. There was no evidence that the interaction between compliance and adhesion affected perceived softness. A possible explanation for this might be that the

frictional force between the fingertips and the stimulus; those forces have an important role in perception of softness. When the compliance increased, the force decreased. It means the force variation is dependent on the different compliances (Kaim and Drewing, 2009). The force differed from one participant to another. Another possible explanation for this is the surface deformation. It depends on the contact force and how stiff the material is compared to a finger, but in the present study all stimuli materials were less stiff than a finger. Also, another reason is that the stimuli's dimensions may influence compliance but those are the same in the present work. Another possible explanation for this is that the contact area between the finger and the stimulus might affect the participants' perception of softness and stickiness. This result may be explained by the fact that the important factor which affects perception of softness is cutaneous sensation. The cutaneous information is located within the skin which provides tactile feedback. Moreover, the cutaneous information alone is sufficient to discriminate the compliance of objects with deformable surfaces (Srinivasan and LaMotte, 1995).

Referring to Figure 9, the results of the sticky stimuli are presented. These results were completely unexpected; given that it is possible that participants cannot distinguish the stickiness by pressing. A possible explanation might be that stickiness seems to be detected through dynamic touch rather than a static touch. Bergmann Tiest et al. (2012) pointed out that people could detect stickiness through dynamic touch.

However, participants were able to distinguish between the levels of softness for each adhesion level or roughness level, in agreement with a previous study on perception of softness, (Yoshioka et al., 2007).

Nevertheless as first experiment shows, participants were able to distinguish between the compliance for each roughness level and for each stickiness level. This is in agreement with a previous study on the perception of softness (Srinivasan and LaMotte, 1995), which showed that perception of softness might depend on the objective compliance of the stimuli and people could discriminate softness easily through active touch. Our results are in agreement, since the compliance was largely determined by the influence of other material properties. The comparison of these results with previous findings shows very similar judgements on the relationship between perceived softness and physical hardness, as well as no significant effect between perception of softness and interaction between compliance and roughness surface as well as interaction between compliance and stickiness.

The results of first experiment showed that perception of softness was affected by compliance for the pressing condition. This finding is in agreement with previous studies (Shirado and Maeno, 2005, Bergmann Tiest and Kappers, 2006).

The findings of the first experiment seem to be consistent with other research (Petrie et al., 2004) which found that the relationship between the perception of smoothness of a surface and the physical hardness of the samples was not significant, and the interactions with other variables (such as surface shape) were also not significant. Moreover, the present finding is also in agreement with

Shirado and Maeno (2005) who showed the influence of elasticity for different materials on the tactile sense.

However, these results of first experiment differ from some published studies (Bergmann Tiest and Kappers, 2006, Shao et al., 2009, Chen et al., 2009b), which found that the perception of softness relates to other material properties such as compliance.

It is difficult to explain this result of first experiment, but it might be related to the deformation of the material and the finger caused by the magnitude of friction forces when pressing and sliding on the surface. These friction forces have an important role in the perception of softness. Moreover, the stiffness of the material compared to a finger and the contact force with material affects the deformation of the material. Another explanation is that perceived softness depends on the force used for pressing the stimuli. The study by Friedman et al. (2008) found that participants press a hard object with more force than a soft object.

The results of second experiment showed that softness was largely influenced by other material properties. The results were compared with previous findings; these are the same in terms of the relationship between perceived softness and physical hardness. Moreover, the present findings seem to be consistent with other research which found that the influence of texture for different materials and surface properties on the subjective ranking of compliance is uncertain (Shirado and Maeno, 2005).

Even though the findings of the second experiment support previous research (Shao et al., 2009, Chen et al., 2009b), they are consistent with those of touch perception being related to more than one physical property. They are consistent with the perception of stickiness being associated with compliance and friction, and with the perception of hardness being related to thermal properties and compliance of the stimulus.

It is difficult to explain this result of second experiment. Sticky is a term not just related to friction but also related to more contact between a finger and a surface (Shao et al., 2009) and related to vibratory cues which contribute to perceiving stickiness (Bensmaïa and Hollins, 2005).

Further analysis is required to investigate how perception of softness is related to physical material properties. Linear regression analysis of first experiment was used to explore the relationship between perception of softness and physical material properties. The data show that there is a correlation ($r = 0.75, <0.05$) between the perceived softness and the measured physical compliance during the pressing condition. This seems to be consistent with the results of Shao et al. (2009). Perception of softness and compliance values seems to have a strong relationship (Petrie et al., 2004). However, there is only a weak effect ($r = 0.30, p > 0.05$) between the perceived softness and measured compliance during the sliding condition. Roughness and softness seem to be perceived differently. Roughness can be tracked by running the finger across the surface (sliding) and softness tracking by pressing the finger onto the surface. For this reason, the tactile display was built. As can be seen from the analysis, the mean of perceived softness was high in cases of high roughness. Perceived softness depends on the way stimuli are touched, how the contact area increases with contact force, the pressure over the contact area, and the force used

to press the stimuli (Bergmann Tiest, 2010, Johnson et al., 2000, Friedman et al., 2008).

In addition, the data indicated that there is a correlation ($r = -0.74$, $p < 0.05$) between the perceived softness and the friction coefficient during sliding conditions. In reviewing the literature, data were found on the association between perceived softness and friction coefficient (Chen et al., 2009c). However, the findings of the current study are inconsistent with those of Shao et al. (2010) who found that softness perception was related to compliance and thermal conductivity. Perhaps no correlation was found between softness perception and thermal conductivity because that condition was controlled, for example, dT/dt was made to be the same in every case.

Across the friction coefficients tested, there was no correlation ($r = -45$, $p > 0.05$) between the friction coefficient and measured roughness during both conditions, which shows that this finding is in agreement with results by Shao et al. (2009), (Shao et al., 2010). They reported that rough was related to the roughness of a surface. However, it appears to be different from results found by Skedung et al. (2011). Roughness and friction are inverse correlated. This means that perceived coarseness is less when the friction is high.

Linear regression analysis was used to explore the relationship between perception of softness and physical material properties in both conditions. Correlations between physical measurements of compliance and psychophysical perceptions of softness and stickiness are presented in Figure 10. From the results, there is a significant relationship between the perceived softness during pressing conditions and measured compliance which is highly correlated with each other and with heat transfer. Moreover, perceived softness during sliding conditions was significantly related to measured compliance and heat conductivity ($p < 0.05$). In addition, there was a significant correlation between perceived stickiness, compliance, adhesion and friction coefficient during sliding conditions ($p < 0.05$). However, perceived stickiness during pressing conditions was not significantly correlated with any physical properties. The results seem to be consistent with findings by Shao et al. (2009).

In order to examine the relationship between physical measurements and softness perception, a regression analysis was used. A feeling of softness depends on compliance and thermal conductivity, which are consistent with relationships identified by Shao et al. (2009). Their finding was that hardness perception was correlated with compliance and thermal conductivity. It seems this is because the properties depend on the material of stimuli or the condition used to manipulate the stimuli (Shao et al., 2009).

A feeling of stickiness depends on compliance, adhesion and friction which differs from the relationships identified by Shao et al. (2009) that sticky perception was correlated with friction and compliance. It also differs from the findings of Hollins and Risner (2000) which state that sticky perception depended only on friction. It seems this was because of the task applied or the material used. However, all relations appear to be in agreement with research done by Shirado and Maeno (2005) which draw together the relations between physical properties and people's perception. They found that perception of softness is related to modulus of elasticity and heat transfer property.

Unlike most previous work which studied relations between subjective and objective properties separately, Chen et al. (2009a) examined the combination of physical properties in relation to touch perception. This study included consideration of a range of material properties interacting to influence perception of material softness.

Regardless of the method of contacting the stimulus, by pressing or sliding, the subjective softness felt by a typical participant was very similar to the objective compliance. This means that softness correlates with compliance; it is the same as the results found by Shao et al. (2009). They reported that there was a correlation of thermal and compliance properties that is dependent on the materials of the stimuli. Perception of softness and Shore hardness values seems to have a strong relationship (Petrie et al., 2004).

An implication of this is the possibility that softness feelings could be presented through a tactile display using compliance of material. This finding may help to understand how to design an ideal tactile display which presents realistic softness feelings to the surgeon's fingertip.

The findings from the current analysis give answers to the study's research questions and help to achieve its goals, which are to investigate whether roughness and compliance or adhesion and compliance could affect the perception of softness. These findings have significant implications for the design of the tactile display, particularly for the purpose of presenting softness. The results obtained in these experiments may help developers to decide how to generate tactile sensations and how this information can be delivered to surgeons' fingertips.

5. Conclusion

Experiments were conducted to explore whether perception of softness is affected by interaction between compliance and surface roughness or interaction between compliance and adhesion. As a result from the experiments, it was found that the interaction between compliance and surface roughness do not significantly affect perceived softness for sliding or pressing conditions, indicating that both compliance and surface roughness had the same effects on participants' ratings. Also, interaction between compliance and adhesion does not significantly influence perceived softness for sliding and pressing conditions, indicating that both compliance and adhesion had the same effects on participants' ratings. Results from the first experiment, which used polyurethane stimuli to determine the effects of roughness and compliance on the perception of softness, confirm that perceived softness was related to compliance alone in the pressing condition, and friction coefficient alone in the sliding condition. However, in the second experiment, which used silicone stimuli to determine the effects of adhesion and compliance on the perception of softness, the perception of softness correlated with compliance, thermal conductivity and friction coefficients for both the pressing and sliding conditions. An explanation for this result could be because it was not possible to control the physical properties of the silicone stimuli independently; both thermal conductivity and friction coefficient correlated with the materials' compliance. For the polyurethane stimuli, it was possible to control the physical properties independently. The difference in results could also be because the silicone stimuli were similar in compliance to the human finger, and

the polyurethane stimuli were somewhat harder, and that perception of softness does indeed also depend on thermal and friction properties.

This work is an essential step towards understanding interactions between compliance and other material properties which affect perception of softness and how this understanding can be applied to the medical field, especially laparoscopic surgery.

Acknowledgment

This study is a part of a thesis for PhD of Mechanical Engineering 2014, conducted at School of Mechanical Engineering at University of Leeds. The authors would like to thank all participants for their contributions.

References

- [1] Beierholm Et Al., B., U., Kording, K., Shams, L., Ma, W.J., (2007). Comparing Bayesian Models For Multisensory Cue Combination Without Mandatory Integration. *Advances in Neural Information Processing Systems*, ed.^eds.
- [2] Bensmaïa, S. & Hollins, M. (2005). Pacinian Representations of Fine Surface Texture. *Attention, Perception, & Psychophysics*, 67, 842-854.
- [3] Bergmann Tiest, W. M. (2010). Tactual Perception Of Material Properties. *Vision Research*, 50, 2775-82.
- [4] Bergmann Tiest, W. M. & Kappers, A. M. (2006). Analysis of Haptic Perception of Materials By Multidimensional Scaling And Physical Measurements of Roughness And Compressibility. *Acta Psychol (Amst)*, 121, 1-20.
- [5] Briggs, G. & Nebes, R. (1975). - Patterns Of Hand Preference In A Student Population. *Cortex*, 11, 230-8.
- [6] Beierholm Et Al., B., U., Kording, K., Shams, L., Ma, W.J., (2007). Comparing Bayesian Models For Multisensory Cue Combination Without Mandatory Integration. *Advances In Neural Information Processing Systems*, Ed.^Eds.
- [7] Bensmaïa, S. & Hollins, M. (2005). Pacinian Representations of Fine Surface Texture. *Attention, Perception, & Psychophysics*, 67, 842-854.
- [8] Bergmann Tiest, W. M. (2010). Tactual Perception of Material Properties. *Vision Research*, 50, 2775-82.
- [9] Bergmann Tiest, W. M. & Kappers, A. M. (2006). Analysis of Haptic Perception of Materials By Multidimensional Scaling And Physical Measurements of Roughness And Compressibility. *Acta Psychol (Amst)*, 121, 1-20.
- [10] Chen, X., Shao, F., Barnes, C., Childs, T. & Henson, B. (2009a). Exploring Relationships Between Touch Perception And Surface Physical Properties. *International Journal Of Design* 3, 67-76.
- [11] Chen, X., Shao, F., Barnes, C., Childs, T. A. & Henson, B. (2009b). Exploring Relationships Between Touch Perception And Surface Physical Properties. *International Journal of Design* 3, 67-76.
- [12] Field, A. (2010). *Discovering Statistics Using Spss Introducing Statistical Methods Series*, United Kingdom, Sage Publications Ltd.
- [13] Friedman, R. M., Hester, K. D., Green, B. G. & Lamotte, R. H. (2008). Magnitude Estimation of Softness. *Exp Brain Res*, 191, 133-42.
- [14] Gersem, G. D. (2005). *Kinaesthetic Feedback And Enhanced Sensitivity In Robotic Endoscopic Telesurgery*. Ph.D., Katholieke Universiteit Leuven.
- [15] Harper, R. & Stevens, S. S. (1964). Subjective Hardness of Compliant Materials. *Quarterly Journal of Experimental Psychology*, 16, 204 - 215.
- [16] Hollins, M., Faldowski, R., Rao, S. & Young, F. (1993). Perceptual Dimensions of Tactile Surface Texture: A Multidimensional Scaling Analysis. *Percept Psychophys*, 54, 697-705.
- [17] Hollins, M. & Risner, S. R. (2000). Evidence For The Duplex Theory of Tactile Texture Perception. *Perception & Psychophysics*, 62, 695-705.
- [18] Johnson, K., Yoshioka, T. & Vega-Bermudez, F. (2000). Tactile Functions of Mechanoreceptive Afferents Innervating The Hand. *J Clin Neurophysiol*, 17, 539-58.
- [19] Koçak, U., Palmerius, K., Forsell, C., Ynnerman, A. & Cooper, M. (2011). Analysis of The Jnd of Stiffness In Three Modes of Comparison. In: Cooper, E., Kryssanov, V., Ogawa, H. & Brewster, S. (Eds.) *Haptic And Audio Interaction Design*. Springer Berlin Heidelberg.
- [20] Lodge, M. (1981). *Magnitude Scaling: Quantitative Measurement of Opinions*, Sage.
- [21] Ottermo, M. S., Ø. And Johansen, T. (2008). Design And Performance of A Prototype Tactile Shape Display For Minimally Invasive Surgery. *The Electronic Journal of Haptics Research* 4, 1-13.
- [22] Ottermo, M. V. (2006). *Virtual Palpation Gripper*. Ph.D Degree, Norwegian University of Science And Technology.
- [23] Petrie, H., King, N. & Tomlins, P. (2004). Investigations Into Sensation of 'Softness' And Perception of The Tactile Properties of 'Soft Touch' Thermoplastic Elastomers. . National Physical Laboratory.
- [24] Shao, F., Chen, X. J., Barnes, C. J. & Henson, B. (2010). A Novel Tactile Sensation Measurement System For Qualifying Touch Perception. *Proceedings of The Institution of Mechanical Engineers, Part H: Journal of Engineering In Medicine*, 224, 97-105.
- [25] Shao, F., Childs, T. H. C. & Henson, B. (2009). Developing An Artificial Fingertip With Human Friction Properties. *Tribology International*, 42, 1575-1581.
- [26] Shirado, H. & Maeno, T. (2005). Modeling of Human Texture Perception For Tactile Displays And Sensors. *Proceedings of The First Joint Eurohaptics Conference And Symposium On Haptic Interfaces For Virtual Environment And Teleoperator Systems*. Ieee Computer Society.
- [27] Skedung, L., DanerlāV, K., Olofsson, U., Michael Johannesson, C., Aikala, M., Kettle, J., Arvidsson, M., Berglund, B. & Rutland, M. W. (2011). Tactile Perception: Finger Friction, Surface Roughness And Perceived Coarseness. *Tribology International*, 44, 505-512.
- [28] Srinivasan, M. A. & Lamotte, R. H. (1995). Tactual Discrimination of Softness. *J Neurophysiol*, 73, 88-101.
- [29] Wouter, M. B. T. (2009). Cues For Haptic Perception of Compliance. *Ieee Transactions On Haptics*, 2, 189-199.

Experimental Assessment of The 100 mV Polarization Shift Criterion for Cathodic Protection Systems of the Prestressed Concrete Cylinder pipes

Belied S. Kuwairi ^a, and Hisham A. Elfergani ^{b*}

Faculty of Engineering, University of Benghazi, Benghazi, Libya

**Corresponding author. Tel.: +218-094-456-8085; e-mail: Hisham.elfergani@uob.edu.ly*

ABSTRACT

In this work, an experimental study was carried out to evaluate the 100 mV polarization shift criterion for confirming the effectiveness of applied cathodic protection viz via zinc sacrificial anodes to arrest progress of corrosion in uncorroded or partially corroded high tensile grade prestressing steel wires of the same grade as the one used to manufacture the prestressed concrete cylinder pipes (PCCP).

Total number of 14 wire samples were placed under constant tension approximately 55% of their ultimate tensile strength by the use of specially designed and fabricated holding metal frames. All samples were individually immersed in glass vessels filled with alkaline solutions of pH around 12 and variable chloride ions concentration ranging from 500 to 3000 ppm. With the exception of one wire sample left unprotected; the remaining samples were cathodically protected by systems of zinc sacrificial anodes such that an average measured polarization shift near 100 mV with variable chloride content in solution was maintained for 9 samples and near 75, 50, and 25 mV with constant chloride content of 3000 ppm.

Evaluation of mechanical properties of wire samples suggested that 100 mV criterion and more than sufficient to confirm the adequacy and effectiveness of zinc sacrificial anodes cathodic protection system to arrest progress of corrosion of partially corroded and uncorroded prestressing steel wires in alkaline passivating environment contaminated with chloride ions up to 3000 ppm in solution and for shifts in polarization as low as 25 mV.

It was also evident that corrosion progress in the prestressing steel wires can not be arrested in the 3000 ppm chloride environment without the application of cathodic protection.

Keywords: Corrosion , Cathodic protection , 100 mV Polarization shift criterion , Prestressed concrete .

1. Introduction

A large number of structures e.g. buildings , bridges ,dams, pressure vessels, strong tanks, piles, railway sleepers and nuclear reactor protective shells are made of prestressed concrete in which prestressing steel wires are put into a permanent state of tension to compensate for the inadequate tensile strength of the concrete. By prestressing the steel reinforcement, the concrete is placed under compression at normal working loads and hence it prevents tensile cracking in the concrete .Usually prestressing steel is 4-5 times stronger than mild steel.[1]

The optimum combination of high strength steel with high strength concrete makes prestressed concrete structural components lighter, stronger, and crack-free. Apart from the structural efficiency, it reduces the cost.

1.1. Construction of PCCP at Great Man-Made River Project

One of the single civil engineering projects of the 20th century is the great man made river project (GMRP) of Libya for water transportation for agriculture and industry. The cost of the transported under ground water from the aquifers in the Sahara desert to the coastal region will be substantially less than the desalination.

The project is aimed to convert thousands of hectares of semi-desert into rich fertile agricultural land leading Libya to become self sufficient in agriculture. The water will be available to manufacturing and processing industries. It will facilitate the expansion and growth of the industrial sector along the route of the pipeline.

The fresh potable water will be available to the inhabitants of many cities and villages along the pipeline route. The oil revenues have been made available to invest into the construction of GMRP to benefit all the community in this generation and for many generations to come. This project includes the state of the art construction facilities and a

control system to operate the pipeline as per the experts estimation the fresh water supply will be available for a period over 50 years and hence the design life of the pipelines is to last this long.[2]

1.2. Manufacturing of Pre-stressed Concrete Cylinder Pipe (PCCP):

PCCP is designed to take optimum advantage of the compressive strength and corrosion-inhibiting property of Portland cement concrete and mortar and the tensile strength of prestressing wire. Each conveyance line PCC pipe is generally 4.0 m in internal diameter, 7.5 m in length, and weights over 70 tones. The pipe consists of an externally prestressed post tensioned concrete core 225 mm thick within which is embedded a thin steel cylinder as a watertight membrane. The prestressing is applied to the cured concrete core by over-wrapping with high tensile steel wire at a close pitch under uniform tension, anchoring the wire at each end of the pipe. Prior to the wire wrapping, bonding strips are welded between the anchor points to short out the wire turns and there by facilitate cathodic protection when needed. Steel joint rings welded to each end of the steel cylinder form a spigot and socket joint within the pipe wall thickness between adjacent pipes. Supplementary steel reinforcement strengthens the pipe ends.

Two rubber gaskets at the spigot and socket joints provide a watertight and flexible joint with some freedom of longitudinal and angular movement. High strength cement mortar spray applied on to the prestressing wire wrap provides mechanical and basic corrosion protection of the steel wire. Typical cross-section of the PCCP is shown in figure 1.

The PCCP is rigid, and relies on its inherent strength to resist internal pressure and external soil and surface loadings. Pipe design is in accordance with AWWA.

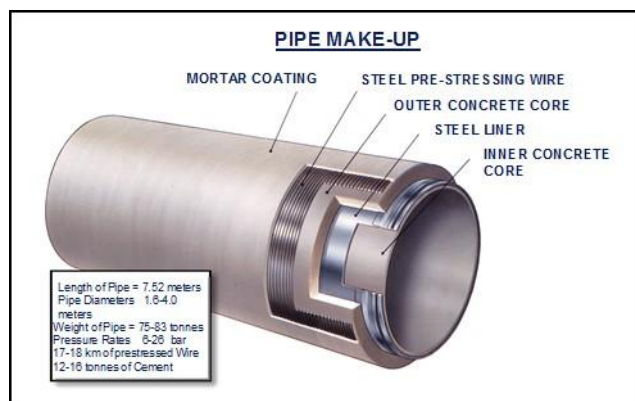


Figure 1 Typical Cross-Section of the PCCP

Standard C301. Pressure rating is based on the maximum steady state operating pressure plus a safety margin of 5 meters head of water, and accommodates transients up to 140% of rated pressure. Ratings for the primary conveyance system range from 6 bars to 28 bars in 2 bar increments, the different ratings being catered for in pipe manufacture by changes in prestressing wire diameter, pitch and number of layers.

During construction, all pipelines are made electrically continuous by the welding of continuity bars across each joint. All joints are cement grouted internally and externally. Special pipes and fittings are generally of fabricated steel construction, and are cement mortar lined to minimize galvanic differences, and thus provide corrosion protection.

Manholes are included on average every 615 meters to provide maintenance access and to carry the necessary air vacuum relief valves and blow-off lines, etc. At every manhole chamber, test leads are installed for use during corrosion survey and for future cathodic protection connection.

The PCCP prestressing wires are protected against corrosion and mechanical damage by a cement mortar coating. In non corrosive soil the pipe was installed un-coated only covered by cement mortar (this called WHITE pipe), while in aggressive ground conditions, black coal tar epoxy barrier coating was applied to the pipe surface to supplement the protection provided by the cement mortar coating (this is called BLACK pipe).

For the corrosion monitoring and the possibility of applying Cathodic Protection (CP) at any stage during the project service life, all pipe joints were provided with continuity bonds, and CP test leads were installed at all appurtenant structures.

The (CP) systems are designed to achieve pipe-to-soil potentials of -710 mV on potential with respect to a Cu/CuSO₄ reference electrode. Magnesium and zinc sacrificial anodes were initially used in Black pipes areas where soil resistivity is very low. They were selected over impressed systems, because of the susceptibility of the prestressing wire to hydrogen embrittlement so it is important to limit the protection levels to avoid hydrogen evolution on the wire surfaces.

The project experienced 4 catastrophic failures during the year 2000, (after 10-years of operation) in the non coated non-CP areas, and from the technical investigation of these four failures, a project policy decision was taken by GMRP-Authority to provide cathodic protection for the entire of the GMR project to cover about 3000 km of large diameter

PCCP.[3]

All failures were located in the White pipe areas characterized by soil of high resistivity where it was virtually impossible to polarize the pipe to the potential of -710 mV by the use of zinc sacrificial anode CP systems. Thus it was decided by the project authority to adopt the 100 mV polarization shift criterion to confirm the adequacy and effectiveness of installed CP systems to prevent any further PCC pipes deterioration due to corrosion of the prestressing wires coated by mortar saturated with high concentration of chloride ions.

Hence the objective of this work is to experimentally evaluate the 100 mV polarization shift criterion for confirming performance and the degree of effectiveness of applied sacrificial anode CP systems of high tensile grade steel wires under tension exposed to corrosive environments of various chloride contents.

Therefore an experimental model was designed and developed to simulate zinc sacrificial anode cathodic protection systems of prestressing steel wires under tension immersed in an alkaline solution with various chloride contents. The 100 mV polarization shift criterion was implemented on all tested samples for the whole period of the experiment. Mechanical properties of tested wires were checked prior and after continuous exposure to prove or disprove the adequacy and effectiveness of the level of protection offered by the applied CP system.[4]

2. Experimental

The experimental setup employed in this work is shown and described in Figure 2, and since it was intended in this work to simulate as close as possible the real physical conditions surrounding the high strength steel wires in concrete pipes, thus it was prudent to place and maintain all relevant wire samples under tension equal to 70% of their U.T.S in PCCP. To achieve this objective 14 tension holding frames were especially designed, fabricated and then tested via strain gauge. Figures 3(a,b) give schematic description of one of these frames.

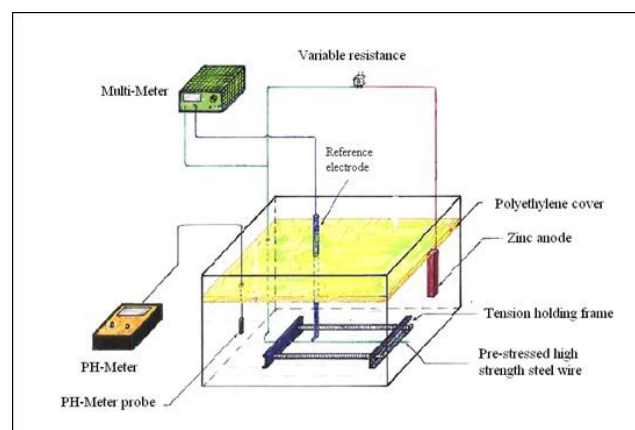


Fig. 2: Detailed schematic view of experimental set-up of a single cell

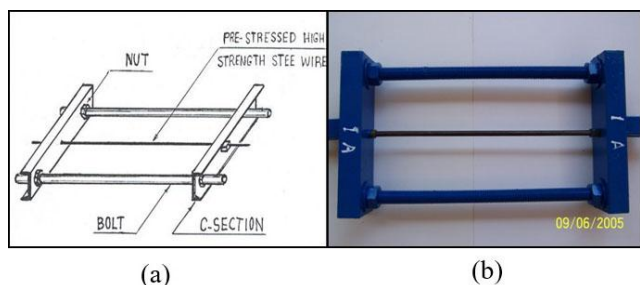


Fig. 3: (a) A Schematic Diagram of An Assembled Tension Holding Frames. (b) A photo of An Assembled Tension Holding Frames.

The fourteen working high strength steel wires samples (6.35 mm in diameter) were supplied from GMRA PCCP manufacturing plant in Brega. Thirteen of them were removed from corroded pipes, and one was cut from a new coil. The metallurgical composition and mechanical properties as certified by the wire manufactures is summarized as follows: Carbon steel (carbon 0.8-0.84%, 0.85-1.00%Mn, 0.030 %Max S, 0.035% Max P, 0.200.35% Si). Typical mechanical properties are presented in Table 1.

Table 1.Typical Mechanical Properties of Prestressing Wires

Tensile Strength	U.T.S (MPa)		Reduction in Area
	Min	Max	
Min(MPa)	1680	1860	Min (%)
1655			30

Each wire sample was subjected to a tensile force of 30 KN and then held in one of the tension holding frames as described earlier before it was released from tensile machine. Periodic testing of each wire sample held in its frame was conducted via a strain gauge to insure that tension is maintained. All samples were coded with identifiable serial numbers S1 to S14 by the use of water proof marker as shown in figure (3b). Each vessel of the 14 used in this work was first washed thoroughly and detergent and then rinsed with portions of distilled water and then were filled with approximately 10 Liters of distilled water. Chunks of cement mortar of the same quality as specified for PCCP manufactured in Brega plant were placed in all vessels to produce a saturated alkaline solution of a pH above 12, simulating as much as possible the real condition of steel prestressing wires embedded in mortar coating of a PCCP. The fourteen working steel wire samples used in this work were prepared as follows:-

1. All samples were first cut in 500 mm segments uniform in shape and in length.
2. Each sample was subjected, by means of a tensile machine, to 30 kN tensile forces to produce a tension equivalent to 55% of U.T.S. Then it was removed from the tensile machine by its designated tension holding frame as explained earlier.
3. A potential measuring post made of copper wire was connected to one end of each working sample and the entire connection zone was covered by coal tar epoxy resin, and electrically insulated by means of tight plastic sleeve.
4. Each working wire sample is passed through the 10 mm

diameter hole and held by two metal clamps equipped with a pvc plate on the inner side of each clamp to provide for electrical insulation of the sample from frame.

5. All samples were numerically coded in the same manner as the tension holding frames described earlier, i.e. S1 to S14.
6. Each tension holding frame with its fastened working wire sample was placed in its designated glass vessel filled with distilled water and concrete mortar chunks.
7. The formation of the electrochemical passive layer on the wire surface of each sample was confirmed through periodic measurements of pH, temperature, and electrostatic natural potential of each working wire sample against a (Ag/AgCl) reference electrode placed in the same vessel for approximately 3 days.
8. The amount of pure sodium chloride salt required to achieve the specified chloride concentration for in each vessel was first weighted, and then dissolved in each vessel. Table 2 gives a summary of the initial wire condition, chloride concentration, and required shift in potential of each sample after CP was applied in each vessel.
9. The electrostatic natural potential of each wire sample was established during the first week through daily measurements of pH, temperature and the potential of each sample until a stable and reproducible measurement of potential is attained i.e. the natural potential of this wire sample in this given prescribed conditions.

Table 2. Summary of Initial Wire Condition, Chloride Conc., and Potential Shift in All Vessels.

Sample No	Wire condition	Vessel No	Chloride concentration ppm	CP criteria mV
S1	corroded	V1	500	100
S2	corroded	V2	750	100
S3	corroded	V3	1000	100
S4	corroded	V4	1250	100
S5	corroded	V5	1500	100
S6	corroded	V6	2000	100
S7	corroded	V7	2500	100
S8	corroded	V8	3000	100
S9	corroded	V9	3000	710
S10	Not corroded	V10	3000	100
S11	corroded	V11	3000	75
S12	corroded	V12	3000	50
S13	corroded	V13	3000	25
S14	corroded	V14	3000	0

10. A zinc sacrificial anode was placed in each vessel and connected in an electrical circuit with a variable resistance to control the amount of current flowing in circuit of the applied cathodic protection such that the measured on potential of each working sample is constantly at a value shifted 100 mV from its pre-determined natural potential. It is worth mentioning here that some trials were carried out ahead of this step by

introducing an interrogator precision switcher in circuit to experimentally confirm that IR drop in such conductive solution is negligible, and hence it was decided that only ON potential will be measured and used to establish the required shift in potential. Figure (2) gives schematic representation of the applied C.P circuit. Table 2 gives a summary of the observed condition of all samples along with measured shifts in potential.

11. A polystyrene cover was placed on the water surface in each vessel in order to minimize the evaporation rate and amount of atmospheric CO₂ gas being dissolved into the water from air.
12. Measurements of pH, temperature, and potential were taken on daily basis with continuous monitoring of all samples to make any necessary adjustments in the variable resistance such that the required shifts in potential are maintained during the duration of the experiment.
13. Periodic Sampling and chemical analysis of water in each vessel was carried out to check for chloride concentration and if any noticeable reduction is observed, a make up amount of sodium chloride salt is added to the solution.
14. Any observed lowering in water level in each vessel due to natural evaporation was periodically corrected by addition of fresh amounts of distilled water.
15. After eight months of continuous daily monitoring of all samples, it was decided to stop and simultaneously withdraw all samples from all vessels. They were first dried, and then cut in 300 mm segments which represent the exposed part of the samples. And after they were visually observed and photographed they were all placed in container with silica-jell to prevent any effect of air humidity before mechanical tests are conducted. 15. Mechanical tests including tensile test and hardness test were performed at Central Research Laboratories in located in Tripoli to quantify any observed changes in mechanical properties incurred on tested samples due to exposure to solutions of variable chloride content and being at the same time under an applied cathodic protection in accordance to the adapted criterion.

3. Results and Discussion

Figures 4 and 5 give graphical representation of the variation of the measured potential of samples S8 (3000 ppm; 100 mV shift), and S13 (3000ppm; 25 mV shift) as a function of time in days, covering the whole period of this study.

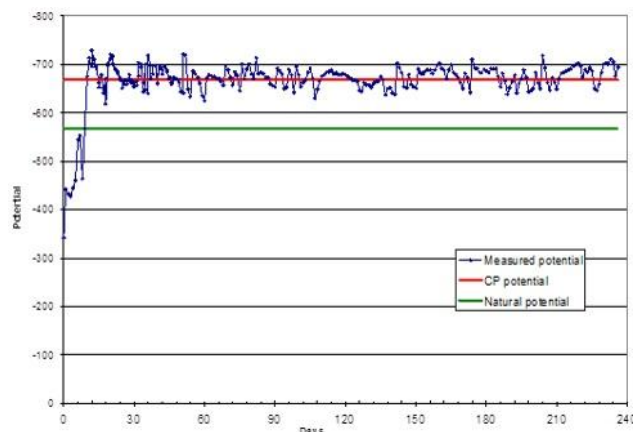


Fig. 4: Potential for Sample (S8).

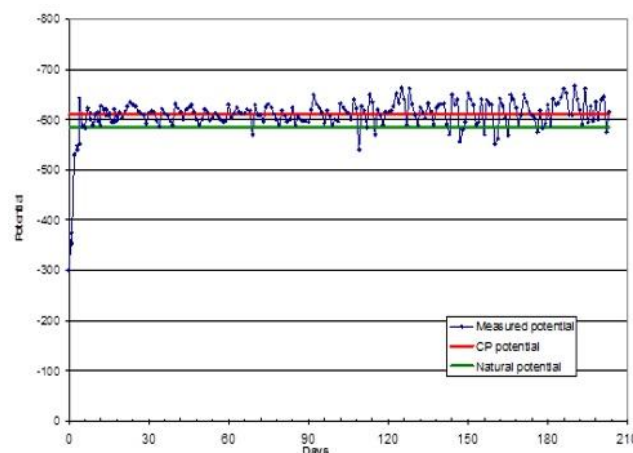


Fig. 5: Potential for Sample (S13)

Table 3 presents a summary of the measured average polarization shift in mV defined as the difference between the overall averages applied CP potential measured in all days, and the established natural potential for each sample. It is noted that the measured average values is slightly above the intended polarization shift of 100, 75, 50, and 25 mV respectively for all samples. This deviation was unavoidable since; polarization and depolarization are dynamic processes constantly changing with many variables controlling in the bulk solution away from the surface of each sample [3]. And thus it was virtually impossible to stabilize potential readings during time interval between two consecutive ones.

Table 3. Summary of Potential Polarization Shift of All Samples.

Sample No.	Natural Potential (mV)	Average Applied CP Potential (mV)	criterion Polarization Shift (mV)	measured Average Polarization Shift (mV)
S1	-558	-667.0	100	109.0
S2	-585	-695.2	100	110.2
S3	-552	-657.5	100	105.5
S4	-580	-687.4	100	107.4
S5	-540	-646.7	100	106.7
S6	-557	-664.8	100	107.8
S7	-572	-679.5	100	107.5
S8	-568	-675.1	100	107.1
S10	-570	-676.9	100	106.9
S11	-540	-623.0	75	83.0
S12	-541	-604.5	50	63.5
S13	-585	-613.4	25	28.4

Figure 6 gives a graphical representation of the average polarization shift measured for all samples in comparison to the intended nominal values.

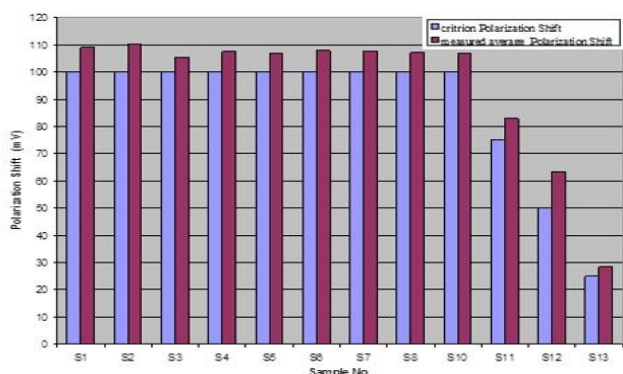


Fig. 6: Summary of Potential Polarization Shift of All Samples.

After each sample was subjected to a tensile test, a force-elongation curve was plotted automatically by computer. Figures 7 to 10 show the force-elongation curves produced for all the samples. All samples show close to normal curves when compared to reference sample S15, indicating that applied cathodic protection was sufficient and effective in arresting the progress of corrosion in the presence of high chloride concentration in the solution. Sample S14 showed the smallest ultimate tensile strength and elongation before failure among all samples. This behavior was expected since no cathodic protection was applied. Thus corrosion process in this sample was progressing in spite of the existing passivating alkaline solution, resulting in the observed deterioration of its mechanical properties. This result confirms that electrochemical passivity will not be sufficient to arrest corrosion in highly chloride contaminated environments in absence of external cathodic protection.

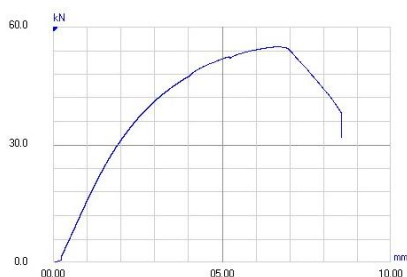


Fig. 7: Load-elongation Curve for S8.

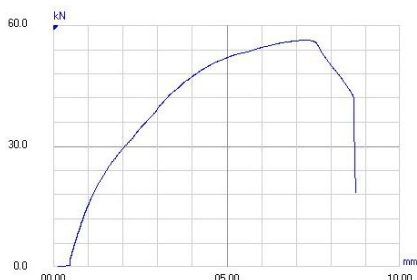


Fig. 8: Load-elongation Curve for S13.

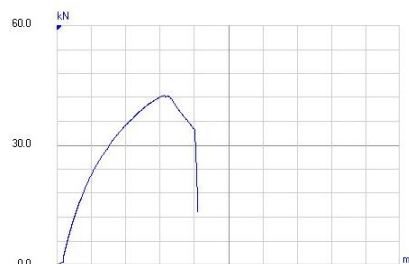


Fig. 9: Load-elongation Curve for S14.

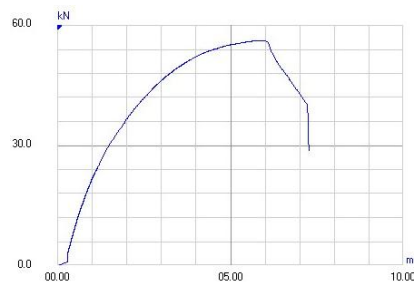


Fig. 10: Load-elongation Curve for S15.

Table 4 shows a summary of all measured mechanical properties for all samples, i.e., ultimate tensile strength (U.T.S), elongation, reduction in area, and hardness.

Table 4. Mechanical Properties of Wire Samples

Sample No.	U. T. S. (MPa)	Elongation (%)	Reduction in area (%)	Hardness HB-30
S1	1781.8	1.439	48.66	389.3
S2	1783.2	1.333	46.38	366.1
S3	1802.4	1.370	46.38	376.1
S4	1783.5	1.418	46.38	358.8
S5	1795.2	1.447	47.52	366.1
S6	1735.4	1.461	48.66	383.2
S7	1779.3	1.307	46.38	379.9
S8	1791.7	1.303	46.38	379.9
S9	1743.9	1.418	45.22	362.4
S10	1778.7	1.408	44.05	377.1
S11	1785.3	1.375	44.05	365.8
S12	1735.5	1.384	47.52	353.0
S13	1786.2	1.498	47.52	386.5
S14	1341.6	0.680	35.50	375.1
S15	1773	1.370	46.38	364.9

Figures 11 to 14 give graphical comparisons between measured mechanical properties of all samples. It can be clearly noted that no significant differences in measured hardness of the cathodically protected samples when compared to those measured for the non protected ones. It is also evident from these graphs that sample (S14), the non protected one gave lower ultimate tensile strength, % elongation, and % reduction area due to the lack of cathodic protection in high chloride concentration environment as mentioned earlier.

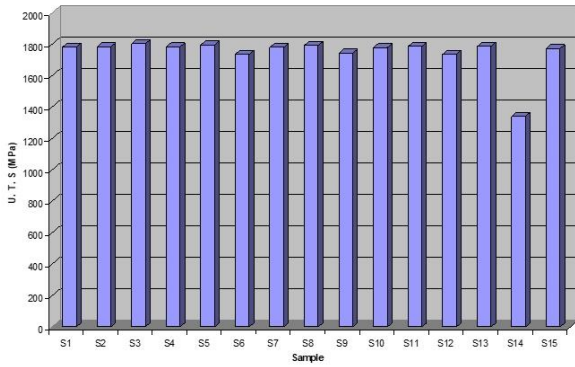


Fig. 11: Effect of Cathodic Protection on Ultimate Tensile Strength.

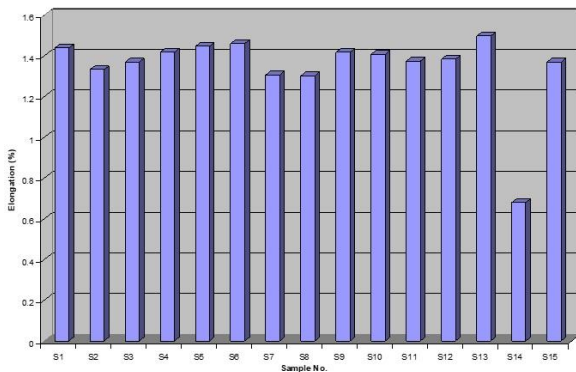


Fig. 12: Effect of Cathodic Protection on Elongation

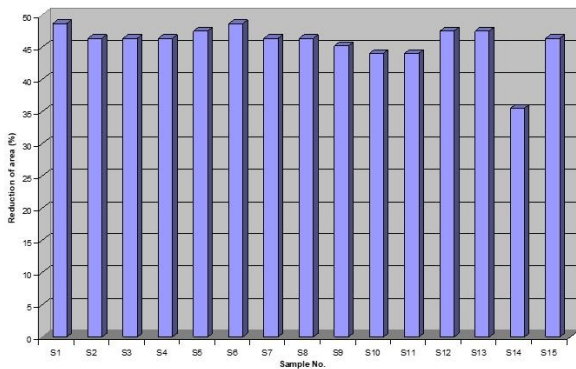


Fig. 13: Effect of Cathodic Protection on Reduction of Area

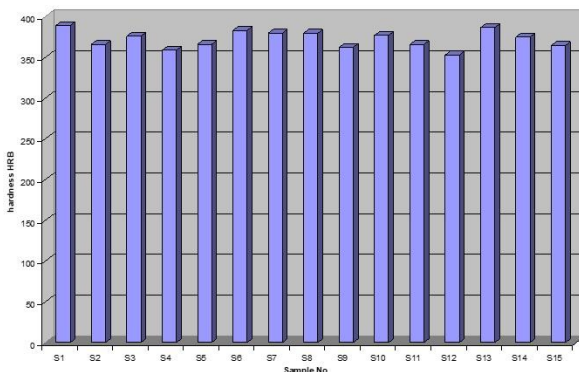
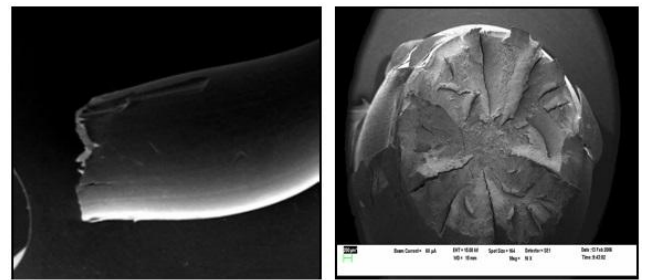


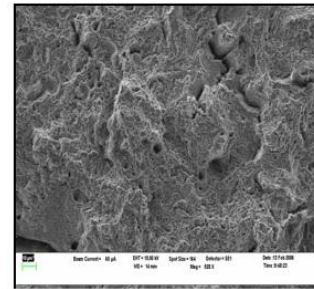
Fig. 14: Effect of Cathodic Protection on Hardness

Figures 15 a, b, and c show the SEM micrographs of the fracture surface of sample S8. The ductile feature and necking are clearly visible in those micrographs. These features indicate that applied cathodic protection was incapable of producing enough hydrogen to cause hydrogen embrittlement

which usually leads to failure mode similar to that observed in stress corrosion cracking.



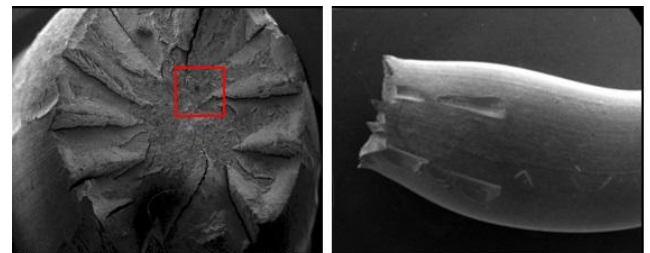
(a) (b)



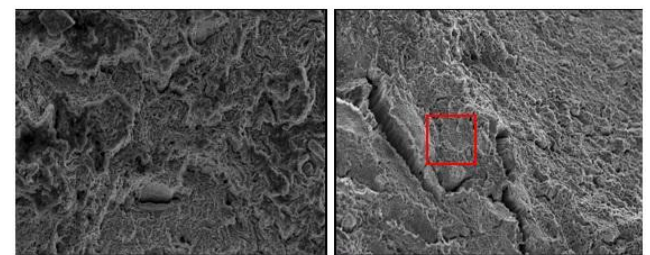
(c)

Fig. 15: SEM Micrograph for Sample (S8).

Figures 16(a), (b), (c), and (d), figure 17 show similar results for samples S13, and S14 respectively confirming the same conclusion stated for sample S8.



(a) (b)



(c) (d)

Fig. 16: SEM Micrograph for Sample (S13).

Table 5 summarizes the results of performance for the applied cathodic protection subjected to different protection criteria. It was found that the application of cathodic protection to partially corroded samples stops the corrosion in all cases studied in this work even in presence of as high chloride concentrations as 3000 ppm. While in the case of sample S14 (non- protected) a severe corrosion is observed resulting in poor mechanical properties

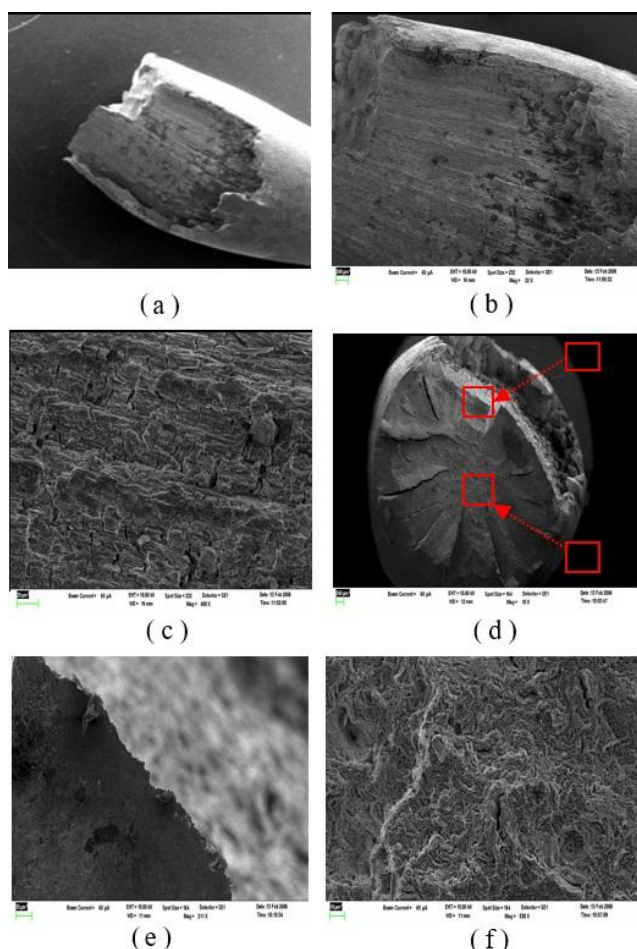


Fig. 17: SEM Micrograph for Sample (S14).

Table 5. Summary of CP results.

Sample No	Chloride concentration ppm	CP levels mv	Status of applied cathodic protection
S1	500	100	Sufficient and effective
S2	750	100	Sufficient and effective
S3	1000	100	Sufficient and effective
S4	1250	100	Sufficient and effective
S5	1500	100	Sufficient and effective
S6	2000	100	Sufficient and effective
S7	2500	100	Sufficient and effective
S8	3000	100	Sufficient and effective
S9	3000	(-710) on potential	Sufficient and effective
S10	3000	100	Sufficient and effective
S11	3000	75	Sufficient and effective
S12	3000	50	Sufficient and effective
S13	3000	25	Sufficient and effective
S14	3000	0	Insufficient and ineffective

4. Conclusion

In this work, the 100 mV polarization shift criterion for the assessment of effectiveness of zinc-sacrificial anodes cathodic protection systems to arrest corrosion in new and partially corroded prestressing steel wires was experimentally evaluated and tested in chloride contaminated aqueous alkaline medium similar to that surrounding environment of prestressing steel wires in PCCP,.

Nine partially corroded and one uncorroded randomly selected samples of steel prestressing wires were immersed in highly rich alkaline aqueous solutions maintained at a pH around of 12 with chloride concentration ranging from 500 up to 3000 ppm. All samples were cathodically protected by a system of sacrificial zinc anodes such that their on-potentials were shifted 100 mV from their natural potentials. Three extra samples were immersed in 3000 ppm chloride solutions and protected under 75, 50, and 25 mV potential shifts in an attempt to establish, a lower limit of the extent of applicability of this criterion under the worst chloride concentration in the surrounding medium.

Experimental results showed that the 100 mV polarization is a valid and more than sufficient criterion to assess the effectiveness of the applied zinc-sacrificial anodes cathodic protection system to arrest corrosion progress in partially corroded and uncorroded prestressing steel wires in alkaline passivating environment contaminated with chloride concentration up to 3000 ppm. The same conclusion was also established even for shifts in polarization as low as 25 mV. This is in full agreement with previous findings by Silvia et. Al. [5].

It was also evident that corrosion of the prestressing wires can not be arrested in 3000 ppm chloride contaminated medium in the absence of cathodic protection. Electrochemical passivity generated on the surface of the wires by immersion in alkaline solution was not sufficient to provide protection against the progress of corrosion.

References

- [1] 1 - H. Elfergani, R. Pullin , K. Holford. Acoustic Emission Analysis of Prestressed Concrete Structures. Journal of Physics: Conference Series 305. 2011, 01207
- [2] 2- S.K.Singh, Corrosion Studies on Prestressing Steel Wire, ph.D. Thesis, Imperial college, University of London, 2000.
- [3] 3-K.M.Enawaa, Technical Evaluation of Field Data from Commissioning of Retrofit Cathodic Protection System for 500Km of 4-meter Diameter Prestressed Concrete Pipeline (PCCP) Utilizing Sacrificial Anodes, MS. Thesis, Imperial college, University of London ,2002.
- [4] 4 -Mars G. Fontana, Corrosion Engineering, McGraw-Hill International Editions, 1987.
- [5] 5 - Sylvia C.Hall, Cathodic Protection Criteria for Concrete Pipe-An Update, MP/November 1998.

Thermal Efficiency Evaluation of Souk Elkhamis Cement Rotary Kiln

Hussam El-Din F. El-Sheikh^a and Suliman A. Shaibi^b

^aAssociate Professor, School of Engineering, Department of Mechanical Engineering, Libyan Academy, Tripoli – Libya.

E-mail: hussam.elsheikh2@mail.dcu.ie

^bM.Sc. student, School of Engineering, Department of Mechanical Engineering, Libyan Academy, Tripoli – Libya.

E-mail: selshibe66@gmail.com

ABSTRACT

نظراً لكون صناعة الإسمنت تعد من الصناعات المستنزفة للطاقة وخصوصاً الحرارية منها، فدراسة أوجه ومجالات استخدام هذا الكم الكبير من الطاقة تعتبر من أهم الأولويات بهذا المجال. حيث تهدف هذه الورقة إلى تسليط الضوء على حيثيات وطرائق استخدام هذه الطاقة وحساب توزيع الطاقة المنتجة من حرق الوقود بالفرن لتحديد مقادير المستفاد والمهدور منها وذلك بإجراء عملية الموازنة الحرارية للفرن. أوجدت هذه الدراسة أن حوالي 47% فقط من الطاقة هو المستغل في إتمام العمليات والتفاعلات الكيميائية، والباقي حوالي 53% يعتبر مفقوداً. أن جزء من هذه الطاقة الحرارية المفقودة يستفاد منه في بعض الأغراض الأخرى اللازمة بهذه الصناعة كعمليات التجفيف والتحميص للمواد الأولية المغذية قبل دخولها للفرن، وتنشيط عملية الحرق للوقود بالفرن، وما إلى ذلك. والجزء الأخر والذي يقدر بحوالي 8.6% يفقد ويهدر عبر سطح الفرن للمحيط. كما وجد أن الطاقة الحرارية الداخلة للفرن لإنتاج كيلوجرام واحد من الكلنكر تعادل 3658.53 كيلو جول\كجم وذلك عند عمل الفرن بحوالي 89% من طاقته الإنتاجية. في وقت أن مقدار الطاقة الحرارية المستخدمة والمسجلة عند الاختبارات الأولية التي أجريت في بداية التشغيل والتي كانت تساوي 3367.64 كيلو جول\كجم وذلك عند عمل الفرن بطاقة إنتاجية تفوق 100%. وهذا يشير إلى زيادة بقرابة 9% من الطاقة. من ذلك توصي هذه الورقة بالبحث في أسباب هذه الزيادة، كما توصي بالتركيز على دراسة إمكانية الاستفادة من هذه الطاقة المهدورة والتي وجدت تساوي 313.27 كيلو جول\كجم وهو ليس بالمقدار البين الذي يمكن إهماله أو تجاهله.

الكلمات المفتاحية: الألياف الزجاجية، المواد المركبة، FRP، GFRP.

Due to the fact that the cement industry is one of the discouraging energy-intensive industries, especially the thermal ones, study areas and aspects of the use of such a large amount of energy is one of the most important priorities in this area. This paper aims to highlight the merits and methods of use of this energy and calculate the output distribution of the energy produced from the burning of fuel to determine the amounts of wasted and used from them by conducting the thermal balance of the process in the kiln. It created that only about 47% of the energy is exploited in the completion of processes and chemical reactions, and the remaining approximately 53% is considered wasted. Part of this thermal energy lost is instrumental in some other purposes necessary in this industry as processes of drying and calcining of raw material nutrients before they entering the kiln, and stimulate the burning process of fuel in the kiln, etc., and the other, which is estimated at about 8.6% lose through the outer surface of the kiln to the surrounding. It was found that the total thermal energy entering the kiln to produce one kilogram of clinker equivalent 3658.53 kJ/kg when the kiln worked in about 89% of its production capacity, at the time that the amount of specific thermal energy used and registered when the initial tests carried out at the beginning of operating, which was equal to 3367.64 kJ/kg when the kiln worked with a capacity above 100%. This refers to the increase of approximately 9% of the energy. This paper recommends research into the causes of this increase of amount of heat consumption. It also recommends focusing on the study of the possibility to recovering this wasted energy, which found equal to 313.27 kJ/kg which is not an insignificant amount that can be neglected or ignored.

Key words: Cement Industry, Rotary Kiln, Thermal Energy, Heat transfer modelling, Energy conservation.

1. Introduction

Cement is one of the world's most important industries for several reasons. First, cement is an essential part of concrete which is the foundational material for any construction industry. Second, because of the importance of cement for assorted construction-related activities such as roads, residential and commercial buildings, tunnels and dams. There are over 150 countries that produce cement and/or clinker [1]. Cement production is an energy-intensive process it consuming about 4 GJ per ton of cement product. Theoretically, to produce one ton of clinker requires a minimum 1.6 GJ of heat [2]. Cement kilns are used for the pyroprocessing stage of manufacture of Portland cement. The kilns are the heart of cement production process, their capacity usually define the capacity of the cement plant. As the main energy consuming and greenhouse gas emitting stage of cement manufacture, improvement of kiln efficiency has been the central concern of cement manufacturing technology [3]. Over the past years, there have been an increasing number of studies performing energy analysis of cement manufacturing processes in order to identify potential opportunities for energy savings. Some of these studies have focused on cement processing kilns which constitute the largest components in any cement production facility.

This modern dry-process Souk Elkhamis cement plant is located about 60 km, south of Tripoli. It is designed to produce 3000 Tons of clinker per day, and one million tons of cement annually, through two similar production lines. This plant has been commissioned in 1978 to "KHD Humboldt wedge industries anlagen AG Company", to produce type 1 Portland cement (general purpose cement), [4]. There are many departments in the factory starting with raw

materials crushers and ending with cement packing. The main components during pyroprocessing process are 4 stage cyclone pre-heater, rotary kiln, and grate type cooler. The kiln is keeping as focus in this study.

2. Mass and Energy Balance

The conservation of mass principle for control volume, C.V expressed as [5];

$$\left(\frac{\text{Total mass entering the C.V during } \Delta t}{\text{during } \Delta t} \right) - \left(\frac{\text{Total mass leaving the C.V during } \Delta t}{\text{during } \Delta t} \right) = \left(\frac{\text{Net change in mass within C.V during } \Delta t}{\text{C.V during } \Delta t} \right)$$

$$m_{in} - m_{out} = \Delta m_{C.V.}$$

During a steady-flow process, the total amount of mass contained within a control volume does not change with time. Then the conservation of mass principle requires that, the rate of mass flow in to the control volume equal to the rate of mass flow out of it.

$$\sum m_{in} = \sum m_{out} \frac{kg}{sec} \dots \dots \dots (1)$$

The energy balance for control volume, C.V., generally expressed as;

$$\text{(Rate of net energy transfer)} = \text{(Rate of change of energy)}$$

$$E_{in} - E_{out} = \frac{dE}{dt} \dots \dots \dots (2)$$

During a steady-flow process, the total energy content of a control volume remains constant, thus the change in the total energy of the control volume is zero. Then the rate form of the general heat energy balance reduces for a steady-flow process to;

$$\sum q_{in} = \sum q_{out} \frac{kJ}{sec} \dots\dots\dots (3)$$

The rate of net heat transfer into or out of the control volume, q when the change in kinetic and potential energies are negligible, and there is no work interaction is, [6];

$$q = m \Delta h = m C_p \Delta T \dots\dots [kJ] \dots\dots\dots (4)$$

While the net heat energy transferred, at specific mass is;

$$\dot{Q} = \dot{m} \Delta h = \dot{m} C_p \Delta T \dots\dots \left[\frac{kJ}{sec} \right] \dots\dots\dots (5)$$

Where, Δh is the change of enthalpy, and, Cp is the specific heat at constant pressure.

The mass and energy balance analysis is used to evaluate the presence of heat energy from a rotary kiln process. Mass and heat balance around the control volume were performed a basis of 1kg clinker.

The data can be obtained from the plant records, while other relevant data for the analysis can be evaluated. The mass balance for the kiln has been described in Figure (1).

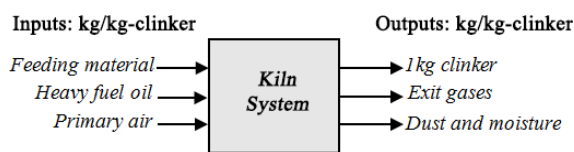


Fig.(1): Mass balance of the kiln overall.

3. Chemical Compositions of Feeding Material and Clinker

The chemical compositions of feeding materials and clinker produced according to criteria required for the installation of the chemical substances included in the cement industry, which insures that the cement product in accordance with the Libyan standard specifications 340/1997, are shown in Table (1).

Table (1): Typical Raw Materials Mix and Clinker Chemical Compositions.

Composition	Raw Material Mix	Clinker
CaO	40 - 43%	62 - 66%
SiO ₂	12 - 14%	19 - 24%
Al ₂ O ₃	3 - 4%	3 - 6.5%
Fe ₂ O ₃	1.5 - 3.0%	2.5 - 4%
MgO	Up to 3%	Up to 4%
SO ₃	Up to 1%	Up to 0.5%
K ₂ O	Up to 2%	-
L.O.J	34 - 37%	-

4. Specifications of Heavy Fuel Oil Used

The heavy fuel oil is predominantly used in cement manufacturing. Souk Elkhamis cement plant is one of these factories, which used this type of fuel to produce the enough amount of heat required. The most important property of fuel oil is the ability to burn in the liquid state. Table (2) shows the typical specifications of heavy fuel oil used (Mazout).

Table (2): Typical Specifications of Heavy Fuel Oil [7,20].

Composition	Parameters	values	Units
	Carbon, C		86.5
Hydrogen, H ₂		12.4	%
Sulphur, S		0.25	%
Nitrogen, N ₂		0.18	%
Oxygen, O ₂		0.05	%
Ash		0.0061	%
Density at 120°C		0.840	kg/l
Specific gravity at 15.6 °C		0.9276	-
Flash point		93	°C
Pour point		72	°C
Gross heat of combustion, Hu		10509.8	%
Temperature at burner		120	°C

5. Models and Assumptions

The main following assumptions are considered for solving the problem:

1. The heat losses from the kiln surface are calculated by considering natural convection as well as thermal radiation.
2. The kiln operates in steady state condition.
3. The kiln is in smooth rotating around it is axis.
4. Compositions of feeding raw material mix and of fuel oil are not change all the time for all subsequent calculations.
5. Feed rate of raw material and fuel are considered as constant.
6. The kiln is simplifying plane surface horizontal cylinder without any existence of deformations and distortions.
7. The heat is transferred in steady state condition.
8. Assume the kiln surface subdivides to recognize the area of each zone.
9. The surface is assumed gray and diffuse in all calculations of this study, (independent of radiation wavelength and direction), so that:

Surface emissivity, $\epsilon_\lambda = \epsilon_\theta = Constant$, [8].

Where; ϵ_λ is spectral emissivity, and ϵ_θ is directional emissivity.

10. The view factor, F12 is for radiation that travels from surface 1 to surface 2. In this study, the surface 2 (air surface) are completely surrounds surface 1 (kiln surface), and the kiln is modeled simply as a cylinder, so that the view factor is always 1, [6].
11. The emissivity is assumed to be a constant value (0.95) throughout the calculations. While the actual kiln surface emissivity is to be measured, the value of (0.95) is believed to be an appropriate estimation based on different references for the surface is assumed dark brown rough oxidized steel plate [9,10].
12. The thermo physical properties of the fluid air are constant.
13. No heat transfer in axial direction.
14. Neglect the effect of the air Humidity.
15. Neglect the wind effect and the fluid around the kiln is moves under the buoyancy force acting.
16. All gas streams are assumed to be ideal gases at the given temperatures.
17. Cold air leakage into the system is negligible.
18. The change of granules size of feeding material and it is motion inside the kiln are neglected.

6. Total Heat Input

The overall heat energy entering the system consists of; heat generated by burning the fuel inside the kiln, and sensible heat in raw meal, fuel, and primary air entering the kiln [12].

The major part of the total amount of heat input is produced by burning the fuel; it is about 97% from the total heat entering the system [9, 19]. The essential parameters required to determine the amount of heat energy produced by burning the fuel are presented in Table (3):

Table (3): Basic Data and Measurements.

Parameters	Values	Unit	Reference
Exhaust gases temperature	1253	K	measured
Preheater temperature	843	K	measured
Kiln discharge temperature	1473	K	measured
Cooler temperature	643	K	measured
Precipitation dust temperature	623	K	measured
Fuel Density at 120°C, ρ	0.840	ton/m ³	Plant data
Fuel Heating value, H_u	10509	kcal / kg _{fuel}	Fuel data
Fuel injected	126.2	m ³ /24h	Plant data
Clinker produced	1337	Ton/day	Plant data
Specific heat of clinker, C_p	0.86	kJ/kg K	[53`55]
Clinker factor	0.6296	kg _{in} /kg _{cl}	Plant data
Air used	1.5 times	-	[11]
Loss of ignition	0.357	%	Plant data

All measurements were taken at one day, when the kiln working with 89% of it is capacity, and all calculations are referring to 1kg clinker.

6.1. Heat Generated by Burning the Fuel

The mass of fuel flow rate, $m_{fuel} = V_{fuel} \times \rho_{fuel} \frac{ton}{day}$

$$m_{fuel} = 126.2 \frac{m^3}{24h} \times 0.84 \frac{ton}{m^3} = 106.01 \frac{ton}{24h}$$

The quantity of fuel required to produce 1kg of clinker is:

$$\dot{m}_{fuel} = \frac{m_{fuel}}{m_{clinker}} = \frac{106.01 \frac{ton}{24h}}{1337 \frac{ton}{24h}} = 0.07929 \frac{kg_{fuel}}{kg_{clinker}}$$

From Eq 5, the specific heat input by Combustion of fuel is:

$$\begin{aligned} \dot{Q}_{fuel} &= \dot{m}_{fuel} \cdot H_{ufuel} \\ \dot{Q}_{fuel} &= 0.07929 \frac{kg_{fuel}}{kg_{clinker}} \times 10509 \frac{kcal}{kg_{fuel}} \\ \dot{Q}_{fuel} &= 833.427 \frac{kcal}{kg_{clinker}} = 3488.73 \frac{kJ}{kg_{clinker}} \end{aligned}$$

6.2. Sensible Heat

The calculations of sensible heat in raw meal of feeding materials, heavy fuel oil used, and primary air entering the kiln are;

The quantity of feeding material is equals to the ratio of rate of raw materials mix feeding to rate of clinker produced as;

$$\dot{m}_{materials} = \frac{24.3056}{15.4745} = 1.57 \frac{kg_{materials}}{kg_{clinker}}$$

The quantity of primary air entering the kiln is $1.81 \frac{kg_{air}}{kg_{clinker}}$.

7. Total Heat Output

Generally the heat living the kiln by five following ways:

1. Waste heat discharge with clinker to cooler.
2. Waste heat with exhaust gases.
3. Heat losses with dust.
4. Heat lost with steam due to humidity.
5. Kiln shell heat losses.

7.1 Waste Heat Discharge with Clinker

The average of specific heat losses with clinker discharge to cooler can be calculated by applying Eq 5,[2]:

$$\begin{aligned} \dot{Q}_{clinker} &= \dot{m}_{clinker} \Delta h = \dot{m}_{clinker} C_{p,clinker} \Delta T \quad \left[\frac{kJ}{sec} \right] \\ \dot{Q}_{clinker} &= 1 \frac{kg_{clinker}}{kg_{clinker}} \times 0.86 \frac{kJ}{kg_{clinker} K} \times (1473 - 643) K \\ \dot{Q}_{clinker} &= 713.8 \frac{kJ}{kg_{clinker} K} \end{aligned}$$

7.2 Waste Heat with Exhaust Gases

There are many gases exhausted from combustion the fuel, primary air, and chemical reactions product which wasted part of heat out of kiln. These gases are; CO₂, H₂O, SO₂, O₂, and N₂.

The combustion of 1 kg of fuel is [2,7]:

$$\begin{aligned} C: 0.86 \times \frac{32}{12} &= 2.29 \text{ kg}_{O_2} \\ H_2: 0.12 \times \frac{16}{2} &= 0.992 \text{ kg}_{O_2} \\ S: 0.25 \times \frac{32}{32} &= 0.25 \text{ kg}_{O_2} \end{aligned}$$

Every 1 kg of fuel combustion required: 2.29 + 0.992 + 0.25 = 3.5 kg_{O₂}

The amount of oxygen required:

$$\dot{m}_{O_2} = 0.0793 \times 3.5 \frac{kg_{O_2}}{kg_{fuel}} = 0.278 \frac{kg_{O_2}}{kg_{clinker}}$$

Total air quantity:

$$\dot{m}_{air} = 0.278 \times \frac{100}{23} \times 1.5 = 1.81 \frac{kg_{air}}{kg_{clinker}}$$

The quantities of waste gases are:

$$\dot{m}_{CO_2} = 0.0793 \frac{kg_{fuel}}{kg_{clinker}} \times 0.86 \frac{kg_{O_2}}{kg_{fuel}} \times \frac{44}{12} = 0.253 \frac{kg_{CO_2}}{kg_{clinker}}$$

$$\dot{m}_{H_2O} = 0.0793 \frac{kg_{fuel}}{kg_{clinker}} \times 0.124 \frac{kg_{H_2O}}{kg_{fuel}} \times \frac{18}{2} = 0.09 \frac{kg_{H_2O}}{kg_{clinker}}$$

$$\dot{m}_{SO_2} = 0.0793 \frac{kg_{fuel}}{kg_{clinker}} \times 0.25 \frac{kg_{SO_2}}{kg_{fuel}} \times \frac{64}{32} = 0.04 \frac{kg_{SO_2}}{kg_{clinker}}$$

$$\dot{m}_{O_2} = 0.0793 \frac{kg_{fuel}}{kg_{clinker}} \times 0.05 \frac{kg_{O_2}}{kg_{fuel}} + \frac{0.278 \frac{kg_{O_2}}{kg_{clinker}}}{1.5} = 0.189 \frac{kg_{O_2}}{kg_{clinker}}$$

$$\dot{m}_{N_2} = 0.0793 \frac{kg_{fuel}}{kg_{clinker}} \times 0.18 \frac{kg_{N_2}}{kg_{fuel}} + \frac{0.931 \frac{kg_{N_2}}{kg_{clinker}}}{1.5} = 0.635 \frac{kg_{N_2}}{kg_{clinker}}$$

The Specific Heat, C_p , for the gases is [3]:

C_p for CO₂ = 1.322 kJ/ kg.K,

C_p for H₂O = 2.596 kJ/ kg.K,

C_p for O₂ = 1.141 kJ/ kg.K,

C_p for N₂ = 1.241 kJ/ kg.K, and

C_p for SO₂ = 3.4689 kJ/ kg.K.

Applying Eq. 5 to find the amount of specific heat wasted with exhaust gases:

$$\begin{aligned} \dot{Q}_{CO_2} &= m_{CO_2} \cdot C_{p,CO_2} \cdot \Delta T \\ \dot{Q}_{CO_2} &= 0.25 \frac{kg_{CO_2}}{kg_{clinker}} \times 1.332 \frac{kJ}{kg_{CO_2} K} \times (1253 - 843) K \\ \dot{Q}_{CO_2} &= 135.5 \frac{kJ}{kg_{clinker}} \\ \dot{Q}_{H_2O} &= 95.79 \frac{kJ}{kg_{clinker}} \\ \dot{Q}_{O_2} &= 88.42 \frac{kJ}{kg_{clinker}} \\ \dot{Q}_{N_2} &= 323.09 \frac{kJ}{kg_{clinker}} \\ \dot{Q}_{SO_2} &= 56.89 \frac{kJ}{kg_{clinker}} \end{aligned}$$

The heat loss with CO₂ from calcium carbonates (CaCO₃) of using materials, when dissolved to calcium oxide (CaO) and carbon dioxide (CO₂), that blows up with gases inside the kiln is determined as follow:

$$\begin{aligned} \dot{m}_{CO_2} &= 0.6296 \frac{kg_{clinker}}{kg_{material}} \times 0.76 \frac{kg_{CaO_3}}{kg_{clinker}} \times 0.44 \frac{kg_{CO_2}}{kg_{CaCO_3}} \times 1.6 \frac{kg_{material}}{kg_{clinker}} \\ \dot{m}_{CO_2} &= 0.3 \frac{kg_{CO_2}}{kg_{clinker}} \end{aligned}$$

Applying Eq. (5):

$$\dot{Q}_{CO_2} = 0.3 \frac{kg_{CO_2}}{kg_{clinker}} \times 1.322 \frac{kJ}{kg_{CO_2}K} \times 410 K = 162.61 \frac{kJ}{kg_{clinker}}$$

The total heat energy wasted with exhaust gases, \dot{Q}_{eg} is;

$$\dot{Q}_{eg} = 135.5 + 95.79 + 56.89 + 88.42 + 323.09 + 162.61$$

$$\dot{Q}_{eg} = 862.3 \frac{kJ}{kg_{clinker}}$$

7.3 Heat Losses with Dust

The quantity of dust exhausted is determined by Exhaust Dusting Fan (E.D. fan). The quantity of air produced by fan is:

$$2.7 \times 10^5 m^3/h.$$

The dust density outlet of kiln is $35 \frac{g}{m^3}$ of air produced by fan [13].

$$\text{The dust flow rate, } \dot{m} = \frac{270000 \frac{m^3}{h} \times 35 \frac{g}{m^3}}{1000 \times 3600} = 2.263 \frac{kg \text{ dust}}{Sec}.$$

$$\dot{m} = \frac{2.263 \frac{kg \text{ dust}}{sec}}{15.4745 \frac{kg_{clinker}}{sec}} = 0.17 \frac{kg_{dust}}{kg_{clinker}}$$

Then applying, Eq 5;

$$\dot{Q}_{dust} = 0.17 \frac{kg_{dust}}{kg_{clinker}} \times 1.09 \frac{kJ}{kg_{dust}K} \times 330 K = 61.15 \frac{kJ}{kg_{clinker}}$$

7.4 Heat Lost with Water Vapor, H₂O

7.4.1 Water Vapor from Raw Material

The contamination of humidity in raw material [4]:

$$\dot{m}_{H_2O} = \left(0.04 \frac{kg_{H_2O}}{kg_{Ls}} \times 0.124 \frac{kg_{Ls}}{kg_{material}} \right) +$$

$$\left(0.575 \frac{kg_{H_2O}}{kg_{clay}} \times 0.24 \frac{kg_{clay}}{kg_{material}} \right) +$$

$$\left(0.85 \frac{kg_{H_2O}}{kg_{iron \ ore}} \times 0.1 \frac{kg_{iron \ ore}}{kg_{material}} \right) =$$

$$\dot{m}_{H_2O} = 0.253 \frac{kg_{H_2O}}{kg_{material}}$$

About 2/3 of this value is evaporated in pre-heater cyclones, then [13];

$$\dot{m}_{H_2O} = 0.253 \frac{kg_{H_2O}}{kg_{material}} \times 0.34 \times 1.57 \frac{kg_{material}}{kg_{clinker}} =$$

$$0.14 \frac{kg_{H_2O}}{kg_{clinker}}$$

By applying, Eq 5;

$$\dot{Q}_{H_2O} = 0.14 \frac{kg_{H_2O}}{kg_{clinker}} \times 2.474 \frac{kJ}{kg_{H_2O}K} \times 325 K =$$

$$112.57 \frac{kJ}{kg_{clinker}}$$

7.4.2 Water Vapor from Waste Gas

$$\dot{m}_{H_2O} = 1.81 \frac{kg_{air}}{kg_{clinker}} \times 0.34 \times 0.1 \frac{kg_{H_2O}}{kg_{air}} = 0.181 \frac{kg_{H_2O}}{kg_{clinker}}$$

By applying, Eq 5;

$$\dot{Q}_{H_2O} = 0.181 \frac{kg_{H_2O}}{kg_{clinker}} \times 2.474 \frac{kJ}{kg_{H_2O}K} \times 325 K =$$

$$145.53 \frac{kJ}{kg_{clinker}}$$

7.5 Kiln Shell Heat Losses

The part of heat which produced by burning the fuel will be transferred to the kiln outer surface by radiation, convection, and conduction despite to the thermal resistance insulators lining, (refractory bricks). This heat is transferred (wasted) to the surrounding due to temperature differential (driving force).

The heat losses from the kiln surface are calculated by considering natural convection as well as thermal radiation.

7.5.1 Natural Convection

The kiln is assumed horizontal cylinder, so an empirical equations of a heated horizontal cylinder are used to calculate the natural convection heat transfer.

The heat transfer due to thermally induced natural convection at solid surface immersed in a fluid, in general can be correlated with the non-dimensional Grashof number, *Gr*. It represents the ratio of the buoyancy force to the viscous force acting on the fluid and expressed as [6]:

$$Gr_d = \frac{g \beta \Delta T d^3}{\nu^2} \dots \dots \dots (6)$$

Where:

g is the gravitational acceleration, m/s².

ν is the kinematic viscosity of the fluid, m²/s.

ΔT is the temperature difference between the surface (*T_s*) and ambient temperature (*T₀*), K.

d is the diameter of the kiln outer surface (the characteristic length of geometry, *L_c*), m.

The volumetric expansion coefficient, β used as ideal gases in this study, so [29];

$$\beta = \frac{1}{T_f} \left[\frac{1}{K} \right] \dots \dots \dots (7)$$

Where; *T_f* is the film temperature, and defined by:

$$T_f = \frac{T_s - T_0}{2} \text{ by absolute temperature } K \dots \dots (8)$$

The heat transfer coefficient, *h* plays a major role in convection heat transfer. It is scaled to a non-dimensional number, Nusselt number, *Nu*:

$$Nu_d = \frac{h_d}{K} \dots \dots \dots (9)$$

Where, *K* is the fluid heat conductivity.

The relationship between Nusselt number and Grashof number can be coined as:

$$Nu_d = c (Gr Pr)^n \dots \dots \dots (10)$$

Where,

Pr is the non-dimensional Prandtl number,

C and *n* are the constants; the value of these constants essentially depends on the geometry of the surface and the flow regime which is characterized by the range of the Grashof number, [14].

When, *Gr* = 10⁴ - 10⁷ the flow is laminar, and Eq (10) becomes:

$$Nu_d = 0.48 (Gr Pr)^{0.25} \dots \dots \dots (11)$$

When, *Gr* = 10⁷ - 10¹² the flow is turbulent, and, Eq (10) becomes:

$$Nu_d = 0.125 (Gr Pr)^{0.333} \dots \dots \dots (12)$$

When the Nusselt number is known, the heat transfer coefficient can be obtained by equation:

$$h = \frac{Nu_d K}{d} \left[\frac{W}{m^2 K} \right] \dots \dots \dots (13)$$

The natural convection heat transfer rate can be obtained by Newton's law of cooling:

$$q_{conv} = A_s h (T_s - T_0) [W] \dots \dots \dots (14)$$

Where; *A_s* is the area of heat transfer surface, (kiln surface).

7.5.2 Thermal Radiation

The heat flow by thermal radiation from gray and diffuse surface with a temperature of *T_s* for any zone at the four times on day, to the ambient with a temperature of *T₀* at these times is given by [14]:

$$q_{rad.(S \rightarrow 0)} = \sigma \epsilon_s A_s F_{S \rightarrow 0} (T_s^4 - T_0^4) [W] \dots \dots \dots (15)$$

Where;

σ is the Stefan-Boltzmann $\left(5.67 \times 10^{-8} \frac{W}{m^2 K^4} \right)$.

ϵ_s is the kiln surface emissivity = Constant.

$F_{S \rightarrow \theta}$ is the view factor, for radiation that travels from kiln surface to the air surface = 1.

Note: all the temperatures in this equation are in Kelvin.

For more accurate results in the estimation of heat losses through the kiln outer surface, the kiln surface is divided into four zones, according to the types of refractory bricks used, and chemical reactions that occur inside the kiln, as well as reading of surface temperature measurements. Where taking the average temperatures of each zone as follows in Table (4).

Table (4): Averages of the surface temperature, T_s , measurements for every zone at four times on day with the ambient temperature, T_o , in related times.

		Temperature [°C]				
		$T_s \cdot Z_1$	$T_s \cdot Z_2$	$T_s \cdot Z_3$	$T_s \cdot Z_4$	T_o
Time	1	171	266	299	245	9
	2	167	271	310	246	5
	3	175	280	316	252	17
	4	193	291	302	263	11

Then calculate the heat losses through the kiln surface by applying the above previous equations, (6 – 15). The results of these calculations are shown in Table (5).

Table (4): Results of shell heat loss calculations.

		Time				
		1	2	3	4	Average
q at zones [kW]	Z ₁	832.42	816.94	832.38	1012.93	873.67
	Z ₂	704.64	736.87	761.90	832.43	758.96
	Z ₃	2203.34	2383.57	2419.23	2237.49	2310.91
	Z ₄	862.20	878.53	878.02	997.81	904.14
	Total	4602.60	4815.91	4891.53	5080.65	4847.67

7.6 Theoretical Heat Required Producing 1 kg of Clinker

The theoretical heat required in relevant process is assigned according to the following calculations [15,12], while theClinker Chemical Compositions is taken partially from Table (1), andpartially from plant data.

$$\dot{Q}_{Tr} = 4.11 \times H_{Al} + 6.48 \times H_{Mg} + 7.646 \times H_{Ca} - 5.116 \times H_{Si} - 0.59 \times H_{Fe}$$

$$\dot{Q}_{Tr} = 4.11 \times 5.7 + 6.48 \times 2.1 + 7.646 \times 64.9 - 5.116 \times 23.3 - 0.59 \times 3.6$$

$$\dot{Q}_{Tr} = \frac{411.9336kcal}{kg_{clinker}} = 1724.35 \frac{kJ}{kg_{clinker}}$$

8. Kiln Thermal Efficiency

To determine the thermal efficiency of the Souk Elkhamis cement kiln thermodynamically, obtaining that the kiln is the system, [5];

$$\text{Kiln efficiency, } \eta_{th} = \frac{\text{Net Work Output}}{\text{Total Heat Input}} = \frac{W_{net}}{\sum \dot{Q}_{in}}$$

Since, $W_{net} = \sum \dot{Q}_{in} - \sum \dot{Q}_{out}$
 Then, Kiln efficiency, $\eta_{th} = \frac{\sum \dot{Q}_{in} - \sum \dot{Q}_{out}}{\sum \dot{Q}_{in}} \dots \dots \dots$ (16)

Where;
 $\sum \dot{Q}_{in}$ is the overall of heat energy entering the system, and
 $\sum \dot{Q}_{out}$ is the overall of heat energy living the system.

Accordingly, the thermal efficiency of the kiln is equal to:

$$\therefore \eta_{th} = \frac{3658.53 - 1932.97}{3658.53} = 0.471 \approx 47\%$$

9. Percentage of SHL to the Total Heat Input

The percentage of heat losses through kiln outer surface by convection and radiation at any day from the total heat input at this day is presented by;

$$\text{Percentage of SHL} = \frac{\dot{Q}_{SHL}}{\dot{Q}_{in}} \times 100$$

10. Evaluation of Mass and Energy Balance

The complete mass and energy balance for the system which calculated are presented in Table (6, A and B).

Table (6A): The Input Mass and Energy Balance.

Stream	Heat Flow Kg/kg _{ci}	Specific Heat Cp KJ/kg °C	Temperature °C	Heat Energy kJ/kg _{ci}	%
Combustion of Fuel	-	-	-	3488.73	95.4
Sensible Heat of Fuel Oil	0.079	1.172 [16]	120	11.15	0.3
Feeding Material	1.57	0.9 [12,17]	80	113.04	3.1
Primary Air	1.81	1.008 [17,18]	25	45.61	1.2
Total	3.46	-	-	3658.53	100

Table (6B): The Output Mass and Energy Balance.

Stream	Heat Flow Kg/kg _{ci}	Specific Heat Cp KJ/kg °C	Temperature °C	Heat Energy kJ/kg _{ci}	%
Clinker Discharge	1.0	0.86 [15,18]	545	468.70	12.81
Exhaust Gas	1.965	*	325	831.75	22.73
Exit Dust	0.17	1.09 [12]	330	61.15	1.67
Water Vapor	0.321	2.474 [11]	325	258.10	7.05
Shell Heat Loss	-	-	-	313.27	8.56
Reaction Energy	-	-	-	1724.35	47.13
Uncounted	-	-	-	1.21	0.03
Total	3.46	-	-	3658.53	100

* The average specific Heat, C_p , for the gases is $CO_2 = 1.294 \text{ kJ/kg K}$, $H_2O = 2.474 \text{ kJ/kg K}$, $O_2 = 1.122 \text{ kJ/kg K}$, $N_2 = 1.215 \text{ kJ/kg K}$, and for $SO_2 = 2.109 \text{ kJ/kg K}$, [11].

11. Conclusion

This study shows that about 47% of the energy is exploited in the completion of processes and chemical reactions, and the remaining approximately 53% is considered wasted. Part of this thermal energy lost is instrumental in some other purposes necessary in this industry as processes of drying and calcining of raw material nutrients before they entering the kiln, and stimulate the burning process of fuel in the kiln, etc., and the other, which is estimated at about 8.6% lose through the outer surface of the kiln to the surrounding. It was found that the total thermal energy entering the kiln to produce one kilogram of clinker equivalent 3658.53 kJ/kg when the kiln worked in about 89% of its production capacity, at the time that the amount of specific thermal energy used and registered when the initial tests carried out at the beginning of operating, which was equal to 3367.64 kJ/kg when the kiln worked with a capacity above 100%. This refers to the increase of approximately 9% of the energy.

REFERENCE

- [1] Anne Elizabeth, Oberlink, “*Non-portland Cement Activation of Blast Furnace Slag*”, University of Kentucky Master’s Theses. Paper 25, (2010).
- [2] Engin T., Ari V., “*Energy Auditing and Recovery for Dry Type Cement Rotary Kiln System- A Case Study*”, Energy Conservation and Management, 46, pp. 551-562, (2004)
- [3] Prajna Mohanty, Smruti Snigdha Patro, “*Processing and Characterization of PEEK with CKP Particles: Use of Industrial Waste in Composite Making*”, International Advanced Research Journal in Science, Engineering and Technology, ISSN 2394-1588, Vol. 2, Issue May (2015).
- [4] KHD Industrieanlagen AG; “*Specifications Documents of Souk Elkhams Cement Plant*”; (1978).
- [5] Y. A. Çengel, and M. A. Boles, “*Thermodynamics: An Engineering Approach*”, Fifth Edition, McGraw-Hill, (2006).
- [6] Çengel .Y.A, “*Heat Transfer*”, Second Edition, McGRAW-Hill, USA, (2003).
- [7] Khalifa M. G, Zohir A. E.and Wanis M. M. “*Study of the Main Energetic Parameters in the Rotary Kiln*”, proceeding of first scientific environmental conference, Zagazig Univ., pp. 171-194, (2006).
- [8] Yunus A. Cengel, Afshin J. Ghajar, “*Heat and Mass Transfer: Fundamentals and Applications*”; 4th Edition; Chapter 12 “Fundamentals of Thermal Radiation”, (2011).
- [9] Hideyuki Tanaka, “*Cement Process and Energy Saving*”, Technical Expert International Engineering Dept. The Energy Conservation Center, Japan, November, (2006).
- [10] European Rotary Kiln Services Ltd; Barry Cooke, David Hey; “*Kiln Alignment Analysis for Souk Elkhams Cement Plant*”; May (2009).
- [11] Boateng, Akwasi, “*Rotary kilns: transport phenomena and transport processes*”, Amsterdam; Boston: ElsevierButterworth-Heinemann, ISBN 978-0-7506-7877-3, (2008).
- [12] R. K. Patil, M. P.Khond, L. G. Navale, “*Thermal Energy Assessment of Indian Cement Plant Specially Related to Rotary Kiln*”, IOSR Journal of Mechanical and Civil Engineering (IOSR-JMCE) ISSN(e) : 2278-1684, ISSN(p): 2320-334X, pp 23-31
- [13] KHD, Humboldt Wedag, “*Pre-heater Manual Sheets*”, Plant Hand Book.
- [14] William S. Janna, “*Engineering Heat Transfer*”; 2nd Edition, ISBN 0-8493-2126-3, (2000).
- [15] Kurt E. Peray, “*Cement Manufacturer’s Handbook*”, Chemical Publishing Co., Inc. ISBN 0-8206-0368-6, New York, N.Y. (1979).
- [16] Energy Efficiency Guide for Industry in Asia, “*Fuels and Combustion*”, UNEP United Nations Environment Programmer, (2006).
- [17] Shaleen Khurana, Rangan Banerjee, Uday Gaitonde, “*Energy Balance and Cogeneration for A Cement Plant*”, Applied Thermal Engineering. No., 22, PP. 485-494. (2002).
- [18] Holder Bank Cement Seminar, “*Heat Balances of Kilns and Coolers and Related Topics*”, Energy Balance of Kiln; Switzerland, March, (1991).
- [19] Ibrahim, A. Ibrahim, and I. Garba, “*Modeling of Sokoto Cement Production Process Using Afinite Automata Scheme*”, An Analysis of the Detailed Model, ISSN 2250-3005, Vol. 04, Issue: May (2014).
- [20] “*Certificate of Quality Fuel Oil*”, issued by Azzawiya refinery in, (2012), No, F- 2/2012.

Using Hazard-Based Duration Models to investigate the Impacts of RUC on Libyan Drivers Travel Patterns

Aziza Safour

Architecture and Urban Planning Department, University of Benghazi, Libya

Tel.: +92 556 8655; e-mail: aziza.safour@uob.edu.ly

ABSTRACT

This paper studies the perceived impacts of road user charging (RUC) on drivers daily activity travel patterns in urban areas by using one of the large Libyan cities (Benghazi) as the case study. The analysis uses full parametric hazard models and data from a field-based RUC experiment that was conducted in Benghazi. The database consists of activity-based travel durations. This paper focuses on the analysis of the durations of drivers travel-to-work trips and addresses the changes on the patterns of driver's trips over the study period to investigate the differences attributable to origin (home-based), time, gender and age as a result of the RUC impacts. The results indicate that RUC can have a positive impact in reducing traffic congestion with reduction of driver's trips crossing restricted areas during peak period by around 35.5%. The paper concludes that RUC could serve as a good instrument in reducing traffic congestion and in improving the environment in city centre of Benghazi. The results could be of benefit to transport policy makers.

Keywords: Activity-based travel patterns, Road user charging and hazard-based duration models.

1. Introduction

Road-user charging (RUC) can be defined as a method of collecting money from road users. Whittles, (2003) defined road pricing as an asset of ideas that can be applied in urban areas to charge road users particularly when they drive in urban areas. RUC is considered as a practical technique used to solve or reduce traffic congestion and transport problems.

To create charging policy that is effective against congestion, some trips would have to be cancelled, while others would have to adapt their mode of travel, destination, frequency or time of travel. This would mean a change both in the lifestyle and style of travelling of an individual or the whole household, and the change involves rescheduling activity patterns, in terms of where, when, how, and with whom these activities are scheduled during the day or week, in order to achieve their desired activity participation (Bowman and Ben-Akiva, 2001).

Many studies have used an activity-based approach to analyse the impact of road user charging on activity travel patterns using travel and activity data. Moreover, various field-based charging experimental studies have been done by investigating the user's behavioral response toward the hypothetical introducing of road user charging policy.

For instance, Hug et al.,(1997), Thorpe & Hill (2003), Francsics (1998), O'Mahony et al., (2000), Nielsen (2004) and Chow (2006) are the most studies that examined behavioral responses toward RUC and provided detailed information on how users could adopt their travel patterns over time in response to RUC. The common positive aspect of these field experimental studies is the use of real budget to achieve more realistic decision from the participants. This process of using real budget helps the researcher to enhance the validity of the experiment. Other worthy points are the use of peak period toll hours which are the effectiveness time that can be used for charging, point-based or cordon-based charging as the type of charging, multi-days data by recording activity travel data for two periods before and after introducing of road user charging.

In this study the approach pursues the examples that stated above by using a field-based RUC experiment, pre-paid experiment budget, cordon-based charging, morning peak period toll hours and multiple activity travel data (7days before and 7days after the introducing of RUC) to ascertain and document the perceived impacts of RUC on individuals activity travel patterns in Libya cities for a sample of 120 participants for the real experiment and 60 participants of another

sample that uses as a control group.

2. Hazard-Based Duration Models

Hensher and Mannering (1994) were one of the early advocates of applying hazard models to travel demand and activity duration modelling. Bhat (1996) stated that hazard duration models are regarded as a useful tool that can be applied to activities and there is much evidence to suggest that the hazard theory is an appropriate tool for investigating parameters that influence changes in both activity type and the consequential demand for travel. Zhong and Hunt (2005) examined household weekend activity durations using hazard-based models. This work suggested that a fully parametric hazard model can be considered as a suitable model for activity and travel related modelling. Also, Zhong et al. (2005) showed that the four most widely used distributions of a fully parametric hazard are Weibull, Exponential, lognormal and log logistic.

Moreover, the hazard function can be used as a tool to compare different scenarios so that their differences can be highlighted. In this study, the analysis focuses on the comparison of the hazard function of travel-to-work trips collected as part of the field based RUC experiment. The analysis will seek to develop a deeper understanding of the changes that have taken place in the duration of the travel-to-work trips of the field-based experiment that conducted during two weeks in May, 2008 in Benghazi, Libya.

The next section of the paper provides a brief description of the data used in the analysis then explores which of 11 parametric models best fits the data used in this work and then presents the results. The analysis firstly looks at the entire data set collected over the study period to explore differences due to trip origin, gender and mode choice. Lastly conclusions are drawn.

3. Description of the Travel Data

Naturally, as stated above, the data used in this study were gathered by the researcher using field-based road user charging experiment in May, 2008 in Benghazi, Libya. In total, 81 driver's respondents completed the survey during the two weeks period; the sample size of the control group respondents was 36. The database consists of information regarding travel-related activities (activity travel diary) and individual and household information. The travel related activity data includes a range of trip information including origin, destination, mode of travel, journey purpose and start and end time for two weeks. Figure 1 explain the main features of RUC experiment that conducted in Benghazi, including the location of the

cordons, type of charging scheme, restricted hours, enforcement system, toll level, type of data and type of sample.

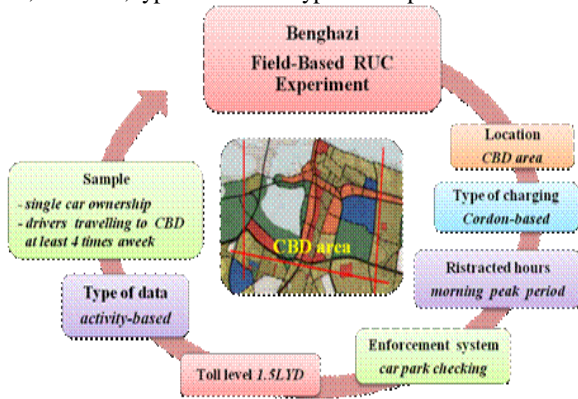


Fig. 1: The key features of road user charging experiment

4. Preliminary Findings of Road User Charging Impacts on Activity Travel Patterns

According to the field based RUC survey, the preliminary results show that;

- Around 68% (55 drivers) of the 81 drivers chose to pay the toll. A number of 46 drivers of the 81 (57%) chose to pay the charging toll on all the days of the experiment, however, 9 drivers of 81 (11%) chose to pay the toll for 3-4 days of the week. On the other hand, 26 drivers of 81 (32%) did not pay the toll at all and avoided the payment by choosing another alternative.
- During the first week of the study survey, drivers made a total of 2023 trips (or 25 trips per person per week, 3.5 per person daily, these results are mostly different with the previous results of Doxiadis (1989) that have been stated that it is about 1.8 trips per person daily.
- However, in the second week, the number of trips decreased by 3.3%. In the first week, the majority (97 %) of trips were by cars and only (3 %) of trips by other modes of travel. From these, one can see that the car was used as the main mode of travel for all the trips types.
- The daily travel patterns is classified into six trips types with respect to the “work” and “home” location namely; home-based, work-based, shopping- based, recreation-based, visiting-based and others-based that involve other different activities places. Based, recreation-based, visiting-based and others-based that involve other different activities places .
- Figure 2 shows that in the first week, the half (50%) of driver’s trips were home-based trips, while nearly one-third (30%) were work-based trips, around 7% were shopping place-based trips, 5% visiting places-based trips and 3% recreation-based trips.

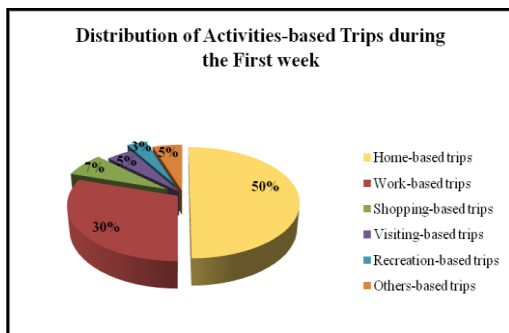


Fig. 2: Distribution of activity-based trips during the first week.

- In the first week the drivers made a total of 1006 home-based trips. Of these, 63% were home-based work trips while nearly one-third were home-based non-work trips such as home-based shopping trips 12%, home-based visiting trips 8%, home-based recreation trips 7% and home-based others trips 10%.
- Number of activity-based trips, and home-based work trips represent nearly two-third of all home-based trips. These results are generally different with the previous results of Libyan studies that have been stated that around 49% of trips are home-based travel to work trips (Doxiadis, 1989).
- Figure 3 illustrates the changes that have accrued on home-based activity travel trips during the second week. Furthermore, even though the percentage of home-based travel to work trips has slightly increased during the second week the number of travel to work trips has slightly decreased by 2.2%. Home-based shopping trips have decreased by 14.5 %, home-based recreation trips have decreased by 13%, and on the other hand, home-based visiting trips have increased by 13 %.

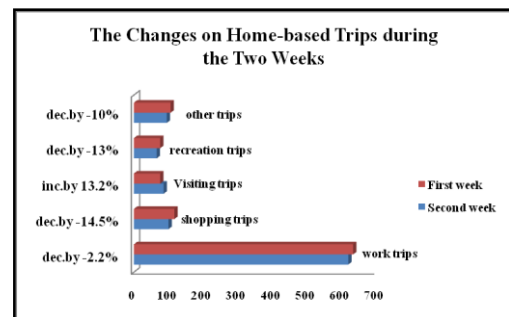


Fig.3: The changes on home-based trips during the two weeks

5. Using Hazard-Based Duration Models to Explain Changes in the Duration of Activity Travel during the Field Experiment

As mentioned previously, survival models or hazard-based duration models are common terms for the collection of models that characterise a probability distribution of the positive random variable T. A review of the literature indicates that while Hensher and Mannering (1994) started to present hazard-based duration models to travel demand modeling in a general way and gave an overview of the applications of these models to transport problems, a number of researchers tried to describe and analyse activity-based duration using hazard-based duration models. Safour (2012) explained the steps in the hazard model approach that applied in this section by clarifying the hazard theory and hazard functions also the steps in the application of the hazard theory.

5.1 Exploring the shape of the probability density function for durations of travel to work trips in the first week

According to Pas (1996), MOTOS Handbook (2008), and Statsoft (2008), there are three families of hazard duration model that can be applied to trip activity; fully parametric, semi-parametric and non-parametric. According to MOTOS Handbook (2008), and Statsoft (2008) the factor that determine the applicable method of hazard is the size of the sample of data, for instance, if the sample is large enough (e.i., 100 and more) the three families of hazard can be used. However, if the sample is small, then these three families can be applied if the data has normal distribution, otherwise, fully parametric hazard model is the suitable method to applied for a small number of

observations.

In this study, full ranges of parametric functions were considered in the analysis of individuals daily travel durations in Benghazi during the first week of the field experiment. Examples of parametric models include Exponential, 2-parameter Weibull, Weibull, 3-parameter Weibull, Normal, Lognormal, 3-parameter Lognormal, Logistic, Loglogistic, 3-parameter Loglogistic and Smallest Extreme Value. According to Hensher and Button (2000) and Zhong et al., (2005), the four largely used distributions in activity-based modelling are Weibull, Exponential, Lognormal and Loglogistic. Generally, the best fit model of these 11 models are identified based on various tests such as, the likelihood test, Anderson-Darling test and the Correlation Coefficients test (Hensher and Button, 2000). In this study, the Anderson-Darling (AD) test and the Correlation Coefficients (COR) test have chosen to evaluate the fit model. Zhong et al., (2005) mentioned a low value of the AD test and a COR value closest to 1 identify the best-fit model. As illustrated in Table 1, a 3-parameter lognormal distribution has the lowest value of the AD test and the highest value of the COR test for travel work trips, followed by the Lognormal distribution. However, the 3-parameter Lognormal has a negative threshold, which has no meaning in the context of duration of travel. Therefore, the lognormal option is selected here as the best fit model.

Table 1: Goodness-of-fit tests for duration of travel to work for the first week

Distribution	Test Statistic	
	AD	COR
Weibull	56.877	0.897
3-parameter Weibull	24.868	0.914
Exponential	183.45	-
2-parameter Exponential	117.95	-
Normal	33.140	0.907
Lognormal	24.001	0.949
3-parameter lognormal*	23.775	0.949
Logistic	27.994	0.947
Loglogistic	83.873	0.811
3-parameter loglogistic *	26.58	0.947
Smallest extreme value	83.873	0.811
Best-fit model	lognormal	

* These distributions generate negative thresholds.

According to the above explanation, the next step was to check that the best fit model for the data for each week separately. The six most promising parametric distributions have been considered and the results presented in Table 2. All of these distributions have positive parameters with the threshold equal to zero. By comparing AD and COR values in Table 2, it is clear that the Lognormal distribution (statistically) is the best-suited distribution for the data, with the Loglogistic function having a similar performance. These two distributions were cited in the four (Weibull, Exponential, Lognormal and Log logistic) highlighted by Zhong (2005) and consistent with the Weibull distribution considered by Oh and Polak (2002). On the basis of this evidence the Lognormal distribution was adopted as the basis for this study.

Table 2: Goodness-of-fit tests for duration of travel to work for the data of two weeks

Distribution	Test Statistic Value			
	Week 1		Week 2	
	AD	COR	AD	COR
Weibull	56.877	0.897	19.637	0.934
Exponential	183.45	-	103.77	-
Normal	33.140	0.907	14.870	0.948
Lognormal	24.001	0.949	12.006	0.954
Logistic	27.994	0.947	18.317	0.939
Loglogistic	83.873	0.811	15.581	0.947
Best-fit model	Lognormal			

By normalizing the data it is possible to compare the disaggregated datasets and thus begin to understand the changes in travel work trip durations that have taken place over time and depending on other parameters such as time of travel, mode choice, and gender.

According to the Handbook (2008), and Statsoft (2008), the Lognormal probability density function $f(t)$ is given by:

$$f(t) = \frac{1}{\sigma t \sqrt{2\pi}} \exp \left[-\frac{(\ln t - \mu)^2}{2\sigma^2} \right], t > 0 \quad (1)$$

The cumulative distribution function $F(t)$:

$$F(t) = \int_{-\infty}^t \frac{1}{\sigma t \sqrt{2\pi}} \exp \left[-\frac{(\ln t - \mu)^2}{2\sigma^2} \right] dt \quad (2)$$

The survival function is $S(t)$

$$S(t) = \int_{-\infty}^t \frac{1}{\sigma t \sqrt{2\pi}} \exp \left[-\frac{(\ln t - \mu)^2}{2\sigma^2} \right] dt \quad (3)$$

Where: μ = the location parameter ($\mu > 0$), and σ = the scale parameter of the distribution ($\sigma > 0$).

Using the Lognormal density function the hazard theory is applied to total sample sets to develop the baseline results, which are presented in the next section.

6. Baseline Hazard for Travel to Work Trips Durations

As mentioned previously, hazard-based duration models will use to explain the changes on the travel patterns of commuter trips during the peak period of RUC experiment using a fully parametric method and Minitab software. To describe the hazard functions that used a number of Figures will illustrate the different situations of peak period travel using durations of travel to work trips.

6.1. Baseline hazard for travel to work trips durations in the first week

To explain the travel to work trips during the first week in the peak period a set of durations of trips of travel to work (commuter trips) has been applied using hazard based duration models. As mentioned above in table 2 the lognormal distribution is the best-fit distribution.

Firstly, as can be seen Figure 4 shows the probability density function (a), goodness of fit (b), survival function (c) and the hazard function (d) for travel or journey to work trip durations that conducted by the drivers participated in the first week of the study during peak period using the Lognormal distribution which is according to the AD and COR tests the best fitted model for the first week data. It also includes the parameter estimates and calculated statistics. Interpretation of these functions can be explained using the duration of 20 minutes of travel to work trips. It can be seen that the probability density function shows that 56% of travel to work trips have duration of 20 minutes. The goodness of fit plot (with correlation $R = 0.94$) indicates a very high degree of correlation between the lognormal distribution and

the observed values. The largest deviation occurs for the shorter and longer journey times.

From the survival function (c) one can see that less than half of travel to work trips have a duration greater than 20 minutes and more than the half have durations less than or equal to 20 minutes. The hazard function presents the ratio of the probability of a given trip duration relative to the total number of trip durations greater than this particular duration (d). Longer and shorter duration trips than the duration at the maximum hazard value (here about 20 minutes) are more likely to remain because the hazard (the prevention or disincentive) is lower.

The discussion of each step of the hazard theory has been presented here for clarity and to ensure understanding of the basics.

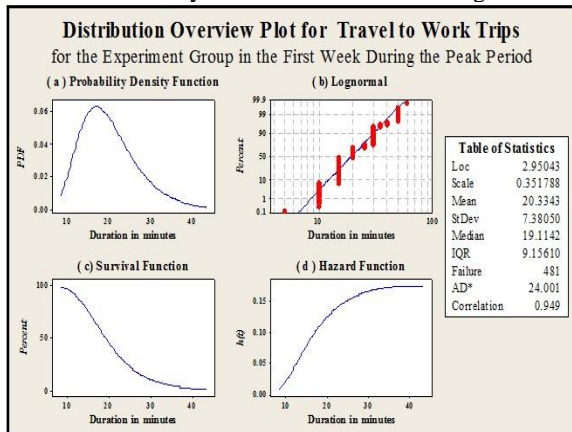


Fig.4: Distribution overview plot for duration of travel to work in the first week.

6.2. Baseline hazard for travel to work trips durations in the first week compared to the second week during the peak period

To investigate the changes that occurred on travel patterns during the second week of the field experiment of RUC, and according to the goodness of fit test the data of trips durations of travel to work during the peak period have applied using the baseline of hazard model and lognormal distribution which is the best fitted distribution for the field experiment data (Table 3).

Figure 5 shows the baseline hazard for durations of travel to work trips for the first week trips compared to second week trips during the peak period using two types of data (durations of trips by cars and durations of trips by other travel modes). The differences in the baseline hazard for travel to work trips in the second week during the peak period using cars and all other modes of travel and first week trips are evident from the Figure.

In general, for the first week, the hazard rate is higher for trips longer than about 12 minutes compared to second week trips durations for cars and other modes. The reverse is true for shorter than 10 minutes durations. This means that the disincentive to first week trips compared to the second week is respectively higher, and lower for shorter than 10 minute trip durations suggesting that the longer trips for the second week have more chance of surviving than for first week. This is counter intuitive result that indicates the most changes which have made during the second week were on the shorter trips more than longer trips.

Table 3: Goodness-of-fit tests for duration of travel to work for the second week trips using different modes

Distribution	Test Statistic Value			
	Week 2 (all mode trips)		Week 2 (car trips)	
	AD	COR	AD	COR
Weibull	19.64	0.934	30.32	0.907
Exponential	103.77	-	103.3	-
Normal	14.87	0.948	18.83	0.920
Lognormal	12.01	0.954	14.63	0.951
Logistic	18.32	0.939	21.58	0.914
Loglogistic	15.58	0.947	18.11	0.940
Best-fit model	Lognormal			

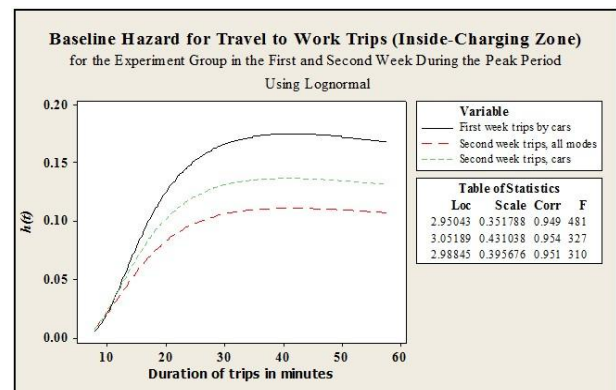


Fig. 5: Baseline hazard function for durations of travel to work trips in the first and second weeks using different modes of travel.

As stated above, the differences in the baseline hazard for durations of travel to work trips in the second week during the peak period using cars and other travel modes and first week trips is very clear. The Figure shows that the shape of the hazard function for car trips during the second week are (as expected)

different to the hazard shape for all modes trips; however, the difference is less than the difference to the first week cars trips. This is changes due to the fact that travel to work trips by car has shorter durations of travel than others modes trips such buses.

Moreover, in the second week car trips there was an increase in the hazard for shorter durations with change from all modes trips. In addition, it is clear that the maximum value of hazard rate has reduced for all modes trips during the second week suggesting shorter trips are surviving. The hazard curve again increases shifting slightly to higher deviations for cars than other modes.

6.3. Baseline hazard for travel to work trips durations for the control group

Another suggestion can be used to realise the changes that occurred during the second week after introducing the RUC scheme is the comparison study between the travel patterns of real experiment group (participated drivers of RUC experiment) and travel patterns of the control group (normal drivers).

Firstly, the study will use the control group data to recognise the main changes in the travel patterns during the two weeks of the study and Table 4 provides that the Lognormal distribution is the best suited distribution for durations of travel to work trips for the control group data during the peak period for the two weeks. From Figure 6, it can be seen that the shapes of the three functions; probability density function, survival function and hazard function are quite different for the first week trips of the control group and the second week. The control group trips trends are steady for the

two weeks. This suggests that in general shorter and longer trips for the control group for the two weeks are remained without any changes compared to travel to work trips for the real experiment group which have significantly difference. This has been shown in Figure 5 for the real experiment group trips in second week, the longer trip durations have become longer and this due to the fact that a number of drivers who driving for short term have a chance to change their mode of travel from cars to other modes such as buses (which can be explain in more details by Figure 7 (a) and (b).

Table 4. Goodness-of-fit tests for durations of travel to work for the control group

Distribution	Test Statistic Value			
	Control group Week 1		Control group Week 2	
	AD	COR	AD	COR
Weibull	12.76	0.930	17.68	0.918
Exponential	75.15	-	76.6	-
Normal	8.62	0.951	11.24	0.940
Lognormal	7.42	0.954	9.17	0.949
Logistic	11.2	0.934	14.13	0.925
Loglogistic	9.49	0.938	11.62	0.935
Best-fit model	Lognormal			

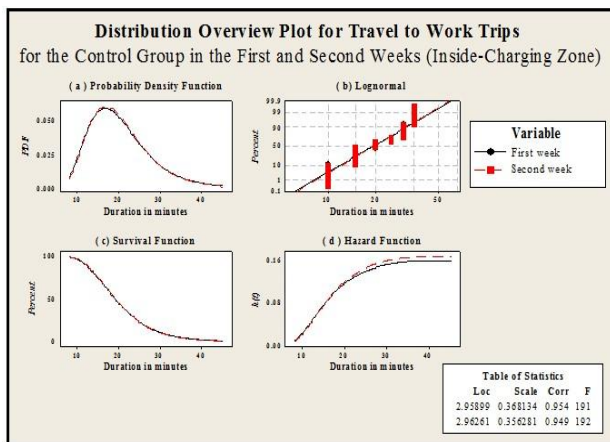


Fig. 6. Distribution overview plot for duration of control group travel to work trips

6.4. . Baseline hazard for travel to work trips durations for real experiment and control groups

In an attempt to gain further understanding of the changes of travel to work trips during the peak period of the field experiment of RUC using cars, control group trips were applied to compare with real experiment group trips. The results are presented in Figures 7(a) and (b). Figure 7(a) shows that the shapes of the hazard functions are quite similar for both experiment group and control group durations trips during the first week. A very little difference in the hazard rate of long durations for the experiment group durations trips where the hazard was higher.

It can be seen that the hazard rate dramatically increases with increasing trip duration until the trip duration reaches approximately 30 minutes. After that the hazard rate gradually steady with increasing durations of trip. However, the hazard values for the experiment trips a little bit higher than the control group trips for trips with 20 minutes durations and more. This suggests that in general longer trips for control group were much than longer for real experiment group trips comparing to the

shorter trips for both groups. This suggested that the long durations trips for the control group more than durations trips of the experiment group comparing with the shorter trips. However, it is clear that the second week changes are quite different. The hazard values for the control group trips are higher than the experiment group trips.

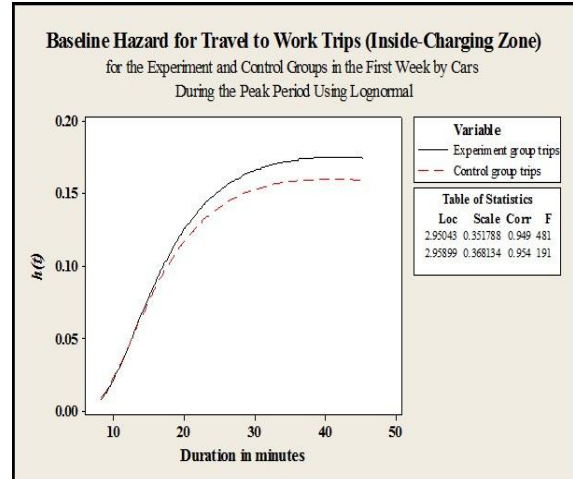


Fig. 7(a). Baseline hazard for peakperiod trips in the first week forreal experiment and control group

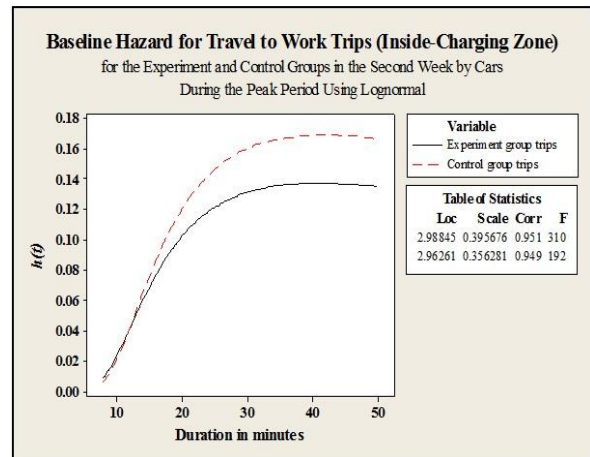


Fig. 7(b). Baseline hazard for peakperiod tripsin the second week for real experiment and control group

As has been seen from Figure 7(a) and (b) the shapes of hazard rates for the two weeks trips for the control group are similar. This suggests that the changes that occurred only with the real experiment group trips as has been shown in Figure 7(b). The decrease of hazard values for the real group trips in the second week means the decrease was in the trips of shorter durations. Also, it is clear in Figure 7(b) that the changes of hazard values starts from 15 minutes durations where the hazard curve increases slightly to higher deviation. This effect evident over such a short term is surprising because charging scheme effects are more likely to take place over shorter trips more than longer trips.

7. Conclusion

RUC is considered as a practical technique used to solve or reduce traffic congestion and transport problems. In Benghazi field-based RUC experiment the results stated that during the

restricted hours, RUC policy can have a positive impact in reducing traffic congestion with reduction of car trips crossing restricted areas during peak period by around 35.5%. The results proved that the lognormal distribution presents the best fit for the journey-to-work trips data. The hazard function was used to gain a fundamental understanding of the characteristics of the changes in the patterns of travel during the study period have been presented. The research has indeed shown that the hazard theory does highlight interesting features that prove the positive impacts of road charging policy.

References

- [1] Bhat, C. (1996), A hazard based duration model of shopping activity with nonparametric baseline, specification and nonparametric control for unobserved heterogeneity, *Transportation research B*, **30**(3) pp189-207.
- [2] Bowman, J. and Ben-Akiva, M. (2000). "Activity-based disaggregate travel demand model system with activity schedules". *Transportation research A* **35**(1) pp. 1-28.
- [3] Chow, V. (2006), *The Impact of Road-User Charging on Households' Mobility and Activity Participation Patterns*, Ph.D. Dissertation. Newcastle University.
- [4] Doxiadis Associates, (1989), *Benghazi region, Baladiyat of Benghazi, final report on the master plan*, DOX-LIB.
- [5] Ettema, D., Borgers, A. and Timmermans, H. (1995), Competing the risk hazard model of activity choice, timing, sequencing, and duration, *Transportation research record* 1493, pp. 101-109.
- [6] Franciscs J. and Ingrey M. (2000). *The EUROTOLL project: road user responses to transport demand management*. Road Transport Information and Control, conference Publication No.472, pp. 121-125.
- [7] Hensher, D. and Mannering, F. (1994), Hazard-based duration models and their application to transport analysis, *Transport reviews* vol. **14**, no. 1, pp. 63-82.
- [8] Hensher, D., and Button, K. (2000), *Handbook of transport and environment*, London Elsevier Ltd.
- [9] Hug, K., Mock-Hecker, R. and Wurtenberger, J. (1997), Transport demand management by electronic fee collection in a zone-based pricing scheme, the Stuttgart MOBILPASS field trial, *Transportation research record*, pp. 69-76.
- [10] MOTOS Handbook (2008), *Engineering statistics handbook*, Accessed on November 2008.
<http://www.itl.nist.gov/div898/handbook/index.htm>.
- [11] Nielsen, O. A. (2004), Behavioural responses to road pricing schemes: Description of the Danish AKTA experiment, *Intelligent transportation system*, **8**, pp. 233-251.
- [12] O'Mahony, M., Geraghty, D. and Humphreys, I. (2000), Distance and time based road pricing trial in Dublin, *Transportation* **27**, pp. 269-283.
- [13] Pas, E. (1996), Recent advances in activity-based travel, *Activity-based travel forecasting conference*, USA.
- [14] Safour, A. (2011), *The impact of road user charging in activity travel patterns in Libya*, Ph.D. Dissertation, University of Salford, United Kingdom.
- [15] Schonfelder, S. and Axhausen, K.W. (2001), Analysing the rhythms of travel using survival analysis, *Transportation research Board*.
- [16] Srinivasan, S. (2004), *Modelling household interactions in daily activity generation*, Ph.D. Dissertation. The University of Texas at Austin.
- [17] Statsoft, *The creators of statistica*, (2008), Accessed on November 2008.
<http://www.statsoft.com/company/webcasts/>
- [18] *Transport modelling: towards operational standards in Europe*. Accessed on November 2008. <http://www.motosproject.eu>.
- [19] Whittles, M. (2003), *Urban road pricing: public and political acceptability*, Hampshire: Ashgate Publishing Limited.
- [20] Zhong, M. and Hunt, J. D. (2005), Modelling household weekend activity durations in Calgary, Annual Conference of the Transportation Association of Canada.

An Implementation of Fuzzy Logic Technique to Predict the Material Removal Rate in Abrasive Water Jet Machining Process

Omar M Elmabrok^{a*}, and Abdel Aziz M Badi^b

^{a, b} *Benghazi University, Benghazi, Libya*

* Corresponding author. Tel.: +218-092-596-1571; e-mail: omar.elmabrouk@uob.edu.ly

ABSTRACT

In this study, the material removal rate values, obtained using machining abrasive water jet (AWJM), were modelled using fuzzy logic. The input variables considered are pressure, abrasive flow rate, orifice diameter, focusing tube diameter and standoff distance while the output variable was material removal rate (MRR). Fuzzy logic was developed using Matlab 2013. The mean absolute percentage errors (MAPE) of the predicted values was employed to compare the results with the previously published results obtained using response surface method technique. The results showed that the predictive model using fuzzy logic model has reduced the errors by 0.28%, which means, using fuzzy logic model to predict material removal rate is sufficiently accurate.

Keywords: Prediction, Material Removal Rate, Fuzzy logic model.

1. Introduction

Abrasive water jet cutting is a novel machining process capable of processing wide range of hard-to-cut materials. The cutting power is obtained by means of a transformation of a hydrostatic energy (400MPa) into a jet of an ample kinetic energy (nearly 1000 m/s) to disintegrate the material. The required energy for cutting materials is obtained by pressurizing water to ultrahigh pressure and forming an intense cutting stream by focusing high-speed water through a small orifice. The use of the AWJ cutting is based on the principle of erosion of the material by the impact of jets. Each of the two components of the jet, i.e. the water and the abrasive material has a specific purpose. The primary purpose of the abrasive material within the jet stream is to provide the erosive forces. Abrasive water jet process is similar to Abrasive Jet Machining AJM excluding that in this case water is used as a carrier fluid in place of gas. These processes offer merit of cutting electrically non-conductive as well as difficult to machine materials comparatively more rapidly and efficiently than other processes.

Figure 1 shows the cutting head of AWJM which includes mainly orifice abrasive mixer, focusing tube, and nozzle [1], and was a studied prediction of MRR and SR for Aluminum 6061 alloy by machining through Abrasive water jet machining parameters in put pressure, abrasive flow rate, orifice diameter, focusing tube diameter and standoff distance on the response (MRR) using Fuzzy Logic (FL) [2].

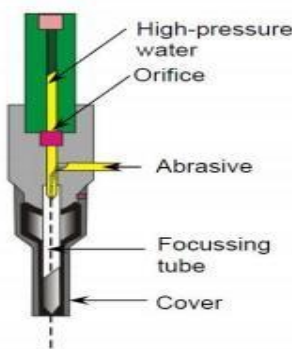


Fig. 1: Cutting head of AWJM [1].

The objectives of this paper are stated as follows:

- To predict material remove rate (MRR) using Fuzzy logic, as a function of five different parameters pressure, abrasive flow rate , orifice diameter, focusing tube diameter and standoff distance ,
- To compare results with a previous work.

2. Experimental details

2.1. Material

Copper Iron Alloy was the target material used in this experiment.

2.2. Experimental design

The number of experiments shown in Table 1 was obtained from previous work [1]. As there are five input parameters namely water pressure, abrasive flow rate, orifice diameter, nozzle diameter and standoff distance therefore total 26 experiments were studied. The output response selected for these experiments is Material Removal Rate (MRR). The MRR has been calculated using the following expression.

$$MRR = (W_i - W_f) / T_m(1)$$

where:

W_i = Initial Weight (kg).

W_f = Final Weight (kg).

T_m = Machining Time(min).

The upper (+1) and lower (-1) levels of all the four parameters and their designations are shown in Table 2.

The fuzzy rules are expressed in the form of fuzzy conditional statements R_i of the type R_i : if x is small, y is large THEN z is large Where x and y are fuzzy variables, and small and large are labels of fuzzy set.

If there are $i=1$ to n rules, the rule set is represented by union of these rules, $R = R_1 \cup R_2 \cup \dots \cup R_n$ [3].

A fuzzy logic controller is based on a collection of control rules. The execution of these rules is governed by the compositional rule. In this study, the triangular membership functions were used for the input process parameters such as water pressure, abrasive flow rate, orifice diameter, nozzle diameter and standoff distance to predict the material removal rate in AWJM of Copper Iron Alloy. The membership function for each input variables were divided into three levels (low, medium and high) and output variable was divided into six levels (very very low, very low, low, medium, high and very high). The fuzzy logic controller was Median type and contained a rule base. This base comprised of groups of rules and each output was defined by twenty-six rules. The rules based on knowledge to predict the material removal rate in AWJM of Copper Iron Alloy are given in Table 3.

The fuzzy inputs are linguistically divided into three levels such as low (L), medium (M) and high (H) which shown in Figure 3.

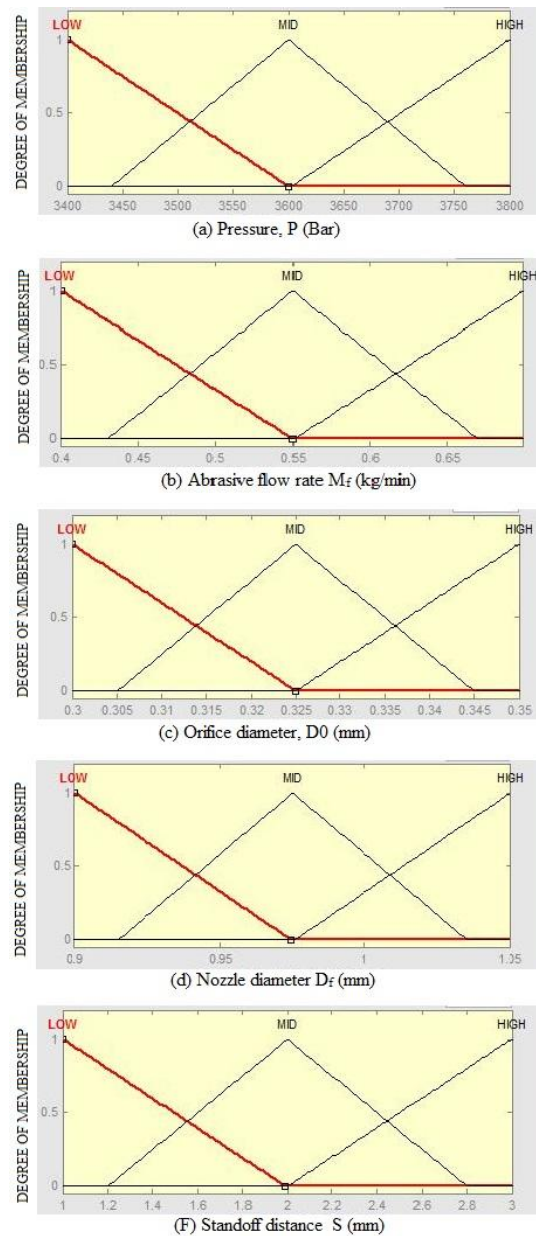


Fig. 3: Membership functions for input process parameters: (a) Pressure, P (b) Abrasive flow rate, M_f (c) Orifice diameter, D_0 (d) Nozzle diameter, D_f and (F) Standoff distance, S of AWJM of Copper Iron Alloy

Figure 4 shows the fuzzy output linguistically divided into six levels such as v v low (VVL), very low (VL), low (L), medium (M), high (H) and very high (VH).

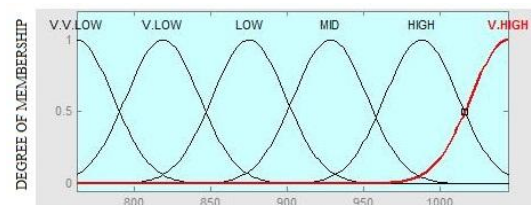


Fig. 4: Material removal rate MRR (mm³/min).

4. Simulation of Fuzzy Logic Model

In this study, the fuzzy model has been developed based on 26 experiments of AWJM of Copper Iron Alloy process parameters. The fuzzy model was simulated for test cases that has been done within the range of the fuzzy set. The experiments was conducted

for the three levels of each process parameters. The purpose of the simulation was to minimize the error of outputs for test case experiments. A MATLAB Simulink model was developed to predict material removal rate of the AWJM of Copper Iron Alloy process. Moreover, to confirm the adequacy of fuzzy logic model, the predicted values of the material removal rate predicted by using the proposed fuzzy model were compared with the previously published predicted values of the material removal rate of the AWJM of Copper Iron Alloy process by using RSM, these comparison is shown in Table 4 (Appendix) with their mean absolute percentage error (MAPE).The MAPE for the predicted of material removal rate by using the proposed fuzzy logic model is lower than the predicted of material removal rate by using RSM, percentage of the error was observed to be 0.28 % .

5. Conclusions

In this study, an attempt was made to predict the material removal rate in AWJM of Copper Iron Alloy as affected by the pressure, abrasive flow rate, orifice diameter, focusing tube diameter and standoff distance. The fuzzy clustering technique used was found to be adequate for establishing the relationship between the input process parameters and the output.The developed fuzzy logic model was also tested by comparing the results with a previously published results using RSM technique. The comparison was carried out based on the mean absolute percentage error between the predicted values and the experimental values and is shown in Figure 5.The fuzzy model gave lower mean absolute percentage error.

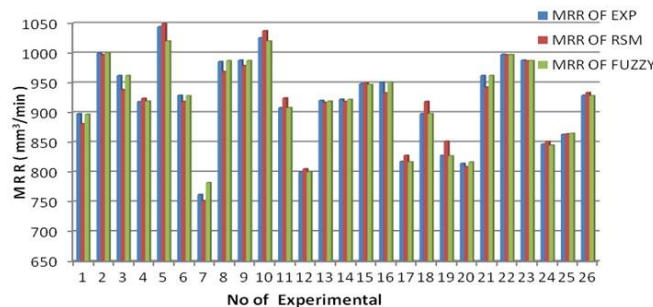


Fig. 5: Comparison of results between experimental and predicted MRR using RSM and fuzzy logic.

References

- [1] Aultrin, K.S. and Anand, M. (2014). Optimization of Machining Parameters in AWJM Process for a Copper Iron Alloy Using RSM and Regression Analysis. International Journal of Emerging Engineering Research and Technology. Volume: 2. Issue: 5. 19-34.
- [2] JaiAultrinKs, M. Dev Anand. Application of Fuzzy Logic Approach for Prediction of Machining Parameters by AWJM Process on Aluminum 6061 Alloy. Journal of Chemical and Pharmaceutical Sciences. ISSN: 0974-2115.
- [3] Omar M Elmabrouk (2014). Predating Surface Roughness of WEDC of SICP/6061 Al MMC Process Using Fuzzy Logic.
- [4] Bandler W. and Kohout L. J., 1988. Special properties, closures and interiors of crisp and fuzzy relations, Fuzzy sets and Systems, Vol. 26, No. 3, pp. 317-332.

APPENDIX

Table 4: The Experimental, Predicted and Mean Absolute Percentage Error of the Material Removal Rate of the AWJM of Copper Iron Alloy for Test Cases.

N o.	Experimental MRR, (mm ³ /min)	Predicted MRR, Using Fuzzy, (mm ³ /min)	Predicted MRR, Using RSM,(mm ³ /min)	Error Using Fuzzy (%)	Error Using RSM (%)
1	897.8	897	880.93	0.000891	1.878906494
2	1000.03	1000	997.11	3E-05	0.291186314
3	961.93	962	938.19	7.28E-05	2.467892154
4	918.21	919	923.71	0.00086	0.599155912
5	1043.96	1020	1049.13	0.022951	0.495263181
6	928.76	928	918.39	0.000818	1.116425826
7	762.29	782	751.80	0.025856	1.375881882
8	985.39	987	968.45	0.001634	1.718833863
9	987.8	987	978.60	0.00081	0.931023537
10	1025.41	1020	1037.33	0.005276	1.16340927
11	907.89	908	924.33	0.000121	1.810895979
12	800.02	800	805.25	2.5E-05	0.654058586
13	920.3	919	916.79	0.001413	0.380924047
14	922.4	922	918.39	0.000434	0.434618007
15	948.38	947	949.67	0.001455	0.136459278
16	950.62	951	932.76	0.0004	1.878030128
17	817.84	817	827.91	0.001027	1.232423151
18	897.8	898	918.39	0.000223	2.293504511
19	827.89	827	851.72	0.001075	2.879229729
20	814.54	817	808.75	0.00302	0.710341972
21	961.93	962	942.45	7.28E-05	2.024161633
22	997.56	997	996.82	0.000561	0.073196499
23	987.8	987	986.82	0.00081	0.098440879
24	846.98	845	851.37	0.002338	0.519131503
25	863.27	865	864.11	0.002004	0.097367683
26	928.76	928	933.38	0.000818	0.497468291

Dynamic Performance of a Sensorless Speed Control for Induction Motor Drives based on Model Reference Adaptive System

Haytham Mustafa^{a,*}, Saad. M. Saad^b, N. El-Naily^c, Salwa Almoshity^d, and Mohamed A. Almaktar^e

^{a,b,d,e}College of Electrical & Electronics Technology, Benghazi, Libya

^cGeneral Electric Company of Libya, Benghazi, Libya

* Corresponding author-mail: Heithamy@ gmail.com

ABSTRACT

Sensorless vector control is greatly used and applied in induction machine drives instead of vector and scalar control for their reliability and robustness, and very low maintenance cost. The estimation of the rotor speed in MRAS-based technique obtained by comparing the output of the adjustable and adaptive models instead of using costly speed sensor gives the sensorless vector control great fortune. MRAS-based techniques are one of the best methods to estimate the rotor position and speed for its performance and stability. In this paper, MRAS-based technique used to estimate rotor speed based on rotor flux estimation, the estimated speed in MRAS used as a feedback for the vector control system. Modeling and simulation of the induction machine and the vector control drives implemented in MATLAB/SIMULINK. Simulation results of the proposed MRAS rotor speed technique are presented. The results show stability and accuracy for the proposed technique.

Keywords: Induction Machine, Field-Oriented Control, Vector Control, Six-Switch Three-Phase Inverter (SSTPI), Sensorless Control.

1. Introduction

In many applications that consist of electromechanical systems, the control of speed, torque, and position is significantly important, such as mechanical robots, elevators, and automated factories. The main purpose of any machine control system is to extract and endurance the energy in an efficient way and in wide speed range control. The controlling of wind energy systems through advanced drives are also needed for maximum power point tracking in variable wind speed and contrastive forecasting. In the near future with the increase of dispatchable energy sources, the need for production maximum torque per ampere is a quite crucial matter [1].

With the development in vector control method, the induction machines become a preferable replacement for DC machines. Even though induction machine categorized by their reliability and robust and simplicity in construction, the control and estimation in induction machine is more difficult than in DC drives. The complex dynamic behavior and the complicated calculations required to estimate the speed of induction machine increase the cost due to the use of more advanced microprocessors [2].

Despite the development of vector control method to estimate and control the rotational speed of the induction machine by mean of microprocessors, introducing shaft speed sensor also decrease the reliability and dependability of the induction machine. Therefore, orientation to sensorless ac drive solutions has become the most prospective method to overcome the issues comes from introducing shaft speed sensor in the induction machine. The most promising approach is the Model Reference Adaptive System (MRAS), due to their simplicity [3].

The research and developments in speed sensorless control of induction motor drives (IM) have been continued in the past decades. The MRAS-based technique is one of the most attractive techniques for sensorless control of IM in literature reviews [4, 5, 6]. The MRAS speed technique is based on the comparison between the output of the reference model and the output of adjustable model until the error vanishes between the two models [7, 8].

The integration of pure voltage signal is the common problem encountered the application of MRAS technique to induction

machine drives. Reference [9] suggest modifying the pure integration in voltage model to the low pass filter. Reference [10] propose adding linear transfer function as a high pass filter in both the reference and the adjustable models. Reference [11] suggest proposing a robust flux observer to improve the response of the low pass filter represented by [9]. The sensitivity of the model-based technique to motor parameter variation could influence its performance. Many papers provide experimental and simulation comparison between various technique, especially in the low-speed region.

This paper mainly concentrates and focus on the comparison between the performance of well-known indirect field Oriented control (IFOC) of IM which implies using speed sensor against the model reference adaptive system (MRAS).

2. Vector Control

Vector control of induction machine drives based on measuring the rotor speed from the feedback of the controller and compared with a reference speed, the resultant error between the commanded speed and the actual speed of the motor is the value given to the controller to regulate the motor speed.

The torque reference extracted from the controller used to calculate the d-q stator reference currents, then the reference currents resultant from the controller converted to abc components to compare with the actual stator currents of the motor to produce the error needed to regulate the speed in the current regulator. The rotor angle θ is also calculated from the rotor speed to convert the d-q stator currents to abc components. The d-axis current is used to obtain the rotor flux. The resulting abc currents used to generate Pulse-Width modulation (PWM) switching signals. The PWM switching signals govern the inverters to obtain the desired the stator voltages. Those switching pulses control the motor speed, electromagnetic torque, stator and rotor currents.

The operation of the vector control requires the use of the speed sensor in the induction machine. The measured speed from the sensor is the feedback to the controller, which used to compare it with the reference speed to produce the error needed for the current regulator. The resultant error produces the stator currents responsible for switching signals of the Three-phase inverters. Introducing shaft encoder in the induction machine

could decrease the reliability of the equipment and increase the cost of the induction machine. Issues come from integrating speed sensor in the induction machine arouse the orientation to the sensorless control of induction machine.

2.1. Indirect Field Oriented control theory

To apply Rotor Field Oriented technique, the rotor flux vector is forced to be aligned with d-axis of the synchronous rotating reference frame. As a result, the quadrature component of the rotor flux in the synchronous rotating reference frame is also forced to be zero. Hence $\lambda_{qr}^e = 0$, The q -axis current command can be calculated

$$I_{qs}^* = (-L_r/L_m)I_{qr}^* \tag{1}$$

Moreover, the torque command as a function of I_{qs}^* can be found as:

$$T_e^* = \frac{3P}{2} \frac{L_m}{L_r} (I_{qs}^* \lambda_{dr}^*) \tag{2}$$

In addition, the following relation gives the slip frequency:

The estimation of rotor speed become difficult and complex in the low-speed operation mode. since the machine inductance affects the estimation of the rotor flux. For that, the accuracy of the sensorless speed estimation depends on the accuracy in calculating machine model parameters. Therefore, the performance of Sensorless vector control techniques become poor in the low-speed range.

A relation between the rotor flux and the flux current command can be found from:

$$R_r I_{dr}^* + \lambda_{dr}^* = 0 \tag{4}$$

Moreover, I_{dr}^* is given by:

$$I_{dr}^* = \frac{\lambda_{dr}^* - L_m I_{ds}^*}{L_r} \tag{5}$$

They are used in slip angle calculation, which is added to the measured rotor angle to get the estimated rotor flux - vector space angle (indirect RFO method). This angle is called the synchronous command angle θ_e^* and is used to transform the stator and/or rotor currents, voltages and fluxes from the stationary reference frame to the synchronous reference frame(SYRF) and vice-versa.

The transfer function of PI is given by:

$$G_s = \frac{k_{ps} [1 + \tau_{cs} S]}{\tau_{cs} S} \tag{6}$$

The torque command, as the output of PI speed controller, can be written as a function of the input as:

$$T_e^* = \frac{k_{ps} [1 + \tau_{cs} S]}{\tau_{cs} S} (\omega_r^* - \omega_r) \tag{7}$$

The q - axis current command can be found as:

$$I_{qs}^* = \frac{1}{k_t} \frac{(\omega_r - \omega_r^*) k_{ps} [1 + \tau_{cs} S]}{\lambda_{dr}^* \tau_{cs} S} \tag{8}$$

The indirect current command I_{ds}^* , is set by the rotor flux level λ_{ds}^* , and is written as:

$$I_{ds}^* = \left(\frac{1}{L_m}\right)(\lambda_{ds}^* + I_{ds}^*) \tag{9}$$

Note that the value of I_{ds}^* is constant below the base speed and should be reduced in an inverse relation with the speed to achieve the field weakening. If the flux command level is kept constant, the relation between I_{ds}^* and λ_{ds}^* is simplified as:

$$I_{ds}^* = (1/L_m)\lambda_{ds}^* \tag{10}$$

As λ_{ds}^* is the rotor flux, the I_{ds}^* represents the rotor field producing component. After that the reference I_{qs}^* and I_{ds}^* are transformed to I_{qs}^{*s} and I_{ds}^{*s} in stationary reference frame and then to abc current commands using inverse park's transformation [2].

The current controller has been implemented in the rotor flux reference frame using PI regulators, the influence of parameters variations at low speed has been considered in this study. The parameters of the PI controller are tabulated in Appendix B.

3. Sensorless control of IM drives

Implementation of indirect field oriented control method of induction machines drives introduce speed sensor, which is necessary for the measurement of the motor speed. The speed measured by the sensor is used as a feedback for the controller to compare it against the reference speed desired. However, installation of shaft speed encoder in the induction machine require space on the machine shaft; moreover, it reduces the motor reliability and increases the cost of the equipment. It is possible to renounce the shaft speed encoder if the speed of the motor could be estimated by using the machine parameters, such as terminal voltage and currents. Most of the identification methods depend on the machine model. In order to obtain the stator flux vector, integration of the voltage vector in the stator voltage equation is required. Fore though, great importance to acquire accurate machine model for stable performance is required.

The estimation of rotor speed become difficult and complex in the low-speed operation mode. since the machine inductance affects the estimation of the rotor flux. For that, the accuracy of the sensorless speed estimation depends on the accuracy in calculating machine model parameters. Therefore, the performance of Sensorless vector control techniques become poor in the low-speed range.

As mentioned early, the estimation of motor speed is used in the closed loop control as a feedback signal for speed regulation. The MRAS-based method is the most attractive method among the sensorless vector control of induction machine drives and has a great potential. In our study, the performance of MRAS is compared and evaluated against the vector control technique.

3.1. Proposed Model reference adaptive system MRAS

The adaptive control methods have considered as a potential solution when high performance required for different and wide operation modes, especially when dynamic characteristics of the model is complex or even unknown. The Model Reference Adaptive System (MRAS) provide reliable and stable performance, the presence of reference adaptive model specifies the desired performance. The adaptive model use stator voltages and currents to compare the output of the adaptive model with the reference model. The rotor speed estimated based on the error from both models. A number of papers discussed MRAS technique [12-14]. The general scheme of MRAS field-oriented IM drives is shown in Figure1.

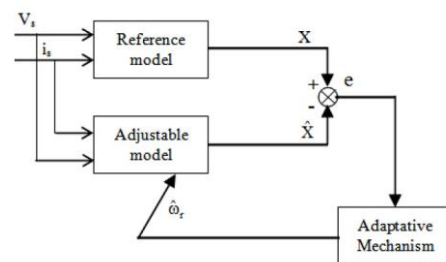


Fig. 1: Block diagram for MRAS control

The stator current is represented as:

$$\hat{i}_{ds} = \frac{1}{L_m} [\lambda_{dr} + T_r \lambda_{qr} \omega_r + T_r p \lambda_{dr}] \tag{11}$$

$$\hat{i}_{qs} = \frac{1}{L_m} [\lambda_{qr} - T_r \lambda_{qr} \omega_r + T_r p \lambda_{qr}] \tag{12}$$

Using the above equations, and estimated instead of measured speed, the stator current is estimated as:

$$\hat{\hat{i}}_{ds} = \frac{1}{L_m} [\lambda_{dr} + T_r \lambda_{qr} \hat{\omega}_r + T_r p \lambda_{dr}] \tag{13}$$

$$\hat{\hat{i}}_{qs} = \frac{1}{L_m} [\lambda_{qr} - T_r \lambda_{qr} \hat{\omega}_r + T_r p \lambda_{qr}] \tag{14}$$

The difference in the stator current is obtained as:

$$(i_{ds} - \hat{i}_{ds}) = \frac{T_r}{L_m} \lambda_{qr} [\omega_r - \hat{\omega}_r] \quad (15)$$

$$(\hat{i}_{qs} - i_{qs}) = \frac{T_r}{L_m} \lambda_{qr} [\omega_r - \hat{\omega}_r] \quad (16)$$

Multiplying by the rotor flux and adding them together:

$$(i_{ds} - \hat{i}_{ds})\lambda_{qr} = \frac{T_r}{L_m} \lambda_{qr}^2 [\omega_r - \hat{\omega}_r] \quad (17)$$

$$(\hat{i}_{qs} - i_{qs})\lambda_{qr} = \frac{T_r}{L_m} \lambda_{qr}^2 [\omega_r - \hat{\omega}_r] \quad (18)$$

By summing the above two equations

$$(i_{ds} - \hat{i}_{ds})\lambda_{qr} + (\hat{i}_{qs} - i_{qs})\lambda_{qr} = \frac{T_r}{L_m} (\lambda_{qr}^2 + \lambda_{dr}^2) [\omega_r - \hat{\omega}_r] \quad (19)$$

Hence, the error of the rotor speed is obtained as follows:

$$\omega_r - \hat{\omega}_r = [(i_{ds} - \hat{i}_{ds})\lambda_{qr} - (\hat{i}_{qs} - i_{qs})\lambda_{dr}] / K \quad (20)$$

The right-hand term seems as the term of speed calculation from the adaptive observer, so the speed can be calculated from the following equation:

$$\hat{\omega}_r = [(K_p(i_{ds} - \hat{i}_{ds})\lambda_{qr}) - (K_I \int (i_{ds} - \hat{i}_{ds})\lambda_{qr} - (\hat{i}_{qs} - i_{qs})\lambda_{dr} dt)] \quad (21)$$

The vector signals can be estimated if the speed and the stator current signals are known, the above equations provide information on the speed and current components. Those equations are firstly suggested by Blaschke and called Blaschke equations, which are creating the adaptive model [1]. The aim in MRAS-based method is to match the output of both the reference model which not consist the estimated rotor speed ω_r with the output of the adjustable model which consist the rotor speed estimated from the motor. If all the parameters of the motor are known, then the output of the both models should be matched.

The difference between the two models produce an error in the rotor flux reference, which is used to generate the desired speed ω_r . The error generated used as a feedback to the proportional-integral controller in tuning the motor speed. The stability and the accuracy of the dynamic performance depend and affected by the algorithm used in the MRAS-based method. In the most algorithms proposed, the PI controller gives satisfactory results. The accuracy of the algorithm used depend also on tuning the PI controller parameters.

4. Software Implementation

MATLAB/Simulink has been chosen to simulate the IM drives. The main advantages of MATLAB/Simulink are its easy implementation of any control algorithm, including linear control, fuzzy logic, neural networks and others. The graphical tools are comprehensive and very easy to use. There are some disadvantages, however, with Simulink. Incorporating models for real power semiconductors is not yet possible and the complexity of the blocks increase with the number of semiconductors used in the circuit. Therefore, the Power System Blockset (PSB) [15-16] was also used. The PSB is a special toolbox in Simulink, which simulate the power circuit by interconnecting the differential components comprising the real circuit. Compared to Simulink, PSB is simpler as it takes advantage of all MATLAB-Simulink capabilities. It has certain special blocks for simulating ac/dc motors. However, one can easily encounter some convergences problems with the PSB if the parameters are not set properly. Setting values for the blocks in PSB can become a very tricky part of the simulation. In this paper, most of the blocks shown were developed using Simulink, but certain blocks, such as the IGBT model, were taken directly from the PSB libraries.

5. Results

The aim of this study is to compare sensor and sensorless vector control schemes for induction machine drives. The steady state error and the dynamic response during speed step change and the resultant torque of each method can be interpreted as an indication of the accuracy and the reliability of each method. In addition, the sensorless algorithm proposed had been examined during the low-speed performance. Also, the applicability of each method to be implemented in the industrial applications also has been studied.

The study aims to evaluate the control characteristics of speed sensor and sensorless vector control schemes and observe the influence of each method strategy on the motor drives performance.

The evaluation of the system performance through simulation require exact modeling for all the elements of the system to measure the complexity of the proposed method on the dynamic response of the induction machine. To achieve that the simulation carried out by MATLAB/SIMULINK power system Blockset, the advantage of using power system Blockset is to simulate the power circuit with the control system proposed in the same diagram by choosing the proper fixed step integration algorithm. The calculation mechanism in both control systems is the same in both indirect field oriented control and model reference adaptive system. The major difference between the two methods is in the speed estimation, in the field oriented control method the speed is directly measured through shaft encoder speed sensor, while in model reference adaptive system the rotor speed estimated through the motor parameters. The studied system contains a 1 hp, 380 V induction motor fed by three-phase inverters, the parameters of the induction motor are tabulated in Appendix A.

6. Simulation results for the proposed drive system

For studying the response properties of multi-loop control of induction motor drive, a series of simulation have been carried out. In this simulation, the drive response of the control system, for the following cases were studied; at 150, 100 and 75 (rad/sec) speed references at full load.

6.1. Drive response at 150(rad/sec) speed reference

The induction motor drives response at 150(rad/sec) reference speed is used to evaluate the performance in terms of steady state errors and stability. The motor is subjected to full load conditions to evaluate the performance. Fig. 2 shows the estimated rotor speed response with its command speed of 150 rad/sec. It can be seen that the rotor speed is accelerated smoothly to follow its reference value. Fig. 3 shows the simulated (real) rotor speed response. It can be seen that the response of simulated and estimated rotor speed are very close. Fig. 4 shows motor developed torque. Fig. 5 and 6 show the q-axis and d-axis stator current components respectively. The d-axis current component is kept constant; this confirms the correct orientation. Also, the q-axis current profile is close to the motor developed torque, this means that the motor torque is a function of q-axis current. Fig. 7 shows the motor phase current.

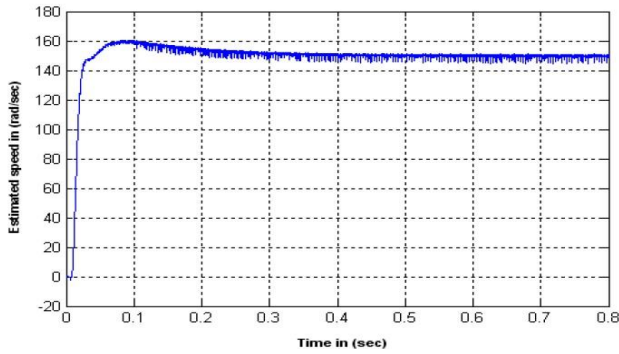


Fig. 2: Estimated Speed via MRAS.

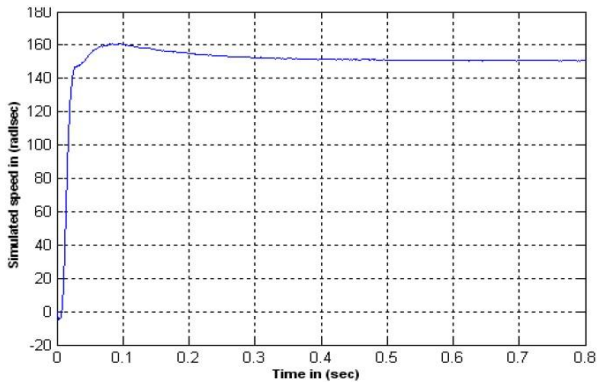


Fig. 3: Estimated Speed via IFOC.

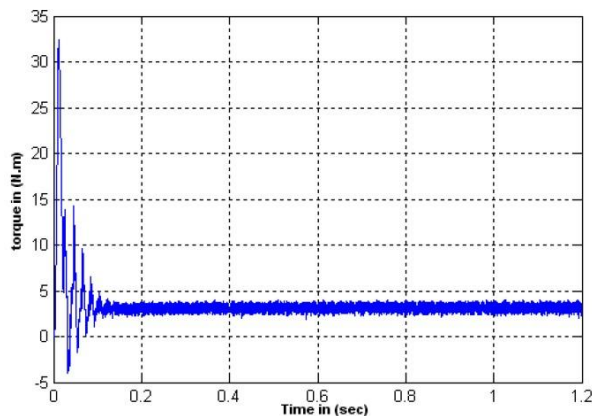


Fig. 4: Motor Developed Torque.

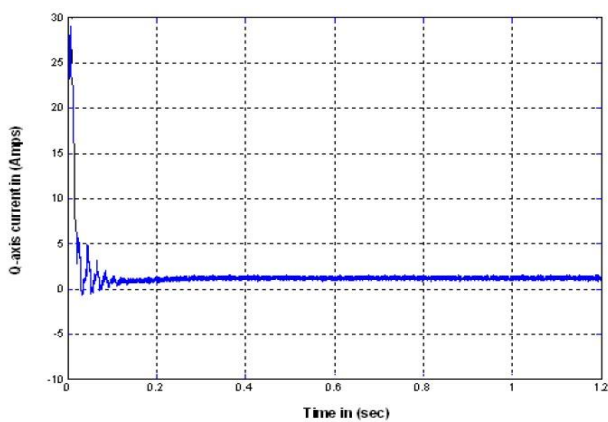


Fig. 5: Q-Axis Current.

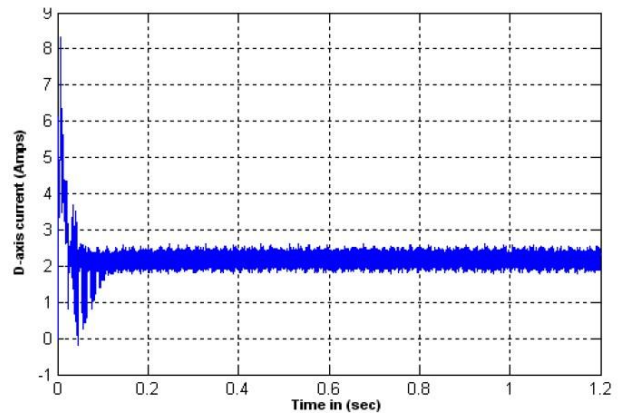


Fig. 6: D-Axis Current.

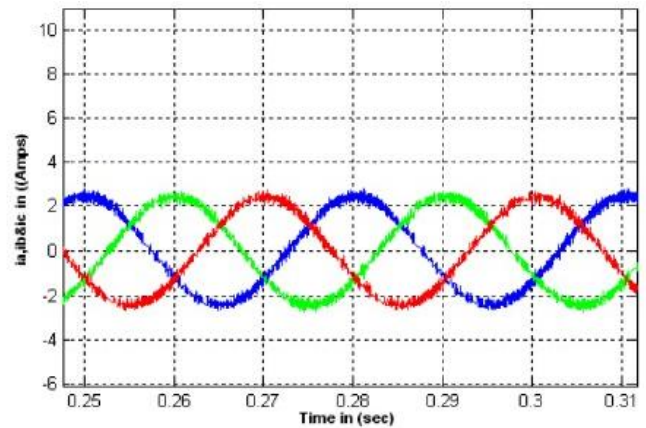


Fig. 7: Three-Phase Motor Current.

6.2. Drive response at 100(rad/sec) speed reference

Another operating point, when the motor subjected to 100(rad/sec) to study the proposed MRAS-based performance. Fig. 8 shows estimated rotor speed. It can be seen the pulsing in speed signal increase compared to 150(rad/sec). This means when speed decreases, the pulsing in the speed signal increase. The estimated speed is similar to simulated speed. Fig. 9 shows the simulated speed. Fig. 10 shows motor developed torque. Fig. 11 and 12 show the q-axis and d-axis stator current components respectively. Fig. 13 shows the motor phase current.

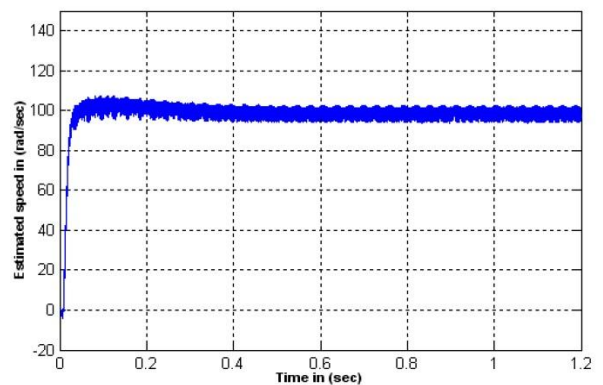


Fig. 8: Estimated Speed via MRAS.

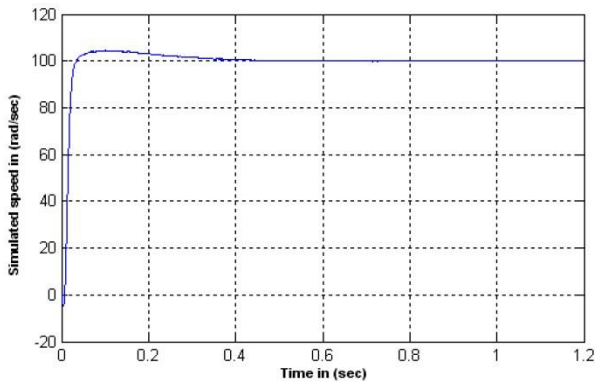


Fig. 9: Estimated Speed via IFOC.

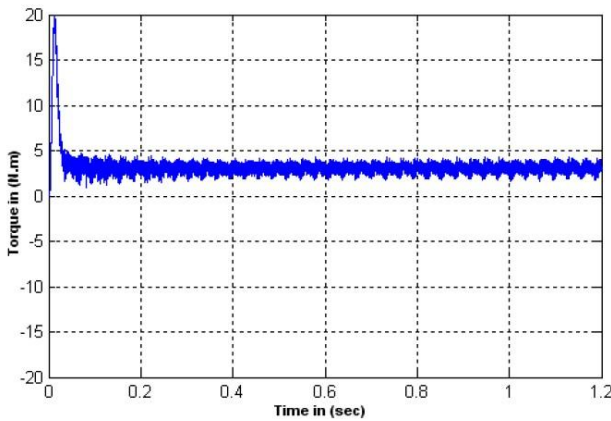


Fig. 10: Motor Developed Torque.

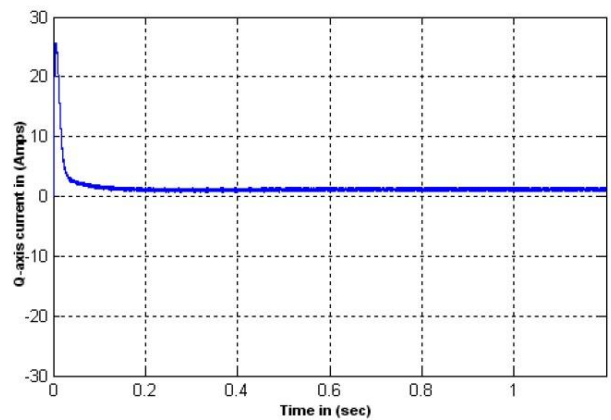


Fig. 11: Q-Axis Current.

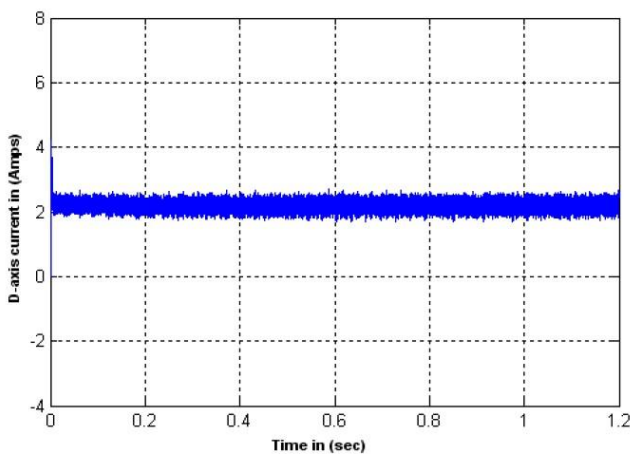


Fig. 12: D-Axis Current.

6.3. Drive response at 75 (rad/sec) speed reference

Another operating point, when the motor subjected to 75 (rad/sec) reference speed to study the proposed MRAS-based performance. Fig. 14 shows the estimated rotor speed response with its command speed of 75 rad/sec. It can be seen the pulsing in speed signal increases when speed decreases to 75(rad/sec). This problem existed in all methods of speed sensorless, because it is difficult to estimate the flux in low and zero speed. Fig. 15 shows the simulated (real) rotor speed response. It can be seen that the response of simulated and estimated is very close. Fig. 16 shows motor developed torque. Fig. 17 and 18 show the q-axis and d-axis stator current components respectively. Fig. 19 shows the motor phase current.

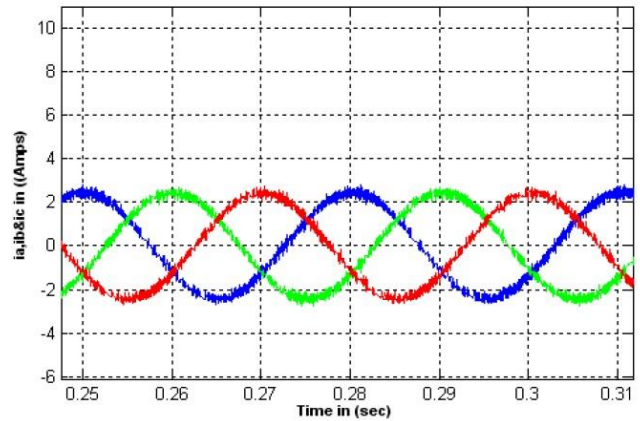


Fig. 13: Three-Phase Motor Current.

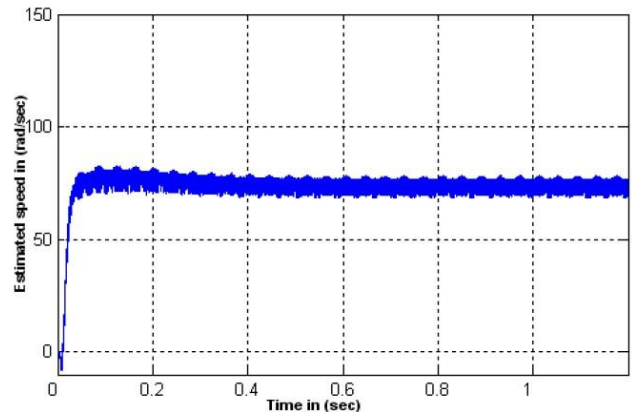


Fig. 14: Estimated Speed via MRAS.

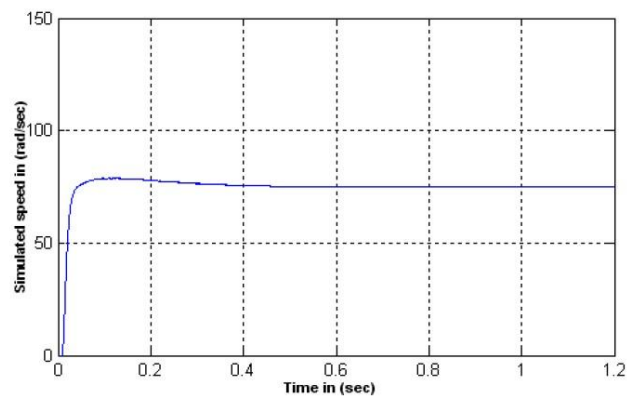


Fig. 15: Estimated Speed via IFOC.

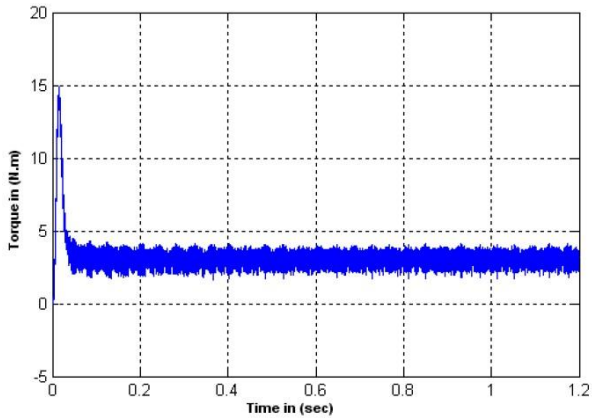


Fig. 16: Motor Developed Torque.

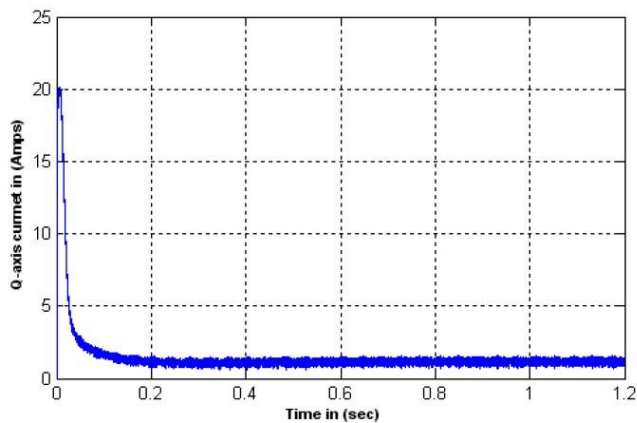


Fig. 17: Q-Axis Current.

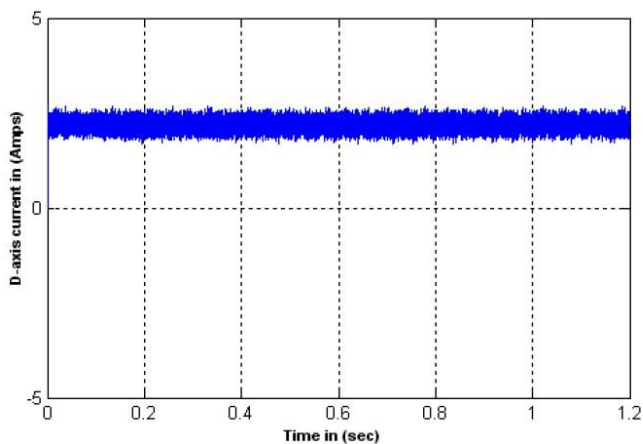


Fig. 18: D-Axis Current.

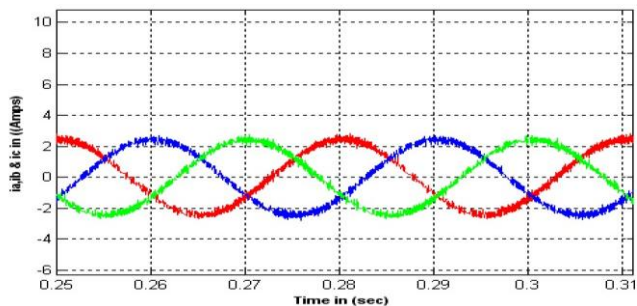


Fig. 19: Three-Phase Motor Current.

6.4. Drive response at step change

The motor response due to a step change in the command speed is used to evaluate the performance in terms of steady state errors and stability. The motor is subjected to step increase and decrease in the reference speed under loading condition to evaluate its performance. Fig. 20 shows the estimated speed; it is set initially at 100(rad/sec) at full load condition. After 0.4 second it increased to 150(rad/sec) and returned to 100(rad/sec) after 0.4 second. Fig. 21 shows the simulated speed, it can be seen that the response of simulated and estimated speed are very close. Fig. 22 shows the motor estimated developed torque, which correspondingly increases, and decreases during the step changes in the reference speed due to the dynamic response. Fig. 23 and 24 show the q-axis and d-axis stator current components respectively. Fig. 25 shows the motor phase current.

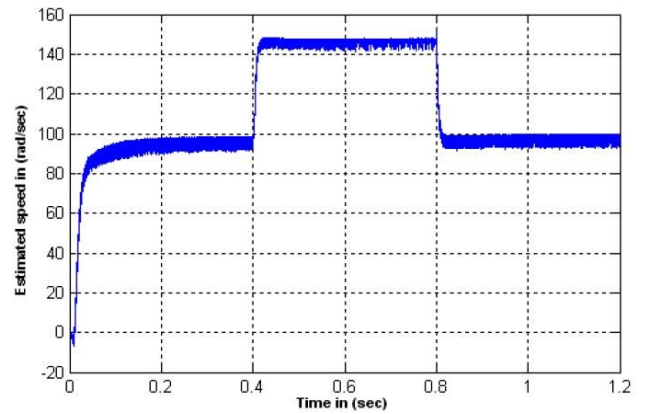


Fig. 20: Estimated Speed via MRAS.

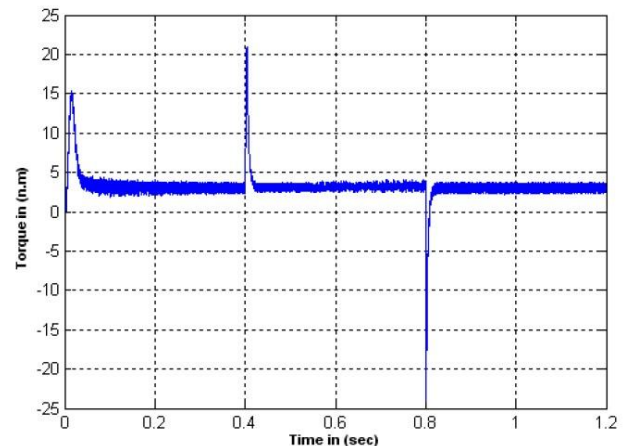


Fig. 21: Estimated Speed via IFOC.

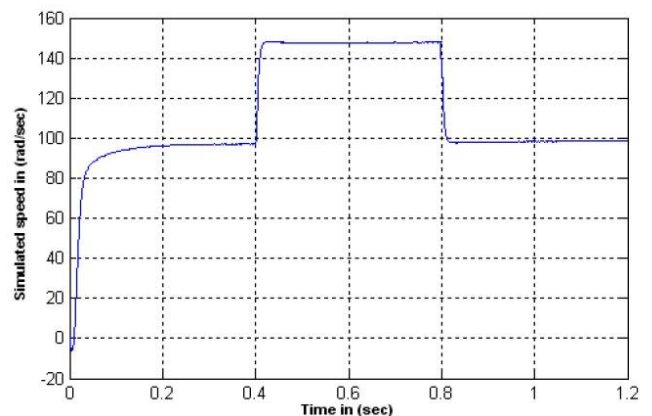


Fig. 22: Motor Developed Torque.

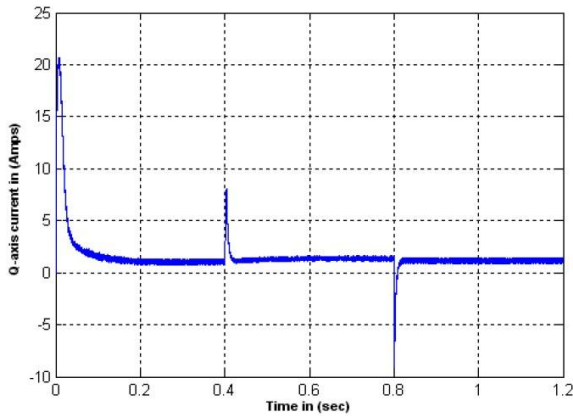


Fig. 23: Q-Axis Current.

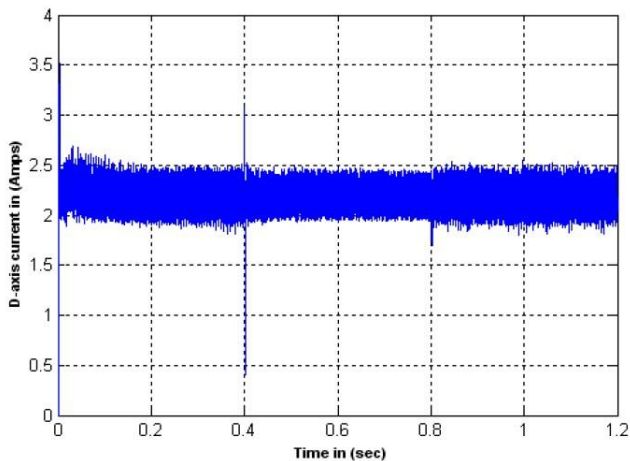


Fig. 24: D-Axis Current.

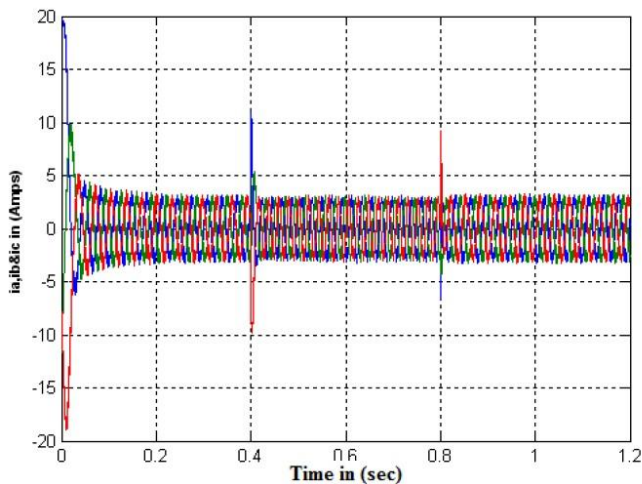


Fig. 25: Three-Phase Motor Current.

6.5. Drive response at Load impact

The motor response due to load impact in the command speed is used to evaluate the performance in terms of steady state errors and stability. The dropped amplitude of the system output such as rotor speed and its recovering time is the important performance specifications. Fig. 26 shows the estimated speed response when a full load impact is applied for 150 rad/sec. The motor started at no load and the full load is applied after 1.5 seconds. After one second, the load released. Fig. 27 shows simulated speed. It can be seen that the response of simulated and estimated speed are very close. Fig. 28 shows the motor estimated developed torque, which correspondingly increases, and decreases during

the step changes in the reference speed due to dynamic response. Fig. 29 and 30 show the q-axis and d-axis stator current components respectively. Fig. 31 shows the motor phase current.

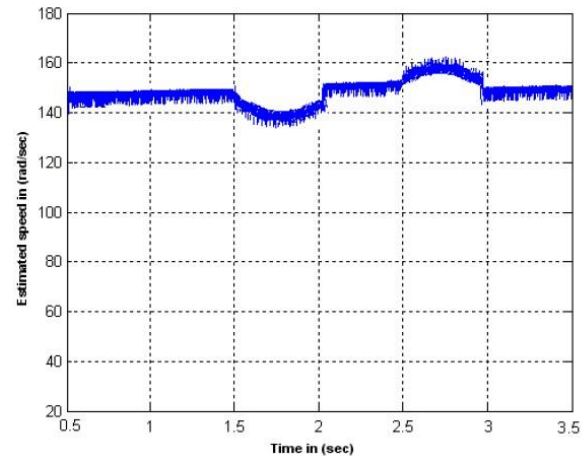


Fig. 26: Estimated Speed via MRAS.

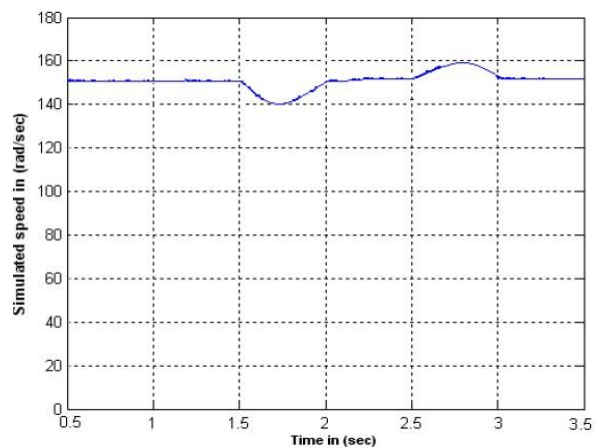


Fig. 27: Estimated Speed via IFOC.

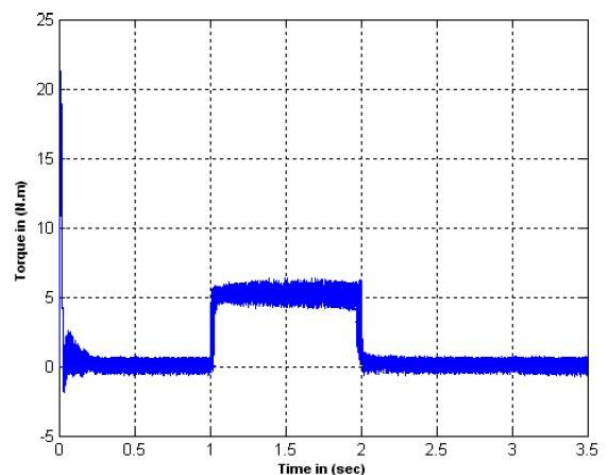


Fig. 28: Motor Developed Torque.

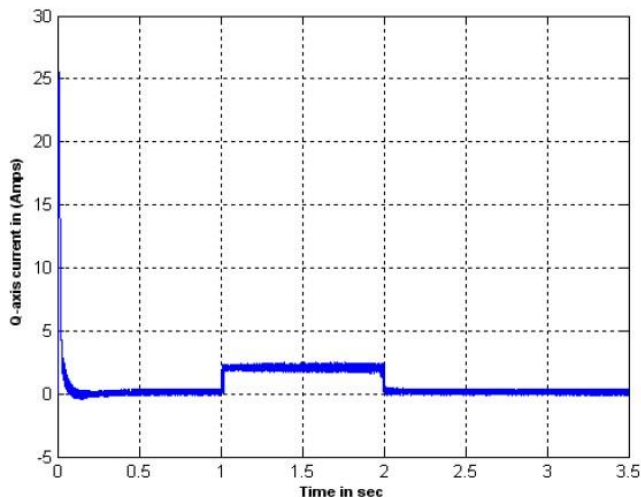


Fig. 29: Q-Axis Current.

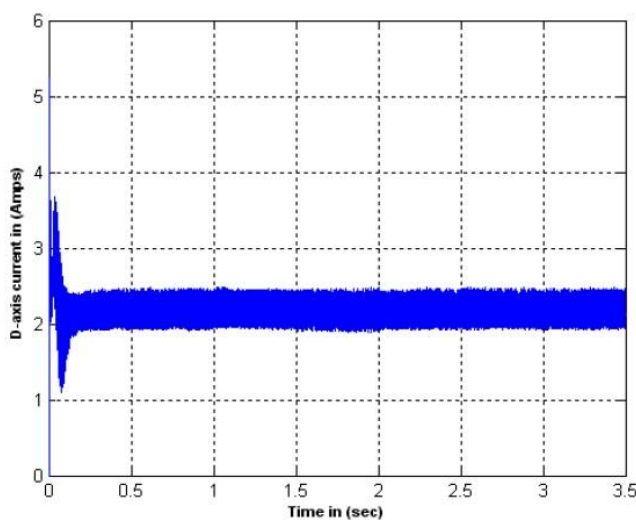


Fig. 30: d-Axis Current.

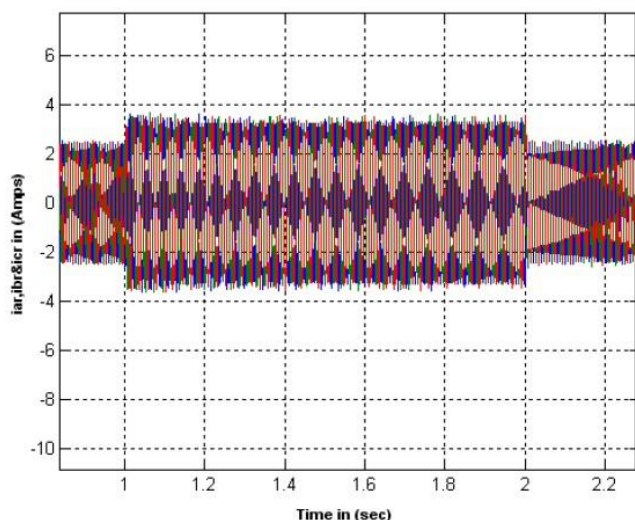


Fig. 31: Motor Developed Torque.

The induction motor can be controlled linearly by applying field orientation control scheme. Multiple loop control method has been investigated by simulation. Series of operating condition used to analysis the drive in the synchronous reference

frame have been carried out to verify the control scheme performance.

In addition to the above estimated variables, the rotor speed is estimated in sensorless control. To estimate the rotor speed, some other variables have to be estimated depending on the speed estimation algorithm used. In MRAS, both d- and q-axis components of rotor flux are estimated for reference and adjustable model. These variables are estimated using the stator voltages and currents of the motor to be controlled. The rotor speed depends on the difference between the outputs of the reference model and adjustable model. For MRAS, the problem of choosing the coefficients of the adaptation mechanism as well as loop stability is not straightforward, and it is clear in the oscillation and ripple on the estimated speed obtained by the MRAS-based method.

7. Conclusion

This study focused on the design, and simulation, of the sensorless drive system for induction motor drives, based on the estimation of the rotor speed, and used as a feedback signal for the drives. Speed sensorless control and vector control techniques for IM drives were simulated. The torque and speed characteristics obtained from those results were compared and investigated. In the different cases and scenarios simulated, it is evident that the proposed sensorless control method work just as well as the vector control method. The difference between the two from the hardware point of view is evident in decreasing the number of sensors (current or speed) that are necessary for vector control methods. Sensors generally make the difference in cost for drive control implementation. Because of this, there is a strong interest in vector-controlled drives without any shaft sensor. The advantage of speed sensorless IM drives are increased reliability (no possibility of tachometer failure), lower cost, and reduced the size of the drive system and elimination of sensor cable. However, there are some limitations in speed estimation with sensorless control methods, speed estimation methods experience problems at low speeds, which are responsible for poor performance, and oscillations in the estimated rotor speed. Also further investigation for the effect of the air gap flux saturation, which is concluded from our model should be considered and manipulated and implemented for further accuracy, Fuzzy logic methods for controlling IM drives, which used instead of conventional PI controller could filter and suppress the oscillations and ripples in the estimation of the rotor speed.

References

- [1] B.K. Bose, Modern Power Electronics and AC Drives, Prentice-Hall, Upper Saddle River, 2002.
- [2] T. Orłowska-Kowalska, M. Dybkowski, "Stator Current-based MRAS Estimator for a Wide Range Speed-sensorless Induction-Motor Drive", *IEEE Trans. on Industrial Electronics*, vol. 57, no. 4, April 2010
- [3] J. W. Finch and D. Giaouris, "Controlled AC electrical drives," *IEEE Trans. Ind. Electron.*, vol. 55, no. 2, pp. 481–491, Feb. 2008.
- [4] V. Verma, M.J.Hossain, T. Saha, C. Chakraborty, "Performance of MRAS Based Speed Estimators for Grid Connected Doubly fed Induction Machines during Voltage Dips," *IEEE 978-1-4673- 2729-9/12*, 2012.
- [5] Teresa Orłowska- Kowalska, Mateusz Dybkowski, "Stator – Current-Based MRAS Estimator for a Wide Range Speed- Sensorless Induction-Motor Drive," *IEEE Transactions on Industrial Electronics*, Vol.57, No.4, pp. 1296-1308, April 2010.

- [6] Abdelrahman Yousif EshagLesan, Mamadou Lamine Doumbia, Pierre Sicard, "Comparative Study of Speed Estimation Techniques for Sensorless Vector Control of Induction Machine," IEEE 978-1-4673-2421-2/12, pp. 4298-4303, 2012.
- [7] Ahmad Razani Haron, Nik Rumzi Nik Idris, "Simulation of MRAS-based Speed Sensorless Estimation of Induction Motor Drives using MATLAB/SIMULINK," First International Power and Energy Conference, Putrajaya, Malaysia, pp. 411-415, 2006.
- [8] Lin-Yu Lu, Tzu-Wei Yeh, Chia-Chi Chu, "Back-EMF-Based Model-Reference Adaptive Sensorless Control for Grid- Connected DFIGs," IEEE 978-1-4799-1303-9/13, 2013.
- [9] S. Tamai, H. Sugimoto, M. Yano, Speed sensorless vector control of induction motor with model reference adaptive system, Conf. Record of the 1985 IEEE- IAS Annual Meeting, pp. 613–620.
- [10] R.D. Lorenz, Tuning of field oriented induction motor controllers for high-performance applications, IEEE Industry Appl. Soc. Annu. Meet. (1985) 607–612.
- [11] H. Tajima, Y. Hori, Speed sensorless field orientation control of the induction machine, IEEE Trans. Industry Appl. 29 (1) (1993) 175–180.
- [12] S. M. Krishna and J. L. F. Daya, "Dynamic performance analysis of MRAS based speed estimators for speed sensorless induction motor drives," 2014 International Conference on Advances in Electronics Computers and Communications, Bangalore, 2014, pp. 1-6.
- [13] A. Y. E. Lesan, M. L. Doumbia and P. Sicard, "Comparative study of speed estimation techniques for sensorless vector control of induction machine," *IECON 2012 - 38th Annual Conference on IEEE Industrial Electronics Society*, Montreal, QC, 2012, pp. 4298-4303.
- [14] Rajalakshmi, D., et al. "Analysis of Speed Estimation for Sensorless Induction Motor Using Model-Based Artificial Intelligent Estimation Techniques. "Proceedings of the International Conference on Soft Computing Systems. Springer India, 2016.
- [15] User's Manual-Power System Blockset for use with Simulink, The Mathworks Inc., Natick, MA, 2001.
- [16] Advanced electric drives: analysis, control, and modeling using MATLAB/Simulink® / Ned Mohan, Copyright © 2014 by John Wiley & Sons, Inc. All rights reserved.

Appendix A: Induction machine data

A 1 HP, 380 V Three-Phase induction machine was used to simulate vector control, MRAS using MATLAB/Simulink with the following data:

Motor Rated Power	1 hp
No. of Poles	4
Motor Inertia	0.02 Kg.m ²
Friction co-efficient	0.0008 Kg.m ² /s
Stator resistance	7.4826 Ohm
Rotor resistance	3.834 Ohm
Stator self-inductance	0.4335 H
Rotor Self-Inductance	0.4335 H
Magnetizing inductance	0.4111 H

Appendix B: Vector Control Parameters

SYMBOL	PARAMETER'S NAME	VALUE	UNIT
λ_{rc}	Flux Command	0.9	P.U
P	Speed PI Proportion Gain	0.25	
I	Speed PI Integral Gain	1	

Appendix C: NOMENCLATURE

I_{qs}^*	Quadrature-Axis Component of the Stator Current Command in The Synchronous Reference Frame
L_r	Rotor Self Inductance
L_m	Mutual Inductance
I_{qr}^*, I_{dr}^*	Quadrature and Direct-Axis Component of the Rotor Current Command in The Synchronous Reference Frame
λ_{dr}^*	Direct-Axis Component of the Rotor Flux Command in The Synchronous Reference Frame
ω_{sl}^*	Command Slop Angular Speed
R_r	Rotor Resistance
ω_r^*	Rotor Speed Command
i_{ds}	Direct-Axis Component of the Stator Current
λ_{dr}	Direct-Axis Component of the Rotor Current
T_r	Rotor time constant
$\hat{i}_{ds}, \hat{i}_{qs}$	Direct and Quadratic Axis Estimated Stator Current
$\hat{\omega}_r, \omega_r$	Actual Rotor and Estimated speed

Modelling and Simulation of Multistage Flash Desalination Plants

Wael Abujazyah

College of Mechanical Engineering Technology, Benghazi, Libya
Tel.: +0218-92-511-4370; e-mail: wailali74@yahoo.com

ABSTRACT

This study describes the mathematical model developed for evaluating the performance of multistage flash (MSF) desalination plants at steady state operation. The governing equations are linearized and are arranged in a tridiagonal matrix form. The solution of these equations are obtained by a computer code written in visual basic language with friendly user format developed for this purpose. This code can predict the plant productivity with profiles of temperatures and flow rates for all stages in the unit. The present results were compared with some previous results presented in literature, and with the design data of MSF plant existed in Benghazi city. The comparisons show good agreement with these available data.

Keywords: System performance, Energy balance, Mass balance, Desalination Plants, Modelling, MSF.

1. Introduction

The goals of modeling and simulation in the process industry include improving and optimizing designs, and developing better insight into the working of the process, ultimately leading to the optimal operation and control of the process. A steady-state model consists primarily of algebraic equations that describe system process, mass balance and energy balance through the system cycle. It is mainly applicable for design purposes as well as for parametric studies of existing plants to evaluate their performance and to adjust or optimize operating conditions.

2. Literature review

Helal et al. [1] used a tridiagonal matrix model for steady-state simulation of MSFD plants. The set of equations was solved in a global manner by arranging the stage energy relations in the form of a tridiagonal matrix. He found this method stable and showed fast convergence. Marina Rosso et al. [2] described a steady state mathematical model developed to analyze the MSF desalination processes. The model allows calculating the plant productivity together with the profiles of temperatures and flowing rates in all the stages of the unit. Husain et al. [3] described the work done on modeling and simulation of multistage plant containing 15 recovery and 3 rejection stages. He used FORTRAN program for the steady state simulation based on tridiagonal matrix formulation. Good agreement was achieved by comparing with the vendor supplied as well as actual plant data. He stated that the TDM formulation, represents a more realistic situation in which the makeup seawater is directly fed to the last rejection stage from which the total brine recycle is drawn. Khawla A. Al – Shayji [4] explained how to apply modular and equation – solving approaches for steady state and dynamic simulations of large scale commercial MSF desalination plants using ASPEN PLUS (Advanced System for Process Engineering PLUS) and SPEEDUP (Simulation Program for Evaluation and Evolutionary Design of Unsteady Processes). His work illustrated the development of an optimal operating envelope for achieving a stable operation of a commercial MSF desalination plant using the SPEEDUP model.

This paper aims to model MSF plant using TDM formulation and to build a computer code that helps in evaluating the plant performance under design and operating parameters at steady state operation conditions to provide plant-working envelope. This code could help in building the system control loop by implementing it as one of the control modulus.

3. Description of the MSF process

Figure 1 shows a schematic diagram of the MSF system. The system involves six main streams: intake seawater rejected cooling seawater, distillate product, rejected brine, brine recycle and heating steam. The system contains flashing stages, a brine heater, pumping units, venting system, and cooling water control loop. The flashing stages are divided into two sections: heat recovery and heat rejection. The intake seawater is introduced into the inside of the condenser tubes of the last flashing stage in the heat rejection section. Similarly, the brine recycle stream is introduced into the inside of the condenser tubes of the last flashing stage in the heat recovery section. The flashing brine flows counters to the brine recycle from the first to the last flashing stage [1].

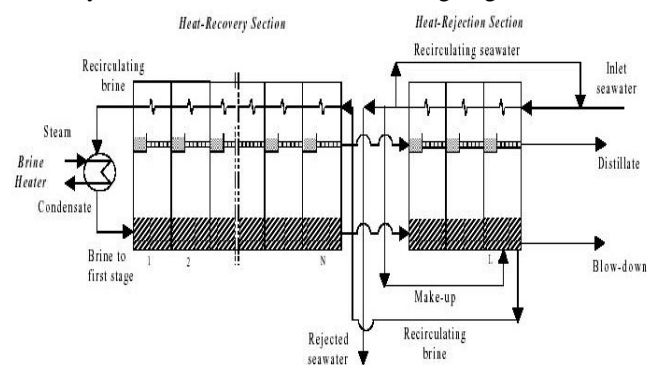


Fig.1: Recirculation brine multistage flash (MSF) desalination plant.

4. Mathematical model

The steady state mathematical model of the multi stage flash desalination process generally is developed under following simplifying assumptions:

- The product leaving any stage is salt free;
- The heat of mixing for brine solutions are negligible ;
- No heat lost in system;
- No subcooling of condensate leaving the brine heater.

The model equations are constituted of a set of mass and energy balances with their final form are given in the following. A detailed description of these equations is presented in reference [1].

The final form of the governing equation which is used to build TDM equation for any stage j , as shown in Figure 2, for the recovery and reject sections is:

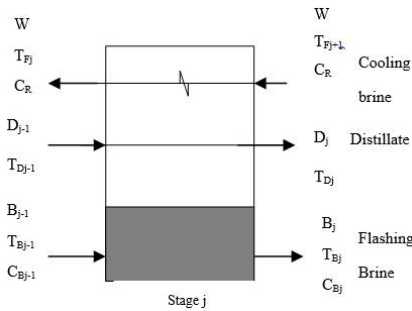


Fig. 2: General stage in an MSF plant.

$$(C_{1j})T_{Fj-1} + (C_{2j} - 1)T_{Fj} + (C_{3j} + 1)T_{Fj+1} = b_{3j} \quad (1)$$

Where;

$$C_{1j} = \left[\frac{b_{1j} a_{j-1}}{(1 - a_{j-1})} \right] \quad (2)$$

$$C_{2j} = \left[\frac{b_{1j}}{(1 - a_{j-1})} \right] - \left[\frac{b_{2j} a_j}{(1 - a_j)} \right] \quad (3)$$

$$C_{3j} = \left[\frac{b_{2j}}{(1 - a_j)} \right] \quad (4)$$

The first and last stages have particular characteristics, which are to be taken into account for deriving the TDM. The first stage in the recovery section receives no distillate stream from an external source. Further, T_{b0} the temperature of the flashing brine entering the stage is calculated from steam temperature. Thus the equation for this stage will be as follows:

$$(C_{21} - 1)T_{F1} + (C_{31} + 1)T_{F2} = b_{31} \quad (5)$$

$$C_{21} = - \left[\frac{b_{21} a_1}{(1 - a_1)} \right] \quad (6)$$

$$C_{31} = \left[\frac{b_{21}}{(1 - a_1)} \right] \quad (7)$$

The elements of the TDM in the last stage are such as:

$$C_{1j} T_{Fj-1} + (C_{2j} - 1) T_{Fj} = b_{3j} \quad (8)$$

Where,

$$C_{1j} = - \left[\frac{b_{1j} a_{j-1}}{(1 - a_{j-1})} \right] \quad (9)$$

$$C_{2j} = \left[\frac{b_{1j}}{(1 - a_{j-1})} \right] - \left[\frac{b_{2j} a_j}{(1 - a_j)} \right] \quad (10)$$

$$C_{3j} = - \left[T_{sp} \left(\frac{b_{2j}}{(1 - a_j)} + 1 \right) \right] - b_{3j} \quad (11)$$

5. System performance

The performance of the plant can be defined as the ratio of the distillate product rate to the rate of steam supplied to the plant. Another way to define the performance is to estimate how much kg of water can be produced by the input of 540 k cal to brine heater or to the first effect.

$$PR = (D_N / W_s); \text{ This ratio is dimensionless} \quad (12)$$

The specific heat consumption (q) is defined as being the ratio between the heat flux injected to the brine through brine heater and the distillate output

$$q = W_s * \lambda_s / D_N; \quad (13)$$

6. Computer code structure and solution procedure

The mathematical model for a steady state simulation, as described above, is used to build computer code for performance analysis of MSF desalination systems.

In this code, all the temperature profiles T_{Fj} , T_{Bj} , and T_{Dj} , $j=1, \dots, N$ are initialized so the various properties, heat transfer coefficients and temperature losses can be calculated and, as a result, all the model equations become linear. A TDM is developed consisting of linear equations correlating each combination of three successive temperatures T_{Fj} , T_{Fj-1} , and T_{Fj+1} . By solving these equations simultaneously, an updated profile of T_{Fj} is obtained which is used through the heat transfer equation to update the T_{Dj} profile.

The convergence criterion used is:

$$\sum_{j=1}^N [T_{Bj}^{i+1} - T_{Bj}^i]^2 \leq 0.00001 \times N$$

Where i is the iteration index.

Figure 3 gives the flow chart of the computer code used for steady state simulation of the MSF desalination systems. The excision steps are as following:

1. Initialize all the variables, temperatures, flow rates and salinity
2. Solve enthalpy balance equations for flashing brine flow rate (B_j)
3. Solve overall mass balance equation for distillate flow rate (D_j).
4. Balance the mass on blow down splitter (relation between F, W, B_N).
5. Balance the overall salt for recycle concentration (C_R).
6. Balance the salt on brine heater.
7. Calculation of the stages temperature losses ($BPE_j, \delta_j, \Delta_j$).
8. Solve the stage heat balance equations simultaneously (matrix equations) for the tube side temperatures and top brine temperature, T_{Fj}, T_{B0} .
9. Solve the heat transfer equations simultaneously for updating distilled temperature profiles (T_{Dj}).
10. Solve equilibrium equations iteratively for a new temperature profile of flashing brine (T_{Bj}).
11. Test for convergence.
12. Use the converged values to obtain the other variables (W_s, q, PR).

7. Model Validation

Table 1 compares the temperatures of the flashing brine (T_{Bj}), distillate (T_{Dj}), and recirculating brine (T_{Fj}) as well as the flash pressures (P_j) in 24 flash stages of actual data of plant in Kuwait and data obtained by [Ref 4] with values predicted by developed code. Table 2 compares actual and predicted values of the recirculating brine temperature entering the brine heater (T_{F1}), temperature of the final distillate produced (T_{DN}) and temperature of final flash stage (T_{BN}) as well as the flow rate of distillate produced (D_N), blow down (B_N), and steam to brine heater (W_s). In addition, this table shows the predicted and actual performance ratio, which is the ratio of distillate produced to steam consumed. While Table 3 shows the profiles of temperature and distillate flow rate presented by [Ref 2] as compared with the predicted values. These two tables show the superiority of the current predictions over the available predicted data as compared with the real plant data.

Table1: Comparison of predicted values with actual plant data and [Ref.4].

Flash stage no.	$T_{B(j)} [^{\circ}C]$			$T_{D(j)} [^{\circ}C]$			$T_{F(j)} [^{\circ}C]$			$P_{(j)} [Bar]$		
	Ref.4	Real data	Current study	Ref.4	Real data	Current study	Ref.4	Real data	Current study	Ref.4	Real data	Current study
1	88.36	88.90	88.23	87.16	87.70	87.27	82.22	83.20	85.02	0.63	0.66	0.63
3	83.09	84.40	84.17	81.89	83.20	83.14	76.97	78.80	80.69	0.52	0.55	0.54
5	77.83	79.60	79.99	76.63	78.40	78.95	71.77	74.00	76.49	0.42	0.45	0.45
7	72.62	75.00	75.77	71.42	73.80	74.73	66.68	69.40	72.27	0.33	0.38	0.38
9	67.52	70.50	71.53	66.32	69.30	70.49	61.75	64.80	68.02	0.27	0.31	0.32
11	62.59	66.20	67.29	61.39	65.00	66.23	57.01	60.50	63.77	0.22	0.26	0.26
13	57.91	61.90	63.05	56.61	60.60	61.98	52.56	56.20	59.52	0.17	0.21	0.22
15	53.58	57.70	58.84	52.18	56.30	57.73	48.47	52.00	55.29	0.14	0.17	0.18
17	49.55	53.60	54.66	48.15	52.20	53.51	44.70	47.90	51.10	0.12	0.14	0.14
19	45.96	49.70	50.53	44.36	48.10	49.33	41.36	44.00	46.95	0.10	0.12	0.12
21	42.82	45.90	46.61	41.10	44.20	45.32	38.44	40.34	42.87	0.08	0.10	0.10
23	40.11	42.60	43.01	38.21	40.70	41.65	34.23	35.30	38.43	0.07	0.08	0.08
24	38.44	40.50	40.75	36.54	38.60	39.35	32.22	32.22	35.57	0.06	0.07	0.07

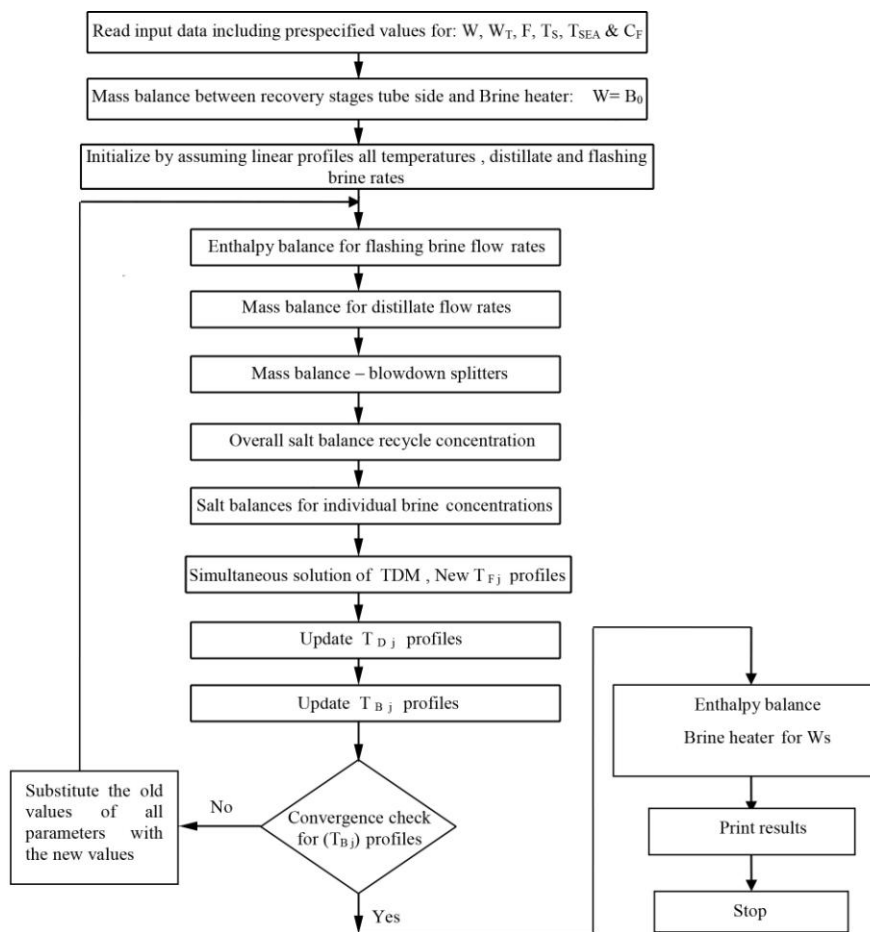


Fig. 3: Flow chart of the computer code.

Table 2: Comparison of predicted performance variables with design data and Ref.4.

Performance variables	Unit	Ref.4	Real data	Current study
$T_{F(1)}$	$^{\circ}C$	84.43	84.89	85.00
$T_{D(N)}$	$^{\circ}C$	36.54	38.60	39.46
$T_{B(N)}$	$^{\circ}C$	38.44	40.50	40.50
$D_{(N)}$	T/min	19.33	18.80	18.69
$B_{(N)}$	T/min	29.43	29.96	29.93
W_s	T/min	2.50	2.35	2.36
Performance Ratio	kg/540 kcal	7.76	8.00	7.93

Table 3: Comparison of predicted performance variables with design data and Ref.2.

Flash stage no.	$T_{B(i)} [^{\circ}C]$		$T_{D(i)} [^{\circ}C]$		$T_{F(i)} [^{\circ}C]$		$D_{(i)} [T/hr]$	
	Ref .2	Current study	Ref .2	Current study	Ref .2	Current study	Ref .2	Current study
0	89.74	89.32	0.00	0.00	0.00	0.00	0.0000	0.00
1	86.89	86.31	85.75	85.69	83.33	83.07	59.40	61.62
2	84.01	83.45	82.87	82.82	80.41	80.19	118.70	119.63
3	81.08	80.57	79.95	79.93	77.44	77.28	178.40	177.50
4	78.11	77.67	76.97	77.02	74.43	74.36	238.50	235.19
5	75.09	74.76	73.94	74.10	71.37	71.43	298.90	292.62
6	72.04	71.84	70.88	71.17	68.28	68.49	359.50	349.72
7	68.95	68.92	67.78	68.23	65.16	65.54	420.10	406.44
8	65.84	65.99	64.65	65.29	62.01	62.60	480.60	462.70
9	62.70	63.07	61.49	62.33	58.84	59.65	541.00	518.43
10	59.55	60.15	58.32	59.39	55.65	56.71	601.00	573.57
11	56.39	57.25	55.13	56.45	52.46	53.78	660.60	628.03
12	53.24	54.36	51.93	53.51	49.27	50.86	719.70	681.73
13	50.09	51.50	48.74	50.60	46.09	47.96	778.00	734.56
14	47.28	48.45	45.87	47.51	44.06	45.08	829.60	790.28
15	44.42	45.30	42.95	44.28	41.10	41.82	881.60	847.59
16	41.51	42.07	39.98	40.97	38.07	38.44	934.10	905.40

8. Case study

In this case study the performance calculations is solved using the developed computer code. The design data used for this purpose belong to the North Benghazi (Libya) MSF desalination plant .The capacity of the plant is 6000 ton/day and the total number of stages are 20, 17 in recovery section and 3 in rejection section . The design operational and dimensional data are listed in Tables 4 and 5. The heat balance diagram of the plant is shown in Figure 4.

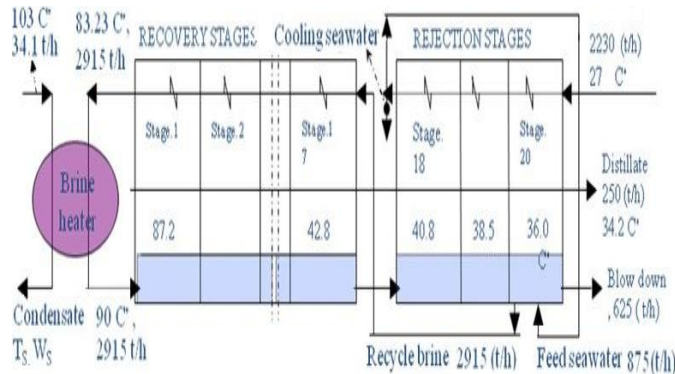


Fig.4: Heat balance diagram for multistage flash desalination plant presented by contractor.

To demonstrate the capability of the code for predicting the performance parameters, the seawater feed flow rate (W_T), the recycle stream flow rate (W) and the steam temperature (T_s) are input to the code. On the basis of these information the model is run to calculate the plant productivity together with the profiles of temperatures and flow rates of in all the stages of the unit . The main parameter used to quantify the process performance is the ratio between the distillate product and the steam flow rate. The results of this calculation are reported in Table 6.

Table 4: Design and operational data of North Benghazi desalination plant [5].

Process variables	Units	Specification
Sea water inlet temperature	$^{\circ}C$	27
Distillate produce	T/h	250
Steam flow rate to brine heater	T/h	34.1
Recycle brine flow rate	T/h	2915
Sea water flow rate	T/h	2230
Make-up flow rate	T/h	875
Blowdown flow rate	T/h	625
Steam temperature to brine heater	$^{\circ}C$	103
Top brine temperature	$^{\circ}C$	90

Table 5: Design and dimensional details of North Benghazi desalination plant [5].

Variables	Unit	Brine heater	Heat recovery section	Heat rejection section
No. of tubes		1535	1520	1433
Tube (D_i)	mm	18	18	16
Tube (D_o)	mm	20	20	18
Area	m^2	842	840	703.33
(U_D)	$kcal/m^2 \cdot c /hr$	1700	2453	2100
F. F	$(kcal/m^2 \cdot c /hr)^{-1}$	3.5819	1.667	1.945
V of brine	m/s	2.0	2.0	2.1

9. Comparison between actual and predicted results

To evaluate the accuracy of the predicted data presented in Table 6, Table 7 is constructed from the manufacture data and predicted values. The comparison is made for the recirculating brine temperature entering the brine heater (T_{F1}), temperature of the final distillate produced (T_{DN}), final brine temperature (T_{BN}) and the top brine temperature (T_{B0}), as well as the flow rate of distillate produced (D_N), blow down (B_N) and steam to brine heater (W_S). In addition , this table shows the performance ratio and energy necessary to produce 1 kg of distillate (q). Inspection of data presented in Table 7 reveals that the predicted values are very close to the referenced values.

Table 6. Output results for the MSF desalination plant

Stage No	B ,T/h	D , T/h	C _B %	T _{Fj} °C	T _{Dj} °C	T _{Bj} °C	p, bar	V, m/s
0	2915	0	0.0544			91.04	0.70	2.060
1	2901.99	13.00	0.0546	84.52	87.56	88.35	0.63	2.081
2	2888.68	26.32	0.0549	81.70	84.89	85.67	0.57	2.077
3	2875.40	39.61	0.0551	78.99	82.19	82.97	0.51	2.074
4	2862.20	52.88	0.0554	76.26	79.48	80.25	0.45	2.070
5	2848.88	66.11	0.0557	73.52	76.76	77.52	0.41	2.067
6	2835.70	79.30	0.0559	70.76	74.02	74.78	0.36	2.064
11	2770.81	144.20	0.0572	56.89	60.18	60.94	0.19	2.049
12	2758.20	156.88	0.0575	54.11	57.40	58.17	0.17	2.046
13	2745.54	169.46	0.0578	51.33	54.61	55.40	0.15	2.043
14	2733.09	181.91	0.0580	48.56	51.83	52.63	0.13	2.041
15	2720.78	194.22	0.0583	45.80	49.06	49.88	0.11	2.038
16	2708.62	206.40	0.0585	43.04	46.30	47.14	0.10	2.036
17	2703.58	211.43	0.0587	40.30	45.04	45.99	0.095	2.033
18	2703.58	228.70	0.0589	37.54	41.21	42.05	0.079	2.104
19	2674.60	240.40	0.0593	34.46	38.44	39.35	0.069	2.102
20	2661.64	254.47	0.0596	30.93	35.42	36.22	0.058	2.100

Table 7: Comparison between actual and predicted principal operating parameters.

Operating parameters	Unit	Contractor's design data	Predicted	Error %
T _{F1}	°C	83.23	84.52	1.55
T _{DN}	°C	34.20	35.42	3.56
T _{BN}	°C	36	36.22	0.61
T _{B0}	°C	90	91.04	1.15
T _m (make up)	°C	37	37.65	1.73
D _N	T/h	250	254.47	1.78
B _D	T/h	625	621.64	0.537
W _S	T/h	34.10	35.67	4.60
Performance ratio	kg/540 kcal	7.33	7.17	2.18
Specific heat consumption	kcal/kg ofdistillate	75.5	75.28	0.30

10. Conclusion

The following conclusions are subtracted from the present study:

1. The developed model can be used adequately to analyze the MSF water desalination process at steady state operation conditions.
2. The developed computer code can be used adequately to perform the performance analysis of MSF desalination plants by calculating the plant productivity together with profiles of temperatures and flow rates in all stages of the unit.
3. The present code is valid when compared with commercial softwares used for the same purpose.
4. North Benghazi desalination plant was used as a case study, and good agreement was found when comparing the predicted data with the plant design data.

References

[1] A. M. Helal, M.S. Medani, M. A. Soliman, and J. R. Flowers. (1986). A tridiagonal matrix model for multistage flash desalination plants. *Comput. Chem. Engg.* Vol. 10, 327-34.

[2] Marina Rosso, Angelo Beltarmini, Marco Mazzotti, and Massimo Morbidelli. (1996). Modeling multistage flash desalination plants. *Desalination* Vol.108, 365- 374.

[3] A. Husain, A. Woldai, Al – Radif, A. Kesou, R. Borsani, and P. B. Dshphandey. (1994). Modelling and simulation of a multistage flash desalination plant. *Desalination* Vol. 97, 555- 586.

[4] Khawlaabduhmohsen Al – shayji. (1998). Modeling, Simulation, and Optimization of large scale commercial desalination plants. PhD Thesis, Virginia Polytechnic Institute and State University, Virginia.

[5] Operating manual of MSF desalination plant at north-Benghazi station.

APENDIX: Nomenclature

Symbol	Description
a _{1j} , a _{2j} , a _{2j}	Temporary constants for stage j
b _{1j} , b _{2j} , b _{3j}	Temporary variables
B _D	Blowdown mass flow rate
B _i	Flashing brine mass flow rate leaving stage j
B ₀	Flashing brine mass flow rate Leaving the brine heater
BPE _j	Boiling point elevation at stage j
c _{1j} , c _{2j} , c _{3j}	Temporary constants at the conditions of stage j
C _{Bj}	Salt concentration in the flashing brine leaving stage j
C _{B0}	Salt concentration in the flashing brine leaving the brine heater
C _F	Feed seawater salt concentration
C _R	Salt concentration in the cooling brine to the recovery section
C _W	Rejected sea water mass flow rate
D _i	Distillate flow rate leaving stage j
D _N	Plant productivity
F	Make-up seawater mass flow rate
N	Total number of stages, N=NR+NJ
NR	Number of stages in the heat recovery section
NJ	Number of stages in the heat rejection section
P _j	Pressure at stage j
PR	Performance ratio of the plant, PR = DN/Ws
T _{B0}	Temperature of flashing brine leaving the brine heater
T _{Bi}	Temperature of flashing brine leaving stage j
T _{Di}	Temperature of distillate leaving stage j
T _{Fj}	Temperature of cooling brine leaving stage j
T _m	Temperature of make up seawater flow rate
T _{SEA}	Seawater temperature
T _S	Steam temperature
W	Recirculating brine mass flow rate To the heat recovery section
W _S	Steam mass flow rate
W _T	Sea water mass flow rate to the heat rejection section

Greek letters

Δ _j	Temperature loss at stage j
δ _i	Non equilibrium allowance at stage j
λ _s	Latent heat of steam to brine heater

Economic Evaluation of Mixed C₄s Upgrading Processes. (Raslanuf Ethylene Plant as a Case Study)

Isam A. B. Salem

University of Benghazi, Benghazi, Libya
Tel.: +0-218-91-3799271; e-mail: isam.salem@uob.edu.ly

ABSTRACT

Reducing the operating cost (opex) is a method implemented by Ethylene producers to keep ethylene prices from expensive feedstock more competitive in comparison with cheaper feed stocks like ethane. Alternatively economics maybe improved by upgrading the mixed C₄ stream which is produced from ethylene plant and contains valuable unsaturated C₄s such as butadiene, isobutylene, butene-1, and butene-2. There are different processing options available to recover these components or turn them into final products. These processing options or routes are combination of different chemical processes such as Total hydrogenation, Butadiene extraction, MTBE production from butylenes, Butane-1 recovery and other processes. Several upgrading options have been proposed and evaluated for Raslanuf ethylene plant c₄ feed of about 130000 tonne/y. Internal rate of return IRR, payback time or period PBP, and the net present value NPV, all have been estimated for options which can be implemented at the site; butadiene extraction and metathesis. Because base case results were not definitive, sensitivity analysis was performed. The parameters investigated are sales prices; feed cost, construction time and total investment. The results suggest butadiene extraction is the best processing option for processing Raslanuf mixed C₄ stream.

Keywords: Ethylene, the upgrading of mixed C₄, butadiene extraction, internal rate of return, sensitivity analysis.

1. Introduction.

Ethylene is produced from steam cracker with different feeds stocks like ethane, LPG, gas oil and naphtha.

The gross profit margin, which is determined mainly by the difference between the products revenues and feedstock costs, made the ethylene produced by ethane (from natural gas) more profitable and competitive in comparison with ethylene from naphtha. Steam crackers, which depend on naphtha, faced a huge challenge in the ethylene market, and the need to reduce the cost of production issue appeared among petrochemical analysts.

Recent decline in crude prices have eroded much the massive cost advantage previously enjoyed by ethane over naphtha, This issue will not remain forever in the volatile oil markets, and many are forecasting oil prices to climb up by the end of 2016 [1]. The permanent solution to tackle the issue of higher feedstock and higher operating costs is to find the most economical upgrading route for one of the main products of ethylene such as pyrolysis gasoline (Py Gas) or the Mixed C₄ hydrocarbons.

This can be accomplished by converting relatively low valuable product to more valuable products. The title "mixed C₄ upgrading routes or schemes" appeared in many articles [2] and some textbooks [3].

Raslanuf complex (Rasco) ethylene plant with capacity (330000 ton/year) faced this challenge because its feedstock was naphtha produced in the nearby Rasco refinery. It is considered as an old plant that needs upgrading.

The present paper investigated the different available technologies (routes) to upgrade locally mixed c₄ produced by Rasco to more valuable products. The data used in this case study is primarily products capacity data obtained from previous published paper and website of the company [1,11].

The final choice of the best scheme was based on techno-economic profitability analysis using different parameters and taking into consideration the age of the plant, site constraints and its sensitivity to market fluctuations.

2. Processing routes or schemes available

Six upgrading schemes are identified and as follows:

2.1. Total Hydrogenation

Total hydrogenation process provides saturation of olefin, diolefin, and acetylene compounds in C₄ stream. This process hydrogenates unsaturated hydrocarbons inside a single fixed-bed reactor system at mild operating conditions.

Product from the unit is mainly LPG, which can be recycled back to the ethylene plant to the cracking heater. The process called cocracking. The option of recycling back LPG will reduce naphtha feed and reduce the operating costs indirectly. It was not considered in this study because the prices of naphtha and LPG are almost the same [4].

2.2. Butadiene extraction

A typical butadiene extraction process consists of two stages of extractive distillation (Extractive distillation is necessary because the similarities in volatilities between the products in the C₄ stream).

Products from this process are mainly a raffinate containing butenes from the first stage overhead and a crude butadiene product from the second stage. The solvent, for example in BASF butadiene process is N-methylpyrrolidinone (NMP).

2.3. Metathesis

Metathesis utilizes two chemical reactions to combine 2-butenes with ethylene to produce propylene. The second reaction isomerizes butene-1 to butene-2 as the latter is consumed in the metathesis reaction. Economics suggest that it can be also selectively hydrogenated to produce additional butylenes feed for the metathesis reactor. The selective hydrogenation unit offers a highly selective catalyst for the hydrogenation of butadiene to butenes [5,6].

2.4. MTBE

Methyl tertiary butyl ether (MTBE) is an oxygenate used worldwide as gasoline octane booster, although the use of MTBE as octane booster has been declining due to problems with groundwater contamination. New type of octane booster ETBE is used instead. MTBE process converts isobutylene by using of methanol [6]

2.5. Other processes.

Other process schemes or routes are available and it is developed through the combination of the previously mentioned main routes.

3. Economic evaluation for the proposed Mixed C4 upgrading schemes.

Before starting the economic evaluation by subjecting the different process to the different economic analysis methods, some consideration should be taken which will lead to dropping some options due to local condition or previous studies:

- 1- Option1 which is producing LPG by total hydrogenation scheme will be dropped from the evaluation for the following reasons:
 - LPG is produced in the nearby refinery and can be utilized
 - Previous studies showed clearly that the processing route1(total hydrogenation) has the least profit[2].
- 2- Options 4 and 5 were dropped from the economic evaluation because of the following:
 - Raw materials for these options are not available on the site.
 - Methanol procurement will be through several sea shipments per year thus increasing feed and operating costs.

Table 1:Material balance

t/y		Option 2	Option 3
Raw materials	Mixed C ₄	130000	130000
	Ethylene	–	42000
	Hydrogen	–	2800
Products	Propylene	–	111872
	Butadiene	65000	–
	Raffinate	65000	62928

Therefore, only two process options (2 and 3) were subjected to economic evaluation .Table 1 illustrates the material balance required to carry out the economic evaluation for the base case study.

The feed for both schemes is 130000 t/y of mixed C4, also the products distribution in tons per year (t/y) are given in table 1. International sales prices of the different raw materials and products are for the August of year 2015 except for hydrogen price where the method of its equivalent fuel to calculate the price was used, as shown in Table 2. The Equipment costs are called the (inside battery limit) ISBL cost which is essential figure in the calculations was taken from old data found in previous studies. Escalation method was used to estimate the present value and location correction factor also used [7].

Table 2:Products and raw materials sales prices Aug.2015.

Raw material	\$/T
Mixed C4	460
Ethylene	1100
Hydrogen	1000
Products	\$/T
propylene	1000
Raffinate	411
Butadiene	900

The bases of the economic evaluation are given in Table3.Us Microsoft Excel® was used to calculate the annual cash flow, net present value NPV and IRR. The calculated economic parameters are presented in Table 4 for the two selected options. Payback

period PBP was found for each case by calculating the cumulative cash flow column divided by plant lifetime[8].

Table 3:The basis of economic evaluation

Parameter	Value
Upgrading plant cap.	130000 t/y
Working days	330days
Plant life time	20 years
Plant construction time	2 years
On stream day	50% 3 rd year, 100% (4-40)
Taxes	10%
Year of starting taxation	6 th year
Maintenance	3% ISBL
Plant overhead	2% fixed investment

4. Discussion and results

Table 4 summarizes the results obtained for the two proposed processes. The economic indicators showed different rankings for the two options and both are economically feasible.

Table 4:The economic evaluation

option	2 nd	3 rd
Feed costs MM/y		
Mixed C 4	59.8	59.8
Hydrogen	–	2.8
Ethylene	–	46.2
Total feed cost MM/y	59.8	108.8
Product sales MM/y		
butadiene	58.5	–
Propylene	–	109.635
Raffinate	26.715	25.86
Total MM/y	85.215	135.495
Gross margin MM/y	25.415	26.695
Total utility cost MM/y	5.4	0.74
Total investment MM/y	32.2	36.59
Simple pay back PBP	2.14	2.32
NPV \$ MM	76.4	79.3
IRR %	54	51

Option 2, which is the butadiene extraction, has the highest IRR (54%) and PBP of (2.14years) compared to 51% and 2.3 years for option 3-metathesis process. Based on the above results, which show very tight margin between the economic parameters, there is a need to see another method to evaluate the projects and guarantee the best selection.

5. Sensitivity analysis.

5.1. Importance of sensitivity analysis.

A sensitivity analysis is a way of investigating the effects of uncertainties in the different forecasts, which are due to the volatile market on the viability of a project. To perform this analysis the total investment and cash flows are calculated using what are considered the most probable values for the various factors; this establishes the base case for analysis. The cash flows and associated economic indicators are then calculated assuming a range of error for each of the factors that may affect profitability as measured by changes in NPV and IRR from base case. These are sales price, raw materials cost, total investment and construction time as shown in Table 5. The results of this analysis are depicted using tornado charts.

Table 5:Sensitivity analysis parameters

Factor	Percent of base value
Sales price	-20 to +20
Feed cost	-10 to +30
Total investment	-20 to +50
Construction time	-6 months to +2years

5.2. Sensitivity analysis results with tornado charts.

A tornado diagram is a special type of bar chart which provides graphical representation of a comparative sensitivity analysis. It is a great tool for the decision makers to give them some insight into the uncertainties and their potential impact on the project under investigation. The x-axis of a tornado diagram is the value of the primary objective function e.g. (NPV). Parallel bars represent the objective function range from base case for each the sensitivity parameters. Each sensitivity analysis parameter in the model has its own bar, and the width of each bar shows how much impact that factor can have on NPV when varied through a range suggested for the study. In other words, it is a method to evaluate the risk associated with the project due to uncertainty in parameters, which affects the outcome [9].

5.3. Sensitivity analysis for 2nd option.

The sensitivity analysis has been performed for the various specified ranges of the input variable parameters depicted in Table 5.

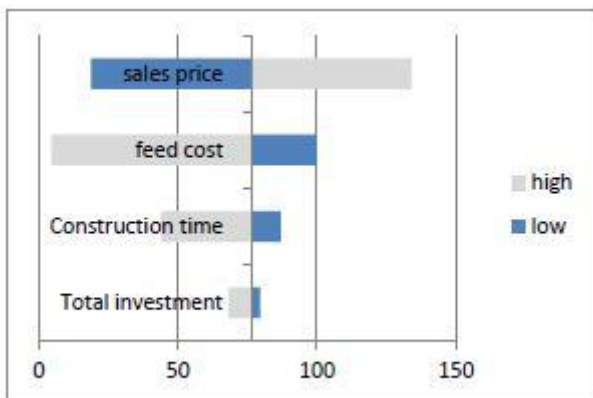


Fig. 1:Tornado chart for 2ndoptionwith NPV base 76 MM\$.

The output results, Figs (1 and 2) are arranged on tornado chart downward from largest width down to smallest width, and presented as tornado charts for the NPV and IRR.

- The factors associated with maximum change on NPV are the sales price, feed cost and to smaller extent is the construction time. The high feed cost and the low sales price may decrease NPV to a value less than the project investment which made the project unfeasible

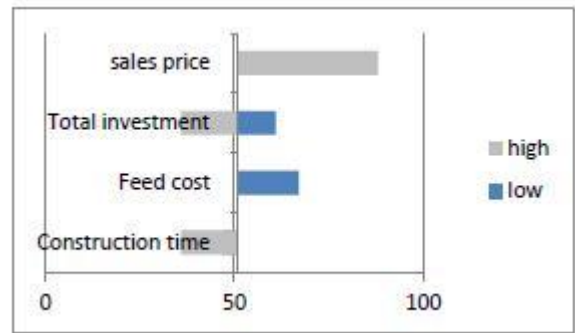


Fig. 2: Tornado chart for 2nd option with IRR base 54%.

- The factors associated with maximum change on IRR are the sales price, feed cost and to smaller extent is the construction time.
- It is clear that the sales price and feed cost are the most influential input parameter for both NPV and IRR, also it could be concluded even with the change in these parameters the 2nd option still feasible and can withstand the volatile market, which is simulated, by these changes.

5.4. Sensitivity analysis for the 3rd option.

The sensitivity analysis has been performed for the various specified ranges of the input variable parameters shown in Table 5.



Fig. 3:Tornado chart for 3rd option with NPV base 79 MM\$.

The output results, Figs (3 and 4) are arranged on tornado chart downward from largest width down to smallest width, and presented as tornado charts for the NPV and IRR and here are the results

- The factors associated with maximum change on NPV are the sales price, feed cost and to smaller extent is the construction time. The high feed cost or the low sales prices can make the project unfeasible
- The factors associated with maximum change on IRR are the sales price, feed cost and to smaller extent is the construction time. The parameters sales price and feed cost turned the NPV to negative, because of this, the IRR was not calculated, and the change in the magnitude was not shown on tornado chart either.

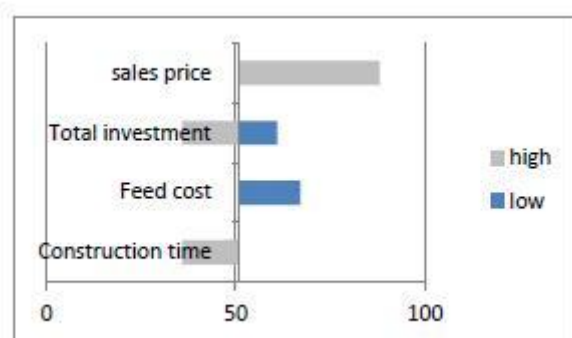


Fig. 4: Tornado chart for 3rd option with IRR base 51%.

6. Conclusions

In this study, four schemes regarding the upgrading of Mixed C₄ stream from Raslanuf ethylene plant were studied. The cash flow method was used for the economic evaluation. The parameters, which were used, are net present value NPV, internal rate of return; IRR and simple payback period, all are evaluated for each case and the conclusion as follows:

- The 1st option was dropped because it will lead production of LPG, which is already available at Rasco refinery and can be used to reduce the consumption of naphtha feed to ethylene plant. This method were studied before in many literatures and was shown to be the least profitable [2].
- The 4th option and the other process, which depend on the use of external raw material (Methanol), was also dropped because this study will focus on the raw materials that already available on site only.
- The two studied options (2 and 3) are profitable. Similar results have been reported [2, 4, and 10].
- The option that has the most attractive economic indicators is 2nd option. Some of reasons behind this are the relatively low total investment in comparison to option 3. The feature that it consumes Mixed C₄ feed only, gives it advantage over option 3, which consumes ethylene and small amount of hydrogen, which are considered as highly expensive raw materials.
- Sensitivity analysis was carried out because the margins between the economic parameters were tight to determine the most influential factor on the projects profitability as measured by NPV and IRR.
- Sensitivity analysis showed that the most influential parameters that affect the project are sales price and the feed cost.
- Tornado charts were used to illustrate the effect of each input parameter on the different economic indicators used in this study. These charts showed that option 2 is less risky in comparison to option 3 and can withstand the expected global changes in prices better than option 3.

References

- [1] Ahmed M. Eltief, (2014), Co – Cracking of Mixed C₄, S and LPG with Naphtha in Raslanuf Ethylene Plant – Libya <https://www.linkedin.com/pulse/20140907080129-178610257-co-cracking-of-mixed-c4-s-and-lpg-with-naphtha-in-ras-lanuf-ethylene-plant-libya>.
- [2] Coulson & Richardson's, (2005) chemical engineering series volume 6, fourth edition.
- [3] Cuckoo James (2015), weaker oil price erodes ethane cost advantage over naphtha, ICIS article.
- [4] Donald L. Burdick, William L. Jeffler, (2001) petrochemicals in nontechnical language, third edition.
- [5] Gavin Towler, Ray Sinnott, (2008), Chemical Engineering Design Principles, Practice and Economics of Plant and Process Design, Elsevier.
- [6] Indra Deo Mall, (2016), Petrochemical Process Technology, First edition.
- [7] Robert A Meyers, (2005), Handbook of petrochemicals production processes, McGraw-Hill, 3rd edition.
- [8] Sami Matar, Lewis Hatch, (2000), Chemistry of Petrochemical Processes, second edition.
- [9] Seham A El- Temtamy, Tahani S. Gendy, (2014), Economic evaluation and sensitivity analysis of some fuel oil upgrading processes, Egyptian Journal of Petroleum.
- [10] Stacia M Edwards, Stephen J Stanley and Margaret M Shreehan, (1998), Relative economics of mixed C₄ processing routes, the petroleum technology magazine PTQ
- [11] Raslanuf oil and gas processing company, <http://www.raslanuf.ly/ethylene-plant-%28en%29.aspx>

A comparative study for the effects of synthetic diesel fuels on the performance and emissions of a single cylinder DI diesel engine

Mansour N. Elhemri ^a*, Iman K. Reksowardojo ^b, Kanit Wattanavichien ^c, and Wiranto Arismunandar^d

^a Faculty of Engineering, University of Benghazi, Benghazi, Libya.

^{a, b, d} Combustion Engines and Propulsion Systems Laboratory, Faculty of Mechanical and Aerospace Engineering, Institute Technology Bandung, Jl. Ganesa 10 Bandung 40132, Indonesia.

^c Associate Professor, Mechanical Engineering Department, Faculty of Engineering, Chulalongkorn University, Phaya-Thai Road, Patumwan, Bangkok 10330, Thailand.

* Corresponding author: Tel.: +218925126026; e-mail: mansour.nagib.elhemri@gmail.com

ABSTRACT

The high cost of crude oil, the volatility of the international energy market, the nation energy supply security and the negative environmental impacts have been significantly stimulating the use of alternative fuel in engine applications. The production process of waste cooking oil and waste plastic to diesel-range paraffinic compositions was appropriately proposed according to the conditions of the socioeconomic situations. Two alternative synthetic diesel fuels from waste cooking oil and from waste plastic were successfully manufactured by Biomass R&D Centre of Chulalongkorn University, Saraburi, and had been used in this study. Pyrolysis (thermal cracking) process was implemented to break the long chain hydrocarbons, which is the main composition of waste plastics and waste cooking oil, to diesel range hydrocarbons. The main target of this research is to evaluate the influence of using two synthetic diesels and palm cooking oil biodiesel (palm methyl ester) on the performance, and emissions of a direct-injection single cylinder diesel engine comparing with conventional diesel fuel (CD) as base line. Test bench experiments (constant speed steady state) were conducted with a single cylinder DI CI engine at 1400, 1700 and 2100 rpm, along selected part load. The acquired data was a comparative analysis dealt with: brake specific fuel consumption, brake specific energy consumption, brake thermal efficiency, and exhaust emissions. The knowledge of these comparative results on engine performance obtained in this research can be used to develop high performance green fuels in a near future. The results provided a realistic experimental investigation in terms of using such alternative diesel fuels on diesel engines in Southeast Asian countries.

Keywords: Direct Injection Diesel Engine, Synthetic Diesel, Waste Plastic, Waste Cooking Oil, Performance, Emissions.

1. Introduction

Compression ignition engines (CI engine, diesel engines) have long been the dominant and workhorse engines of the industrial applications, favored for the exceptional fuel economy, which leads to higher thermal efficiency, and ability to provide power under a wide range of conditions. Therefore, diesel engines are widely used for transport and agricultural machinery in many regions of the world [1]. Despite of their advantages, they emit high levels of exhaust emissions (i.e., NO_x and smoke) which significantly contribute to the environmental pollutions and health issues [2].

According to British Petroleum (BP), population and income growth are the key drivers behind growing demand for energy causing the world primary energy consumption to be projected to grow by 1.6% from 2011 to 2030, adding 36% to global consumption by 2030 [3]. Currently, a large portion of the world's energy needs to be met by traditional fossil fuels. Due to depletion and higher cost of petroleum-based fuels beside the wide awareness of the environmental protection, researchers, globally, look for alternate fuels [4]. Recently, waste to energy is the trend in the selection of alternate fuels. Unconventional (or nonpetroleum derived) diesel fuels and synthetic fuels such as biodiesel from used cooking oil, and diesel fuel from plastics etc., are some of the alternative diesel fuels for the CI engines. Likely, such alternative diesel fuels are becoming major issues in the consciousness of oil importing countries [5, 6].

Biodiesel, which is commercially produced from virgin vegetable oils, has been accepted as a suitable alternate to diesel fuel, and it has become in recent years a subject for debate around the world as well as in the Southeast Asian countries in order to reduce the dependency on foreign oil [7]. However, the main limiting factor for the market diffusion of biodiesel is the high economic cost of production compared to petroleum diesel oil. The major economic factor to consider for the input costs of biodiesel production is the feedstock due to the higher cost of virgin vegetable oil, which is about 80% of the total operating cost [8]. This led to search for feedstock which provides the advantage of the lower cost and sustainability.

Accordingly, due to the production of large quantities of waste

cooking oil, a substantial amount of biodiesel can be produced from which. Therefore, substantial portion of the biodiesel can be replaced by the biodiesel obtained from waste cooking oil [7]. Waste cooking oil (WCO) as a cheap feedstock is considered highly environmentally sustainable since WCO is a waste product from domestic and commercial cooking processes and then recycled to a transportation fuel [9]. In addition, it avoids the conversion of land use for crop production and the import of virgin oil as feedstock.

Typically, four methods to reduce the high viscosity of vegetable oils to enable their use in common diesel engines without operational problems such as engine deposits have been investigated: blending with petrol diesel, pyrolysis, micro emulsification, and transesterification [10]. The two most popular techniques are transesterification and pyrolysis however; the focus has been on the production of bio-diesel via transesterification [11]. Waste cooking oil with long chain of palmitic acid and oleic acid has the potential to be cracked by thermal cracking or catalytic cracking for possible formation of hydrocarbon chain using the pyrolysis technology. To create biodiesel, a fuel with a viscosity closer to diesel, oil can be modified. Thermally cracking, or controlled pyrolysis, of bio-oil decreases its molecular weight and is there by effective in converting oil to a more useable fuel, like biodiesel. Biodiesel via pyrolysis has some advantages against the one, which is produced via the typical transesterification process. Some but not the least are the absence of using alcohols, cleaning water and the very similar properties to the commercial diesel. In addition, the properties of the biodiesel from waste cooking oil would be largely dependent on the physicochemical properties of feedstock [7].

Plastic have become an indispensable part in today's world, due to their light weight, durability, energy efficiency, coupled with a faster rate of production and design flexibility, these plastics are employed in entire gamut of industrial and domestic are as hence plastics have become essential materials and their applications in the industrial field are continually increasing. At the same time, waste plastics have created very serious environmental challenge because of their huge quantities and their disposal problems [12,13,14]. Waste plastics do not biodegrade in landfills, are not easily recycled, and

degrade in quality during the recycling process. Instead of biodegradation, plastics waste goes through thermal treatment and fuel can be derive, by adopting the chemical process such as Pyrolysis can be used to safely convert waste plastics in to hydrocarbon fuels that can be used for transportation [15]. Moreover, both plastics and petroleum derived fuels are hydrocarbons that contain the elements of carbon and hydrogen. The difference between them is that plastic molecules have longer carbon chains than those in LPG, petrol, and diesel fuels. Therefore, it is possible to convert waste plastic into fuels.

Unfortunately, fuels do have different chemical and physical properties compared to fossil diesel fuel have to be considered. Some fuel properties required by the standards. The above fuels' properties affect the whole combustion process and thereby the engine performance and emissions. In contrast to the engine's demand for fuels with defined properties to meet the emission targets.

The motivation of this research is to investigate and compare the effect of different synthetic and alternative diesel fuels to the conventional diesel fuel in terms of their performance and emissions characteristics. These fuels include pyrolysis waste plastics diesel (PWPD) which produced by well-sorted polyethylene (PE) and polypropylene (PP) waste plastics; pyrolysis waste cooking biodiesel (PWCOB) using waste cooking oil as a feedstock; and palm cooking oil biodiesel (Palm methyl ester, FAME BD). The experiments were performed using a single-cylinder, direct-injection diesel engine that is used for general purposes. Comparatively, Thai conventional diesel fuel (CD) was used as a base line.

2. Experiment Setup and Tested Fuels

2.1. Experiment Setup and test method

The schematic diagram of the experimental setup is shown below in Fig.1. A commercial diesel engine, type KUBOTA RT140 was implemented in this experiment. The engine remained unmodified during the whole experiment with all testing fuels. The engine specification is listed in Table 1.

sensor was used for measuring the ambient conditions (pressure, temperature, and relative humidity) of the air in the testing room. The average gravimetric fuel consumption rate was measured by the FC2210 Advanced Fuel Measurement Device (Gravimetric Fuel Gauge). The major emissions of carbon monoxide (CO), carbon dioxide, unburned hydrocarbons (HC) and nitrogen oxides (NOx), were measured with a Portable Exhaust Gas Analyzer type EMS 5002. The diesel smoke evaluator (ETD 020.50) was used along with the diesel smoke tester (ETD 020.00) to indicate the smoke opacity.

The accuracies of the measuring instruments and the EMS 5002 emission analyzer are listed in the Table 2.

Table 1: Kubota engine specifications.

Items	Specification Parameters
Engine Model & Type	Kubota-RT140, Naturally aspirated, Water-cooled, Single cylinder, and 4-cycle DI diesel engine
Cylinder bore × Stroke × Displacement(mm)	97 × 96 × 709
Continuous rated power output (kW/rpm)	9.2/2400
Max. power/engine speed (kW/rpm)	10.3/2400
Max. torque/engine speed (N.m/rpm)	49.0/1600
Compression ratio	18:1
Injection nozzle type	Bosch KBAL type (4 holes nozzle)
Nozzle opening pressure (Bar)	215.75
Injection timing (Deg CA)	18.5° (BTDC)

Table 2: The measuring instruments and EMS 5002 exhaust gas analyzer.

Measurements	Accuracy	Measurement Ranges
HC	±4ppm	0 – 2000 ppm
NO	±25ppm	0 – 5000 ppm
CO	±0.06%	0 – 10%
CO ₂	±0.3%	0 – 20%
O ₂	±0.1%	0 – 25%
Fuel consumption	± 0.4 % full scale	
Speed measuring	±1 rpm	
Temperature	±1°C	

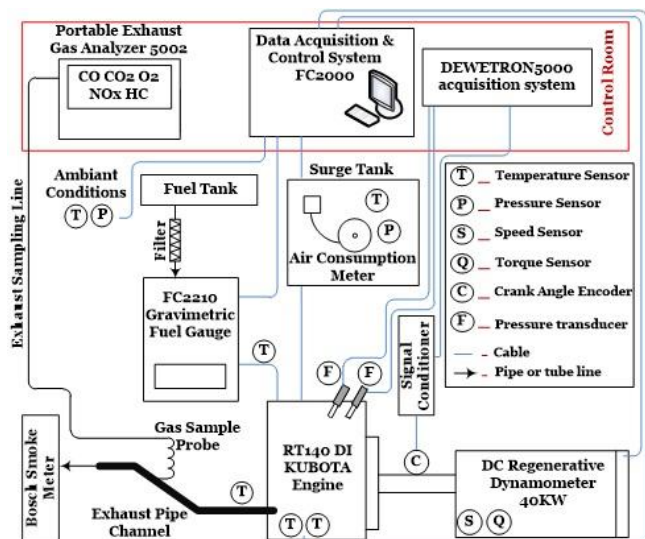


Fig.1: Schematic diagram of the experimental setup.

The engine was coupled to a 40KW DC regenerative dynamometer type (LAK 4180-AA), which fully controlled by FC2000 control system to precisely vary engine speed and torque, and measure other performance parameters. The average air mass flow rate over the entire engine cycle (quasi-steady) measured based on the Air Box method using a TH01-40 air consumption meter. An accurate combined ambient conditions

The test method used in this study was modified-steady-state operating points based on the European Stationary Cycle (ESC) 13-modes (Fig.2)[26]. Points 2, 3, 4, 5, 6, 7, 8, 9, 10, 11, 12 and 13 represent the selected high probably operating points along the ESC driving cycle. Engine speeds A, B, and C was expected to be 1400, 1700, and 2100 rpm, respectively. In addition, the low, medium, and high loads were approximately considered to be 11, 23, 35 N.m, respectively.

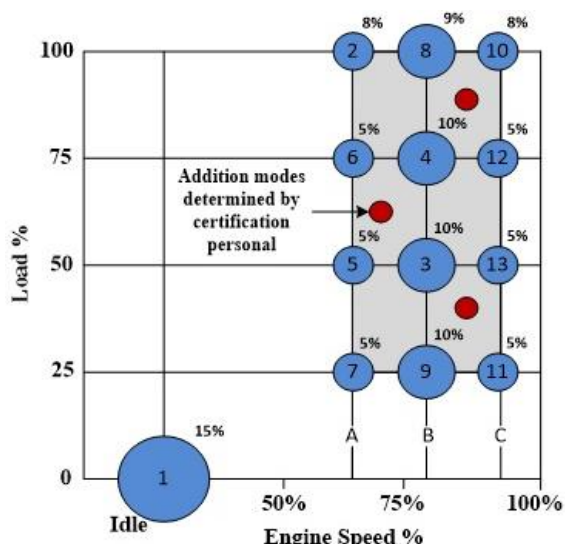


Fig. 2: European stationary cycle (ESC).

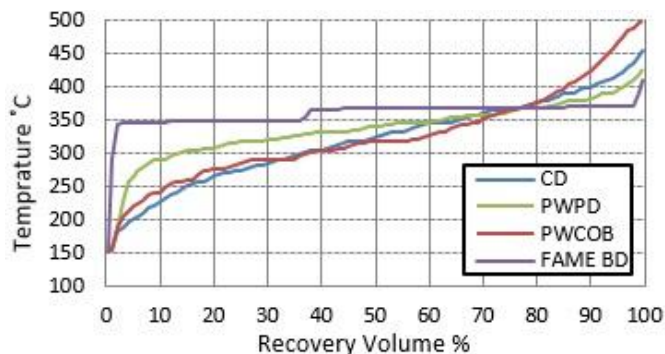


Fig.3: Simulated distillation curves.

Table 4: Elemental percentage analysis.

Contents	CD	PWPB	PWCOD	FAME BD
Naphtha	5.0%	2.35%	2.83%	0.67%
Kerosene	10.0%	1.46%	8.67%	0.18%
Diesel:	(63.0%)	(78.69%)	(66.75%)	(96.15%)
-Light gasoil	50.0%	58.69%	58.5%	35.65%
-Gasoil	13.0%	20.0%	8.25%	60.5%
Long residue	22.0%	17.5%	21.75%	3.0%
Total	100%	100%	100%	100%

2.2. Tested Fuels

The chemical compositions and the properties of interest of the testing fuels are listed in Table 3. In addition, the elemental percent analysis and the simulated distillation curves are provided in Table 4 and Fig.3, respectively as it was direct measured or calculated/predicted from their composition by liquid chromatograph method.

Table 3: Physical properties of the tested fuels.

Property	Test Method	CD ⁽³⁾	PWPB	PWCOD	FAME BD
Density at 15 °C (kg/m ³)	ASTM D1298	827.5	833.3	820.3	876.703
Kinematic viscosity at 40°C (mm ² /s)	ASTM D445	3.74	4.70	2.92	5.36
Heating Value (MJ/kg)	ASTM 04-5865	44.86	45.45	44.48	39.510
CHN elements					
Carbon (%wt)		81.17	76.24	77.14	72.265
Hydrogen (%wt)		15.29	14.08	14.60	13.69
Nitrogen (%wt)		0.066545	0.061415	0.077545	0.412125
API Gravity	ASTM D1298	39.5	38.3	41.0	29.9
Distillation (°C)					
IBP		206.59	250.29	221.61	306.09
T10	ASTM D86	251.70	304.93	265.56	346.29
T50		316.18	329.60	310.46	350.71
T90		375.34	360.01	401.62	352.57
FBP		398.21	376.47	449.71	358.47
Cetane Index ⁽¹⁾	ASTM D4737	56.8	64.9	59.4	N.D(2)
Flash Point (°C)	ASTM D92	81.5	96.0	93.5	180.0
Fire Point (°C)	ASTM D92	85.0	126.0	103.0	185.5

(1) The report on Cetane Index (from Fuel test lab, Division of fuel quality, Department of Energy Business, Ministry of Energy), Thailand.
 (2) FAME BD Cetane Index cannot be determined.
 (3) The conventional diesel fuel is subjected to the Thai policy blended with 5% of palm methyl-ester (PME).

3. Results and Discussions

3.1. Performance Test

3.1.1. Brake Specific Fuel Consumption (BSFC)

Brake specific fuel consumption (BSFC) measures how efficiently an engine is using the fuel supplied to produce work. It is inversely proportional to thermal efficiency and has units of grams per kilowatt-hour (g/kWh). It is also a function of fuel consumption and engine power output. Fig. 4 shows the variations of the BSFC of the test fuels at all engine speeds with respect to engine loads. In general, at all engine speeds, BSFC decreases with increase in the engine load. The main reason for this could be that the percent increase in fuel required to operate the engine is less than the percent increase in brake power due to relatively less portion of the heat losses at higher loads.

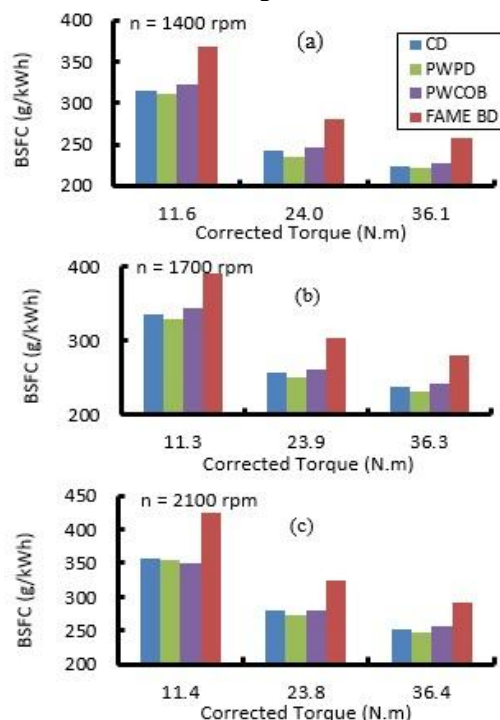


Fig.4: Brake specific fuel consumption.

From Fig.4,BSFC decreases as the load increases for all the fuels. On the total average and in comparing with commercial diesel (CD), brake specific fuel consumption for the pyrolysis waste plastic diesel (PWPB) decreased by 1.52% while increased for pyrolysis waste cooking oil biodiesel (PWCOB) and FAME biodiesel (FAME BD) by 0.94% and 12.65%, respectively. This variation in BSFC mainly attributed to the different amounts of fuel (FC) which is necessary to deliver the same power output at every operating condition. The alterations in the BSFC dominantly due to the consequence of the different heating values of the test fuels (refer to Table 3).

3.1.2. Brake Specific Energy Consumption (BSEC)

The brake specific energy consumption (BSEC) is defined as the energy of fuel needed to produce 1 kWh of brake work. It is an indication of the energy needed to produce the same required power. Fig.5 shows comparisons of BSEC for the test fuels at all operating conditions. As it can be seen from the figure, regardless of engine speed, BSEC decrease with load increase. On average, PWPB shows the best energy economy with a lower BSEC by 0.55% than CD. PWCOB provides similar BSEC which 0.29% higher than CD. The highest BSEC was shown by FAME BD with 2.19% higher than CD. Beside the effect of the heating values of the test fuels on the fuel consumption, the higher kinematic viscosity of FAME BD fuel could also affect its spray characteristics and consequently the whole combustion process and fuel consumption.

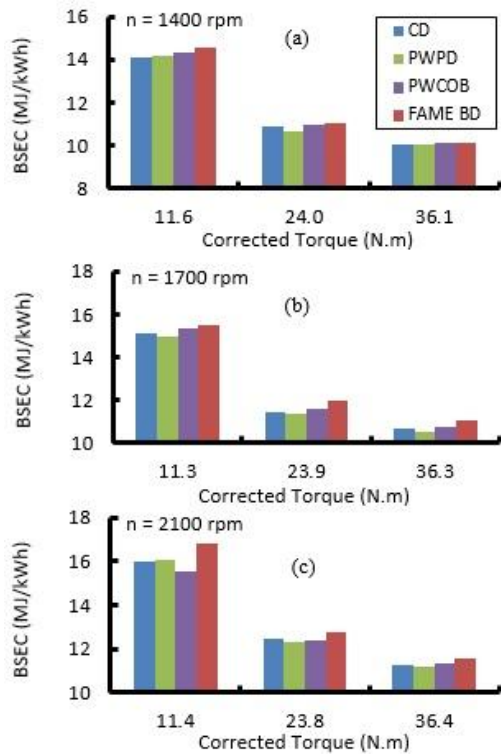


Fig.5:Brake specific energy consumption.

3.1.3. Brake Thermal Efficiency (BTE)

Fig.6 illustrates brake thermal efficiency (BTE) with CD, PWPB, PWCOB, and BD fuels at all engine speeds. Brake thermal efficiency evaluates how efficient the engine transforms the chemical energy of the fuel into useful work. It is determined by dividing the brake power of the engine to the amount of energy input to the system. As expected that for all engine speeds, the brake thermal efficiency was higher in the case of medium and high-load conditions (23 and 35 N.m) compared to

low load condition (11 N.m). This can be explained by that less fuel energy is needed to cover the mechanical losses of the engine when the engine load is increased.

It can be observed from Fig.6 that there is no significant difference in the BTE for PWPB and PWCOB fuels in compare with CD. Averagely, PWPB shows a slightly higher value of BTE by 0.75% while PWCOB gives slightly lower value by 0.37% compared to that of CD at all engine operating conditions. The main reasons are the corresponding higher and lower heating value of PWPB and PWCOB, respectively. The heating value of PWPB is higher by 1.31% and the corresponding heating value of PWCOB is lower by 0.85% than that of CD. The combination of fuel consumption and heating values results in small variations of BTE among the CD, PWPB and PWCOB fuels. On the other hand, FAME BD shows the lowest BTE with a reduction of 2.82% compared to CD. The reduction in thermal efficiency with FAME BD attributed not only to the lower heating value of FAME BD, which is 11.93% less than of that of CD, but also to the higher viscosity. Higher viscosity resulted in poor spray characteristics and air to fuel mixing.

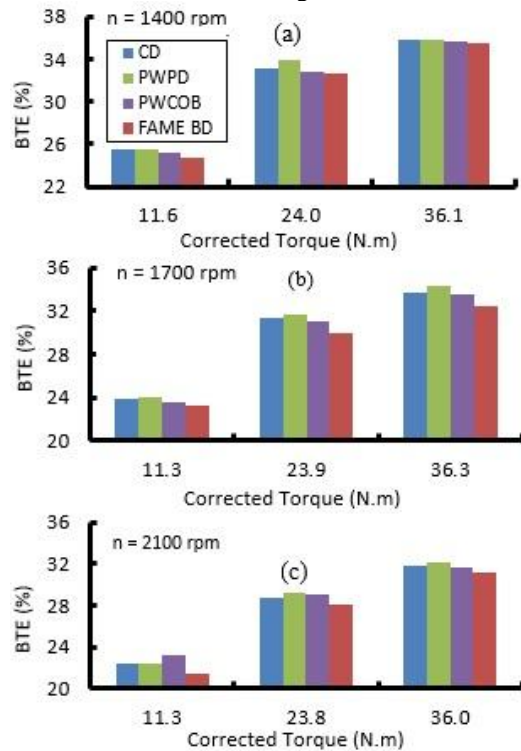


Fig. 6:Brake thermal efficiency.

3.1.4. Exhaust Gas Temperature

Engine exhaust temperature is an important indicator of the cylinder combustion temperature, and it is hence a good parameter in analyzing the exhaust emissions especially for NOx. Furthermore, the exhaust gas temperature is a convenient scale to study the extent of afterburning. The variations of the gases exhaust temperature with the engine speeds and load range for all the test fuels shown in Fig.7.

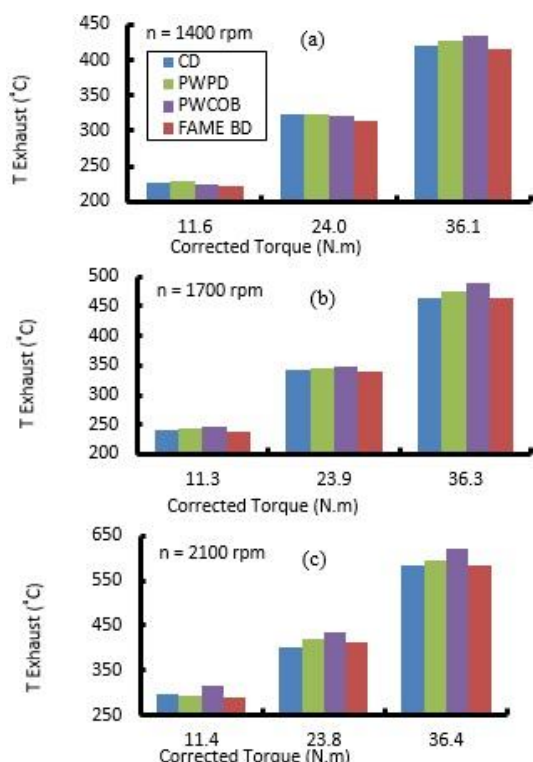


Fig.7:Exhaust gas temperature.

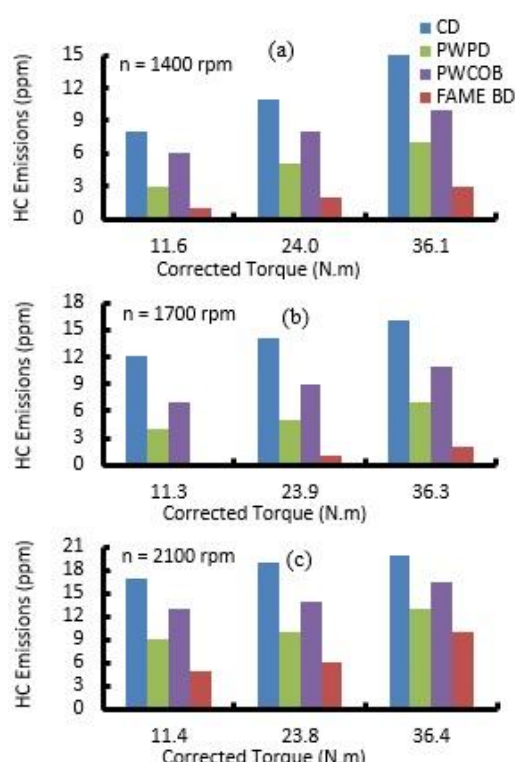


Fig.8:Hydrocarbon (HC) emissions for CD, PWCOB, PWP and FAME BD at (a) 1400 rpm, (b) 1700 rpm, and (c) 2100 rpm.

It is shown from the figure at each engine speed that the exhaust gas temperature increases with load because more fuel is burnt to meet the power requirement. In addition, it was observed that the exhaust gas temperature was reasonably higher for PWP and PWCOB whereas it was lower for FAME BD compared to the baseline CD.

Averagely, the exhaust gas temperature increase in the case of PWCOB and PWP varies approximately from 4 to 31 °C and 4 to 10 °C, respectively, whereas the exhaust gas temperature reduction in the case of FAME BD was up to 7 °C comparing with CD. By the same meaning, the exhaust gas temperature was approximately higher by 2.65% for PWCOB and 1.03% for PWP while lower by 1% with the FAME BD fuel. The higher exhaust gas temperature in the case of PWP and PWCOB compared to CD is due to higher rate of heat release during the latter of expansion where some fuel mixtures tend to burn; consequently, afterburning occurs (see the ROHR curves). In addition, the higher distillation temperature (T90) of PWCOB among the test fuels may contribute to the higher exhaust temperature (see Table 3).

The lower value of exhaust temperature may also suggest that the engine was not thermally overloaded when operating on biodiesel although more fuel was input in order to keep the same power output from engines. Another possible explanation of the lower value of exhaust temperature could be because FAME BD has got lower heating value and higher certain number than diesel fuel. Ignition delay occurred in fewer periods because of higher cetane number resulting in decrease in exhaust temperature.

3.2. Exhaust Gas Emissions Test

3.2.1. Hydrocarbons (HC)

Hydrocarbons are the consequence of incomplete combustion of the hydrocarbon fuels. It is widely accepted that the hydrocarbon emissions are mainly caused by over-mixing (i.e. mixing fuel with air to ratios that are leaner than the flammability limit) during ignition delay and by under-mixing (insufficient mixing of the fuel and air in close the nozzle orifices) during expansion.

Fig.8 presents the variations of the HC emissions for CD, PWP, PWCOB and BD at engine loads and speeds. The result demonstrates that, at overall engine operating conditions, all fuels produce very low HC emissions, and the speeds have no significant effect on the emission. It is also noticed that, as the load increases, HC emissions of all test fuels increase, gradually. The increase in the HC emissions with the increase in engine load is mainly attributed to the change in the air fuel ratio. As it well known, increasing engine load causes a reduction in the air fuel ration. Thus, it enhances the under-mixing process and consequently increases the HC emissions.

It can be seen that all test fuels yield to lower HC emissions than CD. PWCOB, PWP, and FAME BD fuels on average at all partial-load test conditions reduce the HC emissions by approximately 28.54%, 54.11%, and 79.85%, respectively, in comparison with conventional diesel. The HC reduction probably because the alternative fuels have higher cetane number, which generally reduces ignition delay period and over-mixing, hindering the formation of HC emissions. In addition, the reductions in HC emissions with PWCOB and FAME BD are also due to the fuel oxygen content, resulting in improved combustion. Furthermore, the lower density of PWCOB and the higher volatility of PWP with that of the CD improve the spray characteristics and accelerate the mixing process, hence, decreasing HC. Lastly, cleaner combustion with the utilization of PWCOB, PWP, and FAME BD fuels can be concluded from the results of HC emissions.

3.2.2. Nitrogen Oxides Emissions (NOx)

Nitrogen oxides are created during the combustion process at high-temperature from the nitrogen presence in the air and/or from the nitrogen found in fuel. The formation of NOx is dependent on temperature, local oxygen concentration, and residence time (the time period in the combustion cycle spent at high-temperature). NOx steadily increase as air ratio decreases due to the increase in fraction

of cylinder contents being burnt close to stoichiometric during combustion, and also due to higher peak temperature and pressure.

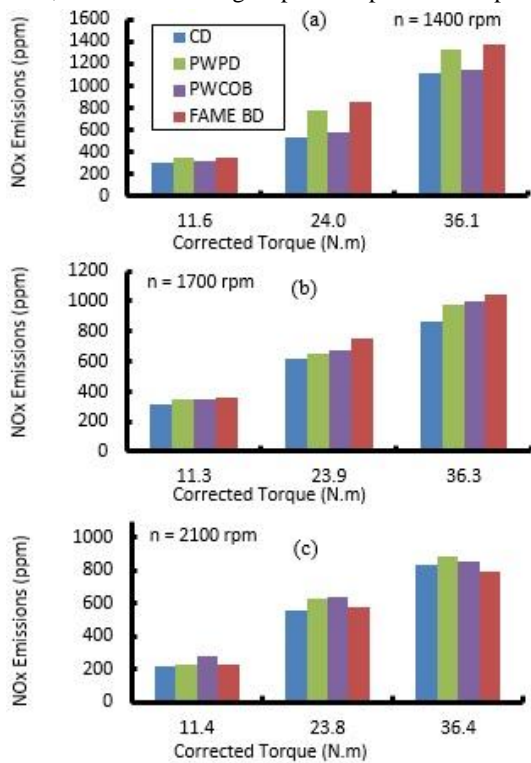


Fig.9: Nitrogen oxides (NOx) emissions for CD, PWCOB, PWPD and FAME BD at (a) 1400 rpm, (b) 1700 rpm, and (c) 2100 rpm.

The variation of NOx emissions with the PWPD, PWCOB, FAME BD, and CD under all engine conditions are shown graphically in Fig.9. As shown in the figure, NOx emissions of all test fuels increases gradually when the engine load increases. This is due to the significant increase in the exhaust temperature as it was mentioned above. It also found that all the alternative fuels emit higher NOx concentrations in compare with CD. Among the test fuels, FAME BD showed the highest NOx concentrations. The average increase in NOx emissions compared to CD fuel for PWPD, PWCOB, and FAME BD fuels was 15.26%, 10.77%, and 17.58% respectively.

The increase in NOx emissions with all the test fuels in compared with CD fuel can be explained as follows:

- One reason for the increased NOx in PWCOB and FAME BD fuels compared to CD may be the oxygen content in these biodiesels, which enhance the local oxygen concentration and consequently promote better combustion and thus the formation of NOx emission. Similarly, PWPD fuel may contain some oxygenated hydrocarbons according to [2,27]. Another factors that cause the increase in NOx could be the lighter of PWCOB cause the better spray atomization thus the higher peak temperature resulted during the combustion process of PWCOB in compared to CD.
- In the case of PWPD fuel, the higher volatility leads to better combustion efficiency and consequently higher peak temperature resulted which promotes the NOx formation.
- The higher percentage of unsaturated fatty acids composition of FAME BD, which contains double bonds in the carbon chain, may be an additional reason for higher NOx emissions.

3.2.3. Carbon Monoxide Emission (CO)

Carbon monoxide (CO) emission is toxic and must be controlled. Generally, CI engine operates with lean mixtures and

hence the CO emission would be very low. Moreover, CO emission represents lost chemical energy from the fully utilization of fuels' energy. It is believed that CO emissions result from the lack of oxygen, poor air entrainment, mixture preparation and incomplete combustion during the combustion process. Emission of CO is therefore greatly dependent on the equivalence ratio. Rich mixture results in higher CO.

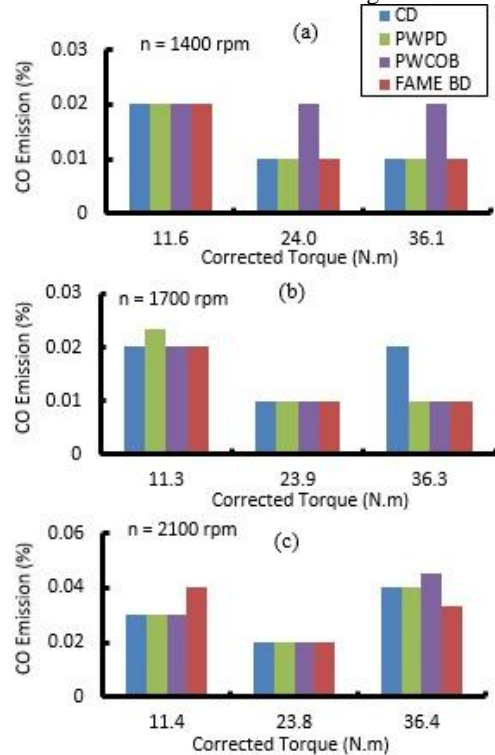


Fig. 10: Carbon monoxide (CO) emission for CD, PWCOB, PWPD and FAME BD at (a) 1400 rpm, (b) 1700 rpm, and (c) 2100 rpm.

The comparison of CO emission with CD, PWPD, PWCOB, and FAME BD fuels is shown in Fig.10. It can be seen from the results that the trends of CO emissions from the engine fueled with different fuels are similar to each other. The amount of engine has emitted CO emissions at low and medium loads are low; but are high at the full loads. The main reason for this phenomenon is due to the higher amount of injected fuel at engine full load than that at low and medium load resulting in the poorer spray atomization that causes larger amount of fuel rich zone that lack of oxygen in the spray combustion processes. In consequence, it caused more CO generated during incomplete combustion processes.

In addition, the some incomparable variations of CO emission might be due to the low accuracy of the exhaust analyzer. In general, it was noticed that the detected CO concentrations of the test fuels at partial loads are less than 0.06%, which represents the accuracy of the CO sensor of the emission analyzer.

3.2.4. Carbon Dioxide Emissions (CO2)

Carbon dioxide emission (CO2) is an indication of complete combustion; therefore, the higher CO2 represents better combustion efficiency. Fig.20 depicts the variation of CO2 emission with load for PWPD, PWCOB, FAME BD and CD at speed of 1400 rpm, 1700 rpm, and 2100 rpm. From the results, the CO2 emissions with all tested fuels increases nearly linearly as the engine load increases due to higher in-cylinder pressures and temperatures which lead to more completed and efficient

combustions. Moreover, it is observed that the amount of CO₂ produced while using PWPB, PWCOB, and FAME BD fuels is lower than CD at all loads with different engine speeds. In compare with the baseline CD, CO₂ emissions for PWCOB, PWPB, and FAME BD fuels decreased averagely by 4.88%, 5.52%, and 8.06 %, respectively. The CO₂ emissions results are good indications of more complete combustion in the case of using the alternative diesel fuels. The increase in CO₂ emissions with the PWPB, PWCOB, and FAME BD fuels were mainly due to the presence of oxygen in the chemical structure of the fuels.

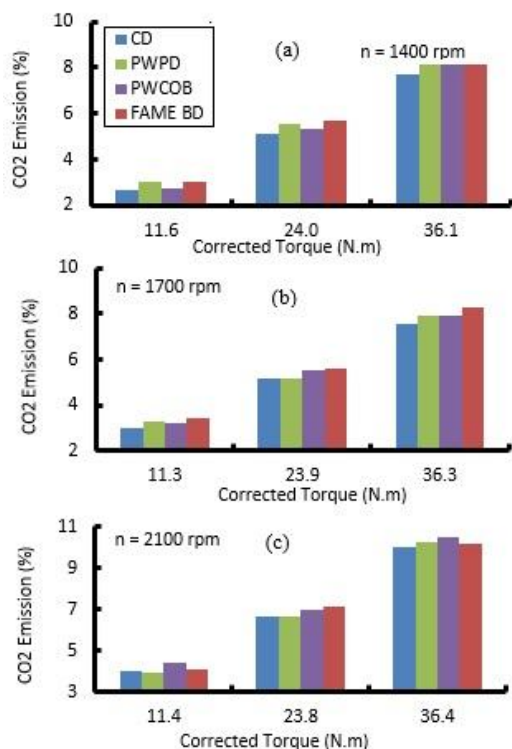


Fig.11:Carbon dioxide (CO₂) emissions for CD, PWCOB, PWPB and FAME BD at (a) 1400 rpm, (b) 1700 rpm, and (c) 2100 rpm.

3.2.5. Smoke Opacity

Smoke is nothing but solid soot particles suspended in exhaust gas. It mainly originates from pyrolysis and incomplete combustion of fuels at in homogeneous mixture conditions.

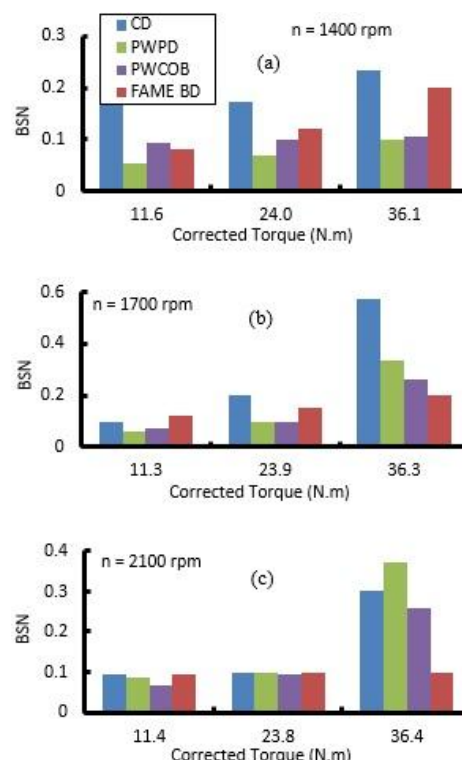


Fig. 12:Smoke opacity for CD, PWCOB, PWPB and FAME BD at (a) 1400 rpm, (b) 1700 rpm, and (c) 2100 rpm.

Fig.12 demonstrates the smoke opacity (Bosch Smoke Number, BSN) for CD, PWPB, PWCOB, and FAME BD. From figure below, smoke for baseline CD fuel is the maximum throughout the load range with significant lower values for the other comparative fuels. On average and relative to CD, 35.60% lower smoke emissions were observed with PWPB fuel and for PWCOB operation 33.25% lower smoke emissions were produced. In the case of FAME BD 25.79%, lower smoke emissions. The reductions in smoke emissions with PWCOB and FAME BD were associated with the oxygen content in the fuels. The oxygen content in the alternative fuels made the local fuel rich mixture to fuel lean mixture. The oxygen enhanced better combustion, which is resulted in reduced smoke emission. In the case of PWPB operation, the reason for the reduced smoke is the availability of premixed and homogeneous charge inside the engine well before the commencement of combustion. Higher combustion temperature, extended duration of combustion and rapid flame propagation are the other reasons for reduced smoke [12]. Another reason for lower smoke may be better and complete combustion of fuel due to the higher volatility of the PWPB fuel. From these results, it can be concluded that the use of PWCOB, PWPB and FAME BD are generally cleaner as they results in lower black smoke emission.

4. Conclusion

In the present work, the effects of two synthetic alternative diesel fuels (pyrolysis waste plastic diesel, PWPB and pyrolysis waste cooking oil biodiesel, PWCOB) on the engine performance and emissions and characteristics over a wide range of engine operating conditions were well investigated. Besides that, further comparing was done using FAME BD from palm cooking oil (palm methyl ester). Experiments were carried out on single cylinder KUBOTA RT140 diesel engine. From the research objectives, the implementation of the research and the results, conclusions can be drawn out as follows:

- The two synthetic diesel fuels showed very acceptable performance characteristics in compare with the conventional diesel fuel. These performance characteristics presented by an average improvement in the BSFC, BSEC, and BTE by 1.52%, 0.55%, and 0.75%, respectively, in the case of PWPDP, whereas slightly reductions in the mentioned performance characteristics were observed with PWCOB by 0.94%, 0.29%, and 0.37% ,respectively.
 - At all operating conditions the HC emissions are averagely lower for PWCOB, PWPDP and FAME BD by 28.78%, 54.11%, and 79.85%, respectively, compared to those of CD.
 - Under all the engine operating conditions both at low speed and high speed as well as both at partial loads and full load, the NOx emissions produced by PWCOB, PWPDP and FAME BD are slightly higher. Specifically, in average at partial load conditions NOx was higher by 10.77%, 15.26%, and 17.58%, respectively compared to CD.
 - Engine black smoke was significantly reduced with all the PWCOB, PWPDP and FAME fuels by 35.61%, 33.26%, and 25.8%, respectively, at partial load conditions.
 - At a fixed engine speed, the CO₂ emission with all tested fuels increases nearly linearly as the engine load increases while. The average increasing in the CO₂ emissions with PWCOB, PWPDP and FAME BD at partial load conditions was by 5.52%, 4.88%, and 8.06%, respectively.
 - The trends of CO emissions from the engine fueled with different fuels are similar to each other. The amount of engine has emitted CO emissions at low and medium loads are low.
 - FAME BD showed an expected results based on some previously research done.
 - The operating ability of the engine to be run with such synthetic diesel fuels under a wide range of operating conditions and without any engine's modifications indicates that the PWPDP and PWCOB are good alternative fuels for diesel and therefore must be taken into consideration in the future for transport purpose.
- [9] Celia Bee Hong Chua, Hui Mien Lee, Jonathan Sze Choong Low: Life cycle emissions and energy study of biodiesel derived from waste cooking oil and diesel in Singapore, *Int J Life Cycle Assess* 15, pp417–423, 2010.
- [10] Gerhard Knothe, Jon Van Gerpen, Jürgen Krahl: *The Biodiesel Handbook*, AOCS Press, 2005.
- [11] K.D. Maher, D.C. Bressler: Pyrolysis of triglyceride materials for the production of renewable fuels and chemicals, *ScienceDirect, Bioresource Technology* 98, pp2351–2368, 2007.
- [12] M. Mania, C. Subash, G. Nagarajan: Performance, emission and combustion characteristics of a DI diesel engine using waste plastic oil, *ScienceDirect, Applied Thermal Engineering* 29, pp2738–2744, 2009.
- [13] Agung Sudrajad, Ismail Ali, Hazmie Hamdan and Mohd. Herzwan Hamzah: Exhaust emissions of DI diesel engine using unconventional fuels, *The 4th International Meeting of Advances in Thermofluids (IMAT 2011), AIP Conf. Proc.* 1440, pp425-430, (2012).
- [14] M. Mania, G. Nagarajan, S. Sampath: Characterisation and effect of using waste plastic oil and diesel fuel blends in compression ignition engine, *ScienceDirect, Energy* 36, pp212-219, 2011.
- [15] Pawar Harshal R. and Lawankar Shailendra M.: Waste plastic pyrolysis oil alternative fuel for CI engine – A Review, *Research Journal of Engineering Sciences Vol. 2(2)*, pp26-30, 2013.
- [16] Heywood, J.B.: *Internal Combustion Engine Fundamentals*, McGraw-Hill, Inc., Singapore, 1988.
- [17] Hua Zhao, Nicos Ladommatos: *Engine Combustion Instrumentation and Diagnostics*, SAE, USA 2001.
- [18] Borman, Gary L., Ragland, Kenneth W., *Combustion Engineering*, WCB/McGraw-Hill, Singapore, 1998.
- [19] Eran Sher: *Handbook of Air Pollution from Internal Combustion Engines Pollutant Formation and Control*, Academic Press, 1998.
- [20] V Ganesan: *Internal Combustion Engines*, Tata McGraw-Hill Education Private Limited, 2010.
- [21] Klaus Mollenhauer, HelmutTschoeke.: *Handbook of Diesel engines*, Springer, 2010.
- [22] Willard W. Pulkrabek: *Engineering Fundamentals of the Internal Combustion*, Prentice Hall.
- [23] H.N. Gupta.: *Fundamentals of Internal Combustion Engines*, PHI Learning Privet Limited, 2009.
- [24] V.P.Mohana Jeya Valli, G.Gnanavel, M.Thirumarimurugan and DT.Kannadasan: A Review of alternate fuel from synthetic plastics waste, *Chemical Engineering, Elixir Chem. Eng.* 54 (2013) 12215-12218.
- [25] John Scheirs, Walter Kaminsky: *Feedstock Recycling and Pyrolysis of Waste Plastics: Converting Waste Plastics into Diesel and Other Fuels*, John Wiley & Sons Ltd, 2006.
- [26] URL: <http://www.dieselnet.com/standards/cycles/esc.php>
- [27] Sachin Kumar, R. Prakash, S. Murugan, R.K. Singh: Performance and emission analysis of blends of waste plastic oil obtained by catalytic pyrolysis of waste HDPE with diesel in a CI engine, *ScienceDirect, Energy Conversion and Management* 74, pp 323–331, 2013.

Acknowledgment

All the participations in this work are highly acknowledged.

References

- [1] Diesel Fuels Technical Review, Chevron Corporation, 2007.
- [2] M. Mania, G. Nagarajan, S. Sampath: An experimental investigation on a DI diesel engine using waste plastic oil with exhaust gas recirculation, *Science Direct, Fuel* 89, pp1826–1832, 2010.
- [3] http://www.bp.com/liveassets/bp_internet/globalbp/globalbp_uk_english/reports_and_publications/statistical_energy_review_2011/STAGING/local_assets/pdf/BP_World_Energy_Outlook_booklet_2013.pdf
- [4] H. Sharon, K. Karuppasamy, D.R. Soban Kumar, A. Sundaresan: A test on DI diesel engine fueled with methyl esters of used palm oil, *ScienceDirect, Renewable Energy* 47, pp160-166, 2012.
- [5] S. Murugan, M.C. Ramaswamy, G. Nagarajan: The use of tyre pyrolysis oil in diesel engines, *Waste Management, Volume 28, Issue 12*, pp 2743-2749, December 2008.
- [6] James G. Speight: *Synthetic Fuels Handbook: Properties, Process, and Performance*, McGraw-Hill Companies, Inc., 2008.
- [7] Mangesh G. Kulkarni and Ajay K. Dalai: Waste Cooking Oils-An Economical Source for Biodiesel: A Review, *American Chemical Society, Ind. Eng. Chem. Res.* 45, pp2901-2913, 2006.
- [8] N.N.A.N. Yusuf, S.K. Kamarudin, Z. Yaakub: Overview on the current trends in biodiesel production, *ScienceDirect, Energy Conversion and Management* 52, pp2741–2751, 2011.

Totally Volume Integral of Fluxes for Discontinuous Galerkin Method (TVI-DG) II-One Dimensional System of Equations

E. I. Elhadi and I. M. Rustum

Department of Mechanical Engineering, University of Benghazi, Libya

ABSTRACT

This is the second paper in a series in which we construct the totally volume integrals of Riemann flux mimicking Godunov flux for discontinuous Galerkin method. In this work the boundaries integrals of the Riemann fluxes are transformed into volume integral. The new family of DG method is accomplished by applying the divergence theorem to the boundaries integrals of the Riemann fluxes. Therefore, the discontinuous Galerkin (DG) method is independent on the boundaries integrals of fluxes at the cell (element) boundaries as in the classical discontinuous Galerkin (DG) methods. The modified streamline upwind Petrov-Galerkin method is used to capture the oscillation of unphysical flow for shocked flow problems. The numerical results of applying totally volume integral discontinuous Galerkin method (TVI-DG) are presented for Euler's equations in one-dimensional cases. The numerical finding of this scheme is very accurate as compared to exact solutions.

Keywords: Scalar conservation laws; Higher order methods, Discontinuous Galerkin; Divergence theorem.

1. Introduction

It is well known that nature is governed by many conservation laws. The convection plays an important role in the real word applications as weather forecasting, turbo machinery, gas dynamics and aero acoustic. The devising of robust, accurate and efficient methods is of considerable important. There has been a surge of researches activities in high order methods as spectral volume (SV) method, spectral difference (SD) method, the weighted essentially non-oscillatory (WENO) method, streamline upwind Petrov-Galerkin (SUPG) method, staggered grid (SG) method and the discontinuous Galerkin (DG) method. In this work, we concerned ourselves to the compact and weighted scheme, which is the DG method.

The DG method is introduced by Reed and Hill in 1973 for neutron transport problems and it is developed for fluid dynamics by Cockburn and Shu in series of papers among them [1-3]. The discontinuous Galerkin methods have recently become popular for the solution of systems of conservation laws. The discontinuous Galerkin methods combine two advantageous features commonly associated to finite element and finite volume methods. As in classical finite element methods, accuracy is obtained by means of high-order polynomial approximation within an element rather than by wide stencils as in case of finite volume methods. The fluxes through the element boundaries are then computed using an approximate Riemann solver, mimicking the successful Godunov finite volume method. Due to the use of Riemann fluxes across element boundaries, the DG method is conservative at the element level. Huynh [4] introduced a flux reconstruction (FR) approach, in which the formulation is capable of unifying several popular methods including the discontinuous Galerkin method, staggered-grid method, spectral difference method and spectral volume method into a single formula. The final mathematical form of the discretized governing equation is in the differential form. After that, Wang [5] extended (FR) approach to multidimensional flow and unstructured mesh under the named lifting collocation penalty (LCP) formulation. Therefore, the differences between DG and other methods lies in the definition of degrees of freedom (DOFs) and how the DOFs are updated [5]. It is well known that, the discontinuous Galerkin method is as an efficient and low error magnitude than the other methods. In the DG formulation, the boundary flux is integrated over the boundary of the cell as traditional methods like finite volume (FV) methods. While for its

development, the weighted function at the boundary of the cell can be transformed into the correction function $g(\xi)$ for (FR) or lifting coefficients $\alpha_{i,j}$ for LCP formulations. Thus $g(\xi)$ and $\alpha_{i,j}$ are dependent on the weighted functions over the boundaries [5] and [6]. Therefore, the weighted functions at the boundary play an important role for boundary flux calculation in the DG method and its development. In general, there are two types of flux integrals, the first one is the volume integral of the physical flux over the entire element domain and the second type of integral is the boundary integral of the Godunov flux over the boundaries of the elements.

This difficulty motivated ourselves to introduce a new family of DG method independent on the weighting functions at the boundaries. Therefore, no boundary integral is needed for this new formulation. The paper is organized as follows. Section 2 introduced the new DG method formulations. The verification of the new formulation is introduced in section 3. Finally, conclusion remarked is introduced into section 4.

2. Totally Volume Integral (TVI) DG Method Formulation

2.1. Space discretization

For convenience of discussion, a review for DG semi-discretization for partial differential equations (PDE) is introduced. This can be done by firstly considering the conservative laws in divergence form:

$$Q_t + \nabla \cdot F(Q) = 0 \dots\dots\dots (2.1)$$

The numerical solution of Eqn. (2.1) is sought on the computational domain Ω subject to proper initial and boundary conditions. Where Q is the conservative variable and F is the conservative flux vector. In Eqn. (2.1), Q and F are scalar or column, representing scalar or system of equations. For example, Eqn. (2.1) represents system of equations, which are one-dimensional Euler equations, if:

$$Q = \begin{bmatrix} \rho \\ \rho u \\ \rho E \end{bmatrix}, F(Q) = \begin{bmatrix} \rho u \\ \rho u^2 + p \\ u(\rho E + p) \end{bmatrix} \dots\dots\dots (2.2)$$

with $p = (\gamma - 1) \left(\rho E - \frac{1}{2} \rho u^2 \right)$

The weighted residual formulation is obtained by multiplying Eqn. (2.1) by a scalar test function (weighted function) W and integrating by parts over the domain Ω

$$\int_{\Omega} [W Q_t - \nabla W \cdot F(Q)] d\Omega + \int_{\partial\Omega} W F(Q) \cdot n d\Gamma = 0 \dots\dots (2.3)$$

A discretization analogue of Eqn. (2.3) over each element can be obtained by subdivided the computational domain Ω into N non-overlapping elements $\Omega = \bigcup_{j=1}^N \Omega_h$. By applying Eqn. (2.3) to each element Ω_h , the semi-discrete analogue of Eqn. (2.3) over the computational grid yields:

$$\int_{\Omega_h} \left[W_h \frac{\partial Q_h}{\partial t} - \nabla W_h \cdot F(Q_h) \right] d\Omega_h + \int_{\partial\Gamma_h} W_h F(Q_h) \cdot \mathbf{n} d\Gamma_h = 0 \dots (2.4)$$

Γ_h denotes the boundary of the element Ω_h and \mathbf{n} is outward vector normal to the boundary. Let Q_h and W_h represents the finite element approximation to the analytical solution Q and the test function W , respectively. Where Q_h and W_h are approximated by a piecewise polynomial function of degrees k , which is continuous within each element and discontinuous between the elements interfaces

$$Q_h(x, t) = \sum_{j=1}^{j=n} \varphi_j Q_j(t) \text{ and } W_h(x) = \sum_{j=1}^{j=n} \varphi_j W_j \dots (2.5)$$

where n is the dimension of the polynomial space P^K and φ_j is the basis of the polynomial. The expansion coefficients $Q_i(t)$ and W_j denotes the degrees of freedom (DOFs) of the numerical solution and of the test function in element Ω_h , respectively. Thus, the summation in eqn. (2.4) is equivalent to the following system of n equations:

$$\int_{\Omega_h} \varphi_j Q_t - \nabla \varphi_j F(Q_h) d\Omega_h + \int_{\Gamma_h} \varphi_j F(Q_h) \cdot \mathbf{n} d\Gamma_h = 0 (2.6)$$

Where, $(1 \leq j \leq n)$

Since in the DG method, the discontinuities are permitted at the interfaces of elements. Because the approximated solution is discontinuous at the element boundaries, the interface flux is not uniquely defined. In this stage, the Riemann fluxes used in the Godunov finite volume method are borrowed.

The normal flux function $F(Q_h) \cdot \mathbf{n}$ appearing in the last terms of eqn.(2.6) is replaced by a numerical Riemann flux function $F_{up} = F(Q_L, Q_R, \mathbf{n})$ that depends on Q_L and Q_R which are the approximated solutions of the conservative state variables Q_h at the left and right side of the element boundary, respectively. In order to guarantee consistency and conservation, the Riemann flux must satisfy:

$$F(Q_L, Q_R, \mathbf{n}) = F_{up} = F(Q_h) \cdot \mathbf{n}, \text{ and } F(Q_L, Q_R, -\mathbf{n}) = -F_{up} = -F(Q_h) \cdot \mathbf{n} (2.7)$$

In the present work, the Riemann flux is approximated by using Lax and Friedrich (LF) flux. This scheme is called discontinuous Galerkin method of degree k as given in the classical form, or in short notation DG (k) method. The surface and volume integrals in Eqn. (2.6) are calculated in case of DG method by using $2k$ and $2k+1$ order accurate Gauss quadrature formulas, respectively. In order to unify the integrals (surface integral and volume integral), the totally volume integral of the upwind flux scheme for DG method is used for this purpose. This can be done by using the relation between surface and volume integrals for any vector A , which is given by the divergence theorem as:

$$\oint_{\partial\Omega} A \cdot d\Gamma = \oint_{\partial\Omega} A \cdot \mathbf{n} d\Gamma = \iiint_{\Omega} \nabla \cdot A dV \dots (2.8)$$

where Γ and V are surface and volume of the problem domain. The totally volume integral DG method is accomplished by applying the divergence theorem to the last term of Eqn. (2.6) and rearrangement to give the following form

$$\int_{\Omega_h} \left[\varphi_j \frac{\partial Q_h}{\partial t} - \frac{\partial \varphi_j}{\partial x} F(Q_h) + \frac{\partial \varphi_j}{\partial x} F_{up} + \varphi_j \frac{\partial F_{up}}{\partial x} \right] d\Omega_h = 0 \dots (2.9)$$

The Riemann or upwind flux vectors are approximated by polynomial of order k as done for the state variable in Eqn. (2.5). $F(Q_h) = \sum_{i=1}^{i=n} \varphi_i F_i(Q_h)$, $F_{up} = \sum_{i=1}^{i=n} \varphi_i F_{up,i}$ the last two

terms of Eqns. (2.9) can be companied into one term as follows:

$$\int_{\Omega_h} \left[\varphi_j \frac{\partial Q_h}{\partial t} - \frac{\partial \varphi_j}{\partial x} \varphi_i F_i(Q_h) + \left(\frac{\partial \varphi_j}{\partial x} \varphi_i + \varphi_j \frac{\partial \varphi_i}{\partial x} \right) F_{up,i} \right] d\Omega_h = 0 \dots (2.10)$$

Equation (2.10) is the DG method in totally volume integral form.

2.2. Coordinate Transformation

In order to achieve an efficient implementation, all the elements are transformed from the computational space (x, y, z) into standard space (ζ, η, ξ) . Consequently, all the partial derivatives with respect to the standard space are related to the partial derivative in the computational space as in the finite element methods. For one-dimensional case, the value of the x can be obtained as:

$$x = \sum_{i=1}^{i=n} x_i \varphi_j(\zeta) \dots (2.11)$$

The derivative of x with respect ζ is obtained as:

$$\frac{\partial x}{\partial \zeta} = x_\zeta = \sum_{i=1}^{i=n} x_j \frac{\partial \varphi_j(\zeta)}{\partial \zeta} \dots (2.12)$$

The derivatives of any function with respect to the standard coordinate can be written as:

$$\frac{\partial(\)}{\partial \zeta} = \frac{\partial(\)}{\partial x} \frac{\partial x}{\partial \zeta} = \frac{\partial(\)}{\partial x} x_\zeta \text{ with } |J| = |x_\zeta| \dots (2.13)$$

Where $|J|$ is the determinant of Jacobian matrix. In addition, the derivatives of any function with respect to physical coordinates can be written as:

$$\frac{\partial(\)}{\partial x} = \frac{\partial(\)}{\partial \zeta} \frac{\partial \zeta}{\partial x} = \frac{\partial(\)}{\partial \zeta} \zeta_x, \text{ with } |J^{-1}| = |\zeta_x| \dots (2.14)$$

From equations (2.12) and (2.14) $x_\zeta = 1/\zeta_x$, with $n_\zeta = \zeta_x/|\zeta_x| = 1$. Thus the Riemann flux $F_{up} = F(Q_L, Q_R, \mathbf{n})$ has no negative direction at the boundaries. By substituting into Eqn. (2.9) and rearrangement yields:

$$\int_{\Omega_h} \left[\varphi_j \frac{\partial Q_h}{\partial t} - \frac{\partial \varphi_j}{\partial \zeta} \varphi_i + \left(\frac{\partial \varphi_j}{\partial \zeta} \varphi_i + \varphi_j \frac{\partial \varphi_i}{\partial \zeta} \right) (\zeta_x F_{up,i}) \right] d\Omega_h = 0 \dots (2.15)$$

Finally, after the spatial discretization is accomplished, equation (2.14) can be written into the following form:

$$M \frac{dQ}{dt} = R(Q), \dots (2.16)$$

where $R(Q)$ and M are called the residual and consistent mass matrix, respectively.

2.3. Time integral

The semi-discrete equation as eqn. (2.15) can be integrated in time using explicit methods. The explicit three-stage third-order TVD Runge-Kutta scheme RK(3,3) and five-stage fourth order RK(5,4) are the widely used methods given in many references among them Ref. [10] and [11]. The RK(3,3) can be expressed in the following form:

$$Q^{(1)} = Q^n + \Delta t M^{-1} R(Q^n) \dots (2.17.a)$$

$$Q^{(2)} = \frac{3}{4} Q^{(n)} + \frac{1}{4} [Q^{(1)} + \Delta t M^{-1} R(Q^{(1)})] \dots (2.17.b)$$

$$Q^{n+1} = \frac{1}{3} Q^n + \frac{2}{3} [Q^{(2)} + \Delta t M^{-1} R(Q^{(2)})] \dots (2.17.c)$$

This method is linearly stable for a Courant number less than or equal to 1.

3. Numerical Results

As a preliminary test, we apply the totally volume integral discontinuous Galerkin method to Euler equations in one-dimensional cases.

3.1. Numerical tests and comparison.

We apply the TVI-DG method to one-dimensional Euler equations eqn. (2.2) in Cartesian coordinate and in cylindrical coordinate (explosion cylinder).

Example-1

The first example is the Riemann problem of Lax considering in many references among them [9]. Zero gradient boundary conditions are applied at the boundaries. The problem domain $x = [-0.5, 0.5]$ is divided into 100 equally space elements, with the initial conditions given as

$$(\rho, u, P) = \begin{cases} (0.445, 0.698, 3.528) & \text{if } x \leq 0 \\ (0.5, 0.0, 0.571) & \text{if } x > 0 \end{cases}$$

The approximated solutions are constructed from polynomials of orders k from 1 to 4. The lax-Friedrich flux scheme is used to evaluate the boundary fluxes. The RK (3, 3) is used for $k = 1$ and 2 while RK (5, 4) is used in case of $k = 3$ and 4, where the RK methods are used for evaluating the time integral part. The numerical results are obtained at time $t = 0.13$. Figures 1 to 3 display the numerical results of the approximated density, velocity and pressure solutions by using of TVI-DG method with polynomials from 1 to 4. The modified streamline upwind Petrov-Galerkin is used to capture the nonphysical oscillation solutions due to the discontinuity of the flow. Figures 1 to 3 demonstrated that TVI-DG method is very efficient scheme in evaluating discontinuous flow problems. The problem solution consists from left rarefaction, contact and right shock waves. There is no enclosed solution of this problem. Therefore the exact solution can be obtained by using 1500 elements with approximated solution is constructed from polynomial of order $k = 2$.

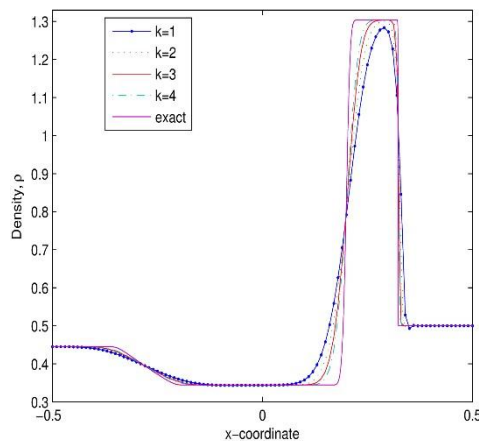


Fig. 1: Density distribution of example 1 by using TVI-DG, at time $t=0.13$ with polynomials of order $k=1$ to 4.

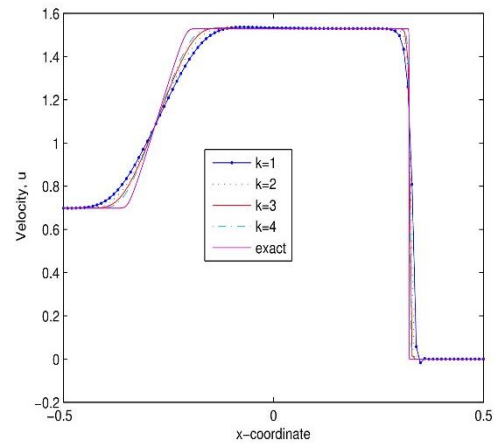


Fig. 2: Velocity distribution of example 1 by using TVI-DG, at time $t=0.13$ with polynomials of order $k=1$ to 4.

Example-2

The second example is considering in [7], with the initial conditions given as:

$$(\rho, u, P) = \begin{cases} (1.0, -2.0, 0.4) & \text{if } 0 \leq x \leq 0.5 \\ (1.0, 2.0, 0.4) & \text{if } 0.5 < x \leq 1 \end{cases}$$

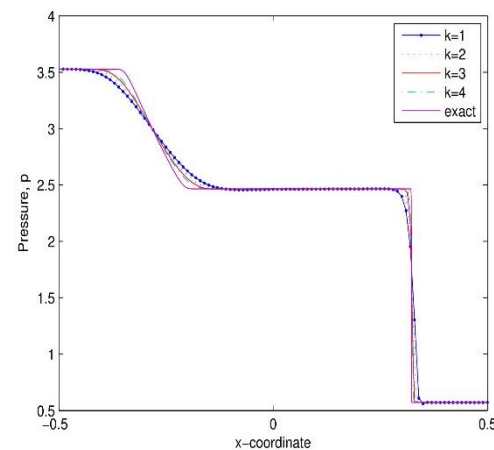


Fig. 3: Pressure distribution of example 1 by using TVI-DG, at time $t=0.13$ with polynomials of order $k=1$ to 4.

The reflecting boundary conditions are applied at the boundaries. The problem domain $x = [0, 1]$ is divided into 200 equally space elements. The approximated solutions are constructed from polynomials of orders k from 2 to 4. The lax-Friedrich flux scheme is used to evaluate the boundary fluxes. The RK (3, 3) is used for $k = 2$ while RK (5, 4) is used in case of $k = 3$ and 4. The numerical results are obtained at time $t = 0.15$. Figures 4 to 6 display the numerical results of density, velocity and pressure solutions by using TVI-DG method with polynomials from 2 to 4. The modified streamline upwind Petrov-Galerkin is used to capture the nonphysical oscillation solutions due to the discontinuity of the flow. Figures 4 to 6 reveal that TVI-DG method is very efficient scheme in evaluating discontinuous flow problems.

The solution is consisted from left rarefaction, contact and right rarefaction waves. The solutions demonstrated that the pressure is very small closed to vacuum pressure with low-density profile. There is no enclosed solution of this problem. Therefore, the exact solution can be obtained by using 800 element with approximated solution is constructed from polynomial of order $k = 5$.

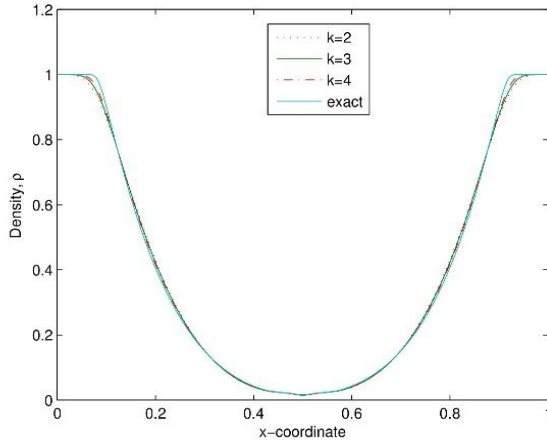


Fig. 4: Density distribution of example 2 by using TVI-DG, at time $t=.15$ with polynomials of order $k=2$ to 4.

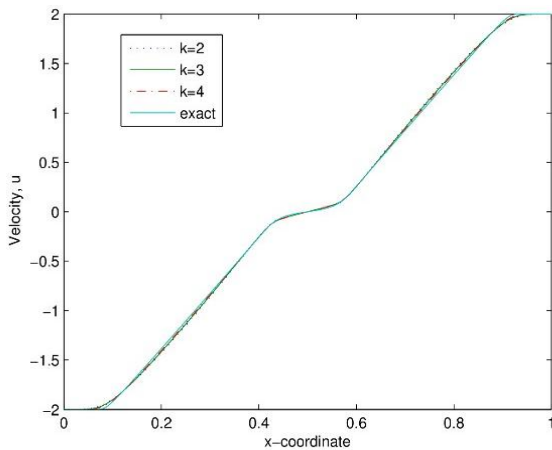


Fig. 5: Velocity distribution of example 2 by using TVI-DG, at time $t=.15$ with polynomials of order $k=2$ to 4.

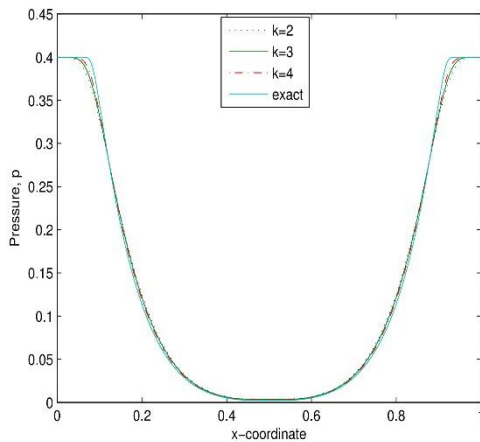


Fig. 6: Pressure distribution of example 2 by using TVI-DG, at time $t=.15$ with polynomials of order $k=2$ to 4

Example-3

The third example is a shock sod tube in cylindrical coordinate given in [8]. The two dimensional cylindrical Euler equations can be reduced into one-dimensional Euler equations with source term as follows:

$$\frac{\partial Q}{\partial t} + \frac{\partial F(Q)}{\partial r} = S(Q),$$

where

$$Q = \begin{bmatrix} \rho \\ \rho u \\ \rho E \end{bmatrix}, F = \begin{bmatrix} \rho u \\ \rho u^2 + p \\ \rho u H \end{bmatrix} \text{ and } S(Q) = \frac{-\alpha}{r} \begin{bmatrix} \rho u \\ \rho u^2 \\ u(\rho E + p) \end{bmatrix}$$

with r is the radial distance from origin and $\alpha = 1$ for cylindrical symmetric flows, with the initial conditions are given as:

$$(\rho, u, P) = \begin{pmatrix} 1.0 & 0.0 & 1.0 & \text{if } 0 \leq x \leq 0.4 \\ 0.125 & 0.0 & 0.1 & \text{if } 0.4 < x \leq 1 \end{pmatrix}$$

The reflecting boundary conditions are applied at the boundaries. The problem domain $x = [0, 1]$ is divided into 200 equally space elements. The approximated solutions are constructed from polynomials of orders k from 1 to 4. The lax-Friedrich flux scheme is used to evaluate the boundary fluxes. The RK (3, 3) is used for $k = 1$ and 2 while RK (5, 4) is used in case of $k = 3$ and 4. The numerical results are obtained at time $t = 0.2$. Figures 7 to 9 display the numerical results of the approximated density, velocity and pressure solutions by using TVI-DG method with polynomials of orders from 1 to 4. The modified streamline upwind Petrov-Galerkin is used to capture the nonphysical oscillation solutions due to the discontinuity of the flow. Figures 7 to 9 demonstrated that TVI-DG method is very efficient scheme in evaluating discontinuous flow problems. The solution consists of a circular shock wave propagating from the origin, followed by a circular contact discontinuity traveling in the same direction, and a circular expansion wave moving towards the origin. The solutions are used as validating for the full model of two-dimensional problem.

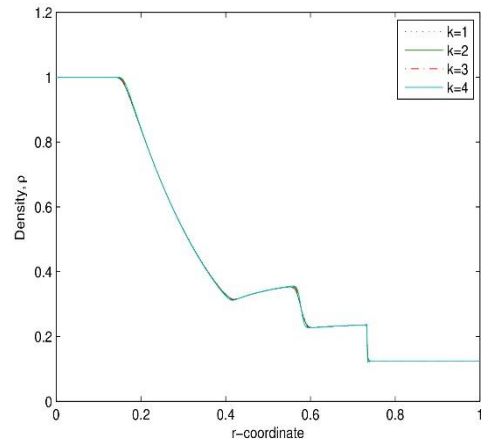


Fig.7: Density distribution of example 3 by using TVI-DG, at time $t= 0.2$ with polynomials of order $k=1$ to 4.

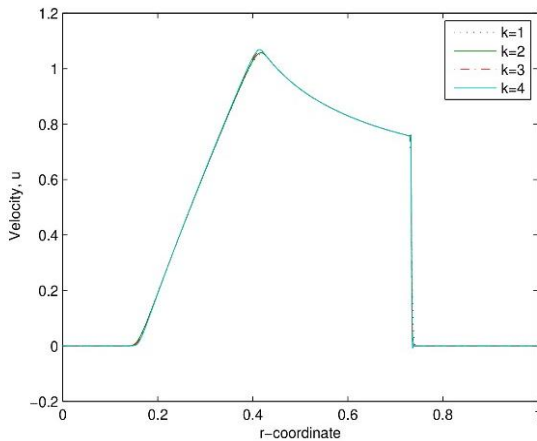


Fig. 8: Velocity distribution of example 3 by using TVI-DG, at time $t=0.2$ with polynomials of order $k=1$ to 4

4. Discussion and conclusions

The transformation of the boundaries integrals into the volume integrals is introduced in this work under the named TVI-DG method. Thus, there is no integration of the test function at the boundaries as in the classical DG method. The totally volume integral discontinuous Galerkin method is used to solve system of equations (Euler equations). The numerical finding presented that the TVI-DG scheme is very efficient for solving problems with shock waves.

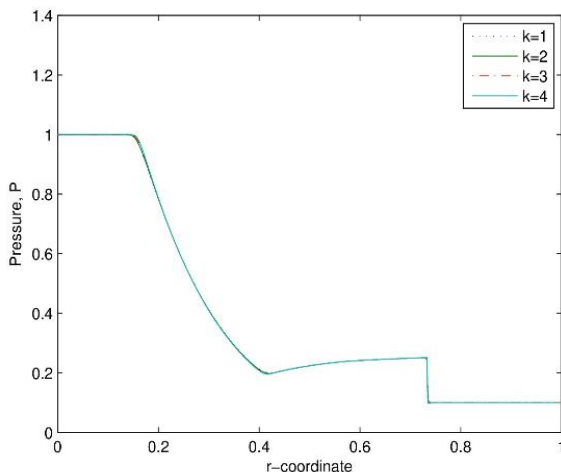


Fig. 9: Pressure distribution of example 3 by using TVI-DG, at time $t=0.2$ with polynomials of order $k=1$ to 4.

References

- [1] Cockburn, B. & Shu, C. W. TVB Runge-Kutta local projection discontinuous Galerkin finite element method for conservation laws II: General framework. *Mathematics of Computation* Vol. 52, 441-435 (1989).
- [2] Cockburn, B., Lin, C. Y. & Shu, C. W. TVB Runge-Kutta local projection discontinuous Galerkin finite element method for conservation laws III: One-dimensional systems. *Journal of Computational Physics* Vol. 84, 90-113 (1989).
- [3] Cockburn, B. & Shu, C. W. The Runge kutta local projection p^1 -discontinuous Galerkin finite element method for scalar conservative laws. *Mathematical Modeling and Numerical Analysis* 25, 337-361 (1991).
- [4] Huynh, H. T. A flux reconstruction approach to high-order schemes including discontinuous Galerkin methods. 18th AIAA computational fluid dynamics conference, 25-28 June Miami FL 4079 (2007).
- [5] Wang, Z. J. & Gao, H. A unified lifting collocation penalty formulation including the discontinuous Galerkin, spectral volume/difference methods for conservation laws on mixed grids. *Journal of Computational Physics* Vol. 228, 8161-8186 (2009).
- [6] Haiyang Gao & Wang, Z. J. A High-order Lifting Collocation Penalty Formulation for the Navier-Stokes Equations on 2D Mixed Grids. 19th AIAA Computational Fluid Dynamics 22 - 25 June 2009, San Antonio, Texas.
- [7] E. F. Toro. *Riemann Solvers and Numerical Methods for Fluid Dynamics*. Springer Verlag, 1997
- [8] Jianguo Xin & Joseph E. Flaherty. Viscous stabilization of discontinuous Galerkin solutions of hyperbolic conservation laws. *Applied Numerical Mathematics* 56 444-458 (2006).
- [9] Andrew K. Henrick, Tariq D. Aslam & Joseph M. Powers. Mapped weighted essentially non-oscillatory schemes: Achieving optimal order near critical points. *Journal of Computational Physics* 207 542-567 (2005).
- [10] Chengming Huang. Strong stability preserving hybrid methods. *Applied Numerical Mathematics* 59 891-904 (2009).
- [11] Gottlieb, S., Ruuth, S.J.: Optimal strong-stability-preserving time-stepping schemes with fast downwind spatial discretizations. *J. Sci. Comput.* 27, 289-303 (2006)